Investigation of material and device properties of GaAsSbN for multi-junction solar cell applications

Tomos Daniel Thomas

Imperial College London, Department of Physics

A thesis submitted for the degree of Doctor of Philosophy (PhD)

June 6, 2017

Declaration of Originality

I hereby declare that the work presented in this thesis is my own, except where described in the text. The work of others has been acknowleged and a list of references is provided.

Copyright Declaration

The copyright of this thesis rests with the author and is made available under a Creative Commons Attribution Non-Commercial No Derivatives license. Researchers are free to copy, distribute or transmit the thesis on the condition that they attribute it, that they do not use it for commercial purposes and that they do not alter, transform or build upon it. For any reuse or redistribution, researchers must make clear to others the license terms of this work.

Abstract

Multi-junction solar cells (MJSCs) have achieved the highest solar power conversion efficiency to date of any type of solar cell and still have considerable potential for improvement compared to their theoretical efficiency. The bandgap combination of sub-cells is an extremely important factor in cell efficiency, with new materials with particular bandgaps necessary to increase efficiency further. Possible improved multi-junction solar cell designs require sub-cells with bandgaps between 1.2 and 0.8 eV. The dilute nitride alloy GaAsSbN can provide adjustable bandgaps in this region while remaining lattice-matched to common Ge and GaAs substrates. This thesis presents measurements and analysis of GaAsSbN 1 eV material and devices. Firstly, simulations of overall MJSC designs for concentrator photovoltaic applications are presented, including the importance of bandgap tunability in the 1 eV region. The material and device properties of 1 eV GaAsSbN subcells are studied experimentally and their performance compared to that necessary for inclusion in MJSCs. Electroreflectance spectroscopy and a model dielectric function are used to examine the absorption properties of GaAsSbN. Time-resolved photoluminescence spectroscopy is used to examine carrier recombination times and mechanisms, finding a typical recombination lifetime of 400 ps. Solar cell devices are electrically and optically characterised using current-voltage, capacitance-voltage and quantum efficiency measurements. The devices are modeled in order to investigate transport, finding a 30 nm hole diffusion length and 500 nm electron diffusion length. Improved sub-cell designs are proposed. Practical limits to the performance of GaAsSbN sub-cells are discussed.

Acknowledgments

There are many people that deserve sincere thanks for helping me get to this point.

I wouldn't even have made it to university were it not for my mum, who, after I dropped out of A levels the first time round, persuaded me to give it another try. I couldn't have stayed at university if not for my dad, who has spent half his life driving along the M4. My parents and grandparents have done so much to get me here.

During my PhD, Ned Ekins-Daukes and Andy Johnson have been ideal supervisors. The CASE funding provided by IQE very much enhanced my studies. Ned and Andy have also always been fun to work with and I have fond memories of the conferences I've attended and the people I met there.

I am grateful to Professor Yoon, Kian-Hua, Loke and Satrio at NTU for providing the samples in this work and for hosting my visit to NTU. At the University of Kobe, my thanks go to Professor Kita and Kasamatsu-san as well as the rest of the group for hosting me and supporting my streak camera measurements.

The members of the QPV group have all helped me along the way. Louise, Megumi and Alvin introduced me to the world of high efficiency PV in the early days. Diego and Markus have both written excellent software that provided the foundation for the calculations here. Nic and Tom Wilson were always great company as well as contributing valuable ideas. Jose was an excellent conference roommate and Alex M an excellent motel roommate.

Finally, I can't say thank you enough to the family of Claire Rodin, and Claire herself.

Contents

Abstract 8

1 Introduction **17**

1.1 Basics of solar cells 17

1.1.1 Fundamental limits 18

1.1.2 The solar spectrum and concentration 19

1.2 Applications of III-V solar cells 20

1.3 Multi-junction solar cells 24

1.3.1 Structure of multi-junction solar cells 24

1.4 Lattice-matched multi-junction solar cells 27

1.5 Outline of this thesis 30

2 Theory and previous work **31**

2.1 Absorption and emission in semiconductors 31

2.1.1 Band structure 33

2.1.2 Model dielectric functions 35

2.2 Electron and hole recombination in semiconductors 38

2.2.1 Radiative recombination 39

2.2.2 Non-radiative recombination 40

2.2.3 Auger recombination 41

2.3 Semiconductor transport 41

2.3.1 The *pn* junction . . . 44
2.3.2 Quantum efficiency . . . 47
2.3.3 Current-voltage characteristic . . . 49
2.3.4 Current-voltage characteristic analysis . . . 51
2.4 Multi-junction solar cell efficiency . . . 52
2.4.1 Optimal bandgaps . . . 53
2.4.2 Extrinsic loss mechanisms . . . 53
2.4.3 Radiative coupling . . . 54
2.5 Dilute nitride alloys . . . 57
2.5.1 Band anti-crossing . . . 58
2.5.2 Localised and excitonic recombination . . . 59

3 Experimental methods 63
3.1 Molecular beam epitaxy . . . 63
3.2 Transmission and reflection spectroscopy . . . 64
3.3 Electroreflectance . . . 67
3.4 Photoluminescence . . . 69
3.4.1 Continuous wave . . . 70
3.4.2 Time-resolved . . . 70
3.5 Device electrical characterisation . . . 71
3.5.1 Current-voltage characteristic . . . 71
3.5.2 Capacitance-voltage characteristic . . . 72
3.5.3 Quantum efficiency . . . 74

4 Multi-junction solar cell radiative coupling and series resistance 76
4.1 Simulation method for MJSC IV including radiative coupling . . . 77
4.1.1 Short-circuit current . . . 77
4.1.2 Extrinsic losses . . . 78

4.2 Limits to triple-junction cell from series resistance and shading 80
4.3 Effect of radiative coupling on spectral sensitivity of multi-junctions 81
4.3.1 Radiative recombination model 81
4.3.2 Results 86
4.4 Effect of radiative coupling on optimal bandgap 97
4.5 Conclusions 100

5 Absorption properties of GaAsSbN alloys 101
5.1 Direct measurement of absorption coefficient 102
5.2 Model dielectric function approach 102
5.2.1 Electroreflectance measurement and fitting 106
5.2.2 Contributions to dielectric function 108
5.3 Results and discussion 109
5.4 Conclusions 116

6 Carrier dynamics of GaAsSbN 117
6.1 Sample design 118
6.2 Photoluminescence method 119
6.3 Results and discussion 120
6.3.1 Interface and bulk recombination 120
6.3.2 Variation with dopant properties 121
6.3.3 Carrier localisation effects 126
6.4 Conclusions 129

7 GaAsSbN 1 eV sub-cell characterisation 130
7.1 Basic sample designs 130
7.2 Proposed designs for improved short-circuit current 131
7.3 Experimental 134
7.4 Results and discussion 135

7.4.1 Basic cell designs 135
7.4.2 Effect of dopant polarity on quantum efficiency 143
7.4.3 Modeling 144
7.4.4 Improved designs 147
7.4.5 Model 147
7.4.6 Experiment 149
7.4.7 Limits to GaAsSbN sub-cell performance 153
7.5 Conclusions 157

8 Summary and further work **158**

A Sample layer structures **172**

B Streak camera images **179**

C List of publications **187**

List of Figures

1.1 IV curve of a triple-junction solar cell 18
1.2 The solar spectrum 20
1.3 Solar cell efficiency chart 22
1.4 Schematic of a triple-junction solar cell 25
1.5 Lattice constant and bandgap for several binary compounds and ternary III-V alloys, as well as germanium and GaAsSbN 28

2.1 Model dielectric function of gallium arsenide 38
2.2 Optical constants of GaAs derived from model dielectric function 39
2.3 Illustration of carrier recombination mechanisms in III-V semiconductor materials 42
2.4 Illustration of effect of illumination on minority carrier transport in a *pn* junction 45
2.5 Illustration of *pn* junction properties for a 1 μm thick *np* GaAs junction . . 46
2.6 Equivalent circuit model of single junction solar cell 51
2.7 Schematic of photon recycling and radiative coupling in solar cells 55
2.8 Simulated MJSC IV curves with and without radiative coupling 56
2.9 Illustration of band anti-crossing in GaAsN 60
2.10 Schematic of disordered conduction band and potential fluctuation 61

3.1 Schematic of MBE equipment and process 65

3.2 Experimental set-up for transmittance and reflectance measurements . . . 66
3.3 Illustration of multiple reflections within layered semiconductor structure . 67
3.4 Experimental set-up for electroreflectance measurements 69
3.5 Experimental set-up for time-resolved photoluminescence measurements . . 71
3.6 Calibration of solar simulator through IV curve comparison 73
3.7 Experimental set-up for quantum efficiency measurements 75

4.1 Calculation of several triple-junction solar cell efficiencies showing the importance of designing front grid adequately for series resistance and the limit to efficiency imposed by series resistance 81
4.2 Calculation of 1.90/1.42/1.03 eV triple-junction solar cell efficiency at 1000 suns as a function of both series resistance and shading 82
4.3 Calculation of 1.90/1.42/1.03/0.66 eV quad-junction solar cell efficiency at 1000 suns as a function of both series resistance and shading 83
4.4 Schematic showing the three contributions of Eq. (4.6) to the absorptivity of a solar cell 84
4.5 Radiative recombination current and escaped fraction from the top of the cell as a function of sub-cell thickness 87
4.6 Power enhancement from radiative coupling as a function of air mass . . . 90
4.7 Power enhancement from radiative coupling as a function of precipitable water 91
4.8 Power enhancement from radiative coupling, as a function of AOD and Angström Exponent for an optimized 1.74/1.18/0.69 eV bandgap triple-junction 92
4.9 Power enhancement from radiative coupling, as a function of AOD and Angström Exponent for an optimised 1.92/1.42/1.04/0.69 eV bandgap quad-junction 93

4.10 Energy yield enhancement from radiative coupling over annual periods for locations and cell designs identified 96
4.11 Schematic of 1.15 eV quad-junction architectures and breakdown of extrinsic losses 98
4.12 Calculation of the externally-induced sub-cell short-circuit current needed in the 1.15 eV sub-cell 99

5.1 Comparison of literature data for dilute nitride material absorption coefficients with absorption coefficient of GaAsSbN measured for this thesis using reflection and transmission 103
5.2 Calculated complex refractive index of GaAsN based on the model dielectric function and parameters from literature 105
5.3 Electroreflectance spectrum of 1eV GaAsSbN np junction 107
5.4 Comparison of experimentally determined absorption coefficient with that calculated by model dielectric function based on the measurement of electroreflectance of GaAsSbN 111
5.5 Photoluminescence of samples N2436 and N2627 113
5.6 Bandgap energy of GaAsSbN as function of N and Sb composition 114
5.7 Short-circuit current density (J_{SC}) calculated from the model absorption coefficient as a function of Sb and N composition 115

6.1 Schematic of double heterostructures for TRPL study 119
6.2 Effective lifetime variation with layer thickness 121
6.3 Decay profile for emission at the peak emission wavelength of samples with different barrier material but otherwise identical structure 122
6.4 Variation of effective lifetime with doping at room temperature 124
6.5 Emission profile at the peak emission wavelength for opposite polarity doped samples at 3K 125

6.6 Shift in photoluminescence peak energy position with temperature 127
6.7 Dispersion of recombination lifetime with emission photon energy 128

7.1 Schematic of the homojunction device design N2627 investigated in this study 132
7.2 Schematic of the heterojunction device design N2623 investigated in this study 133
7.3 Current-voltage measurements in the dark for the two device designs . . . 136
7.4 Current-voltage characteristic of the two devices under AM1.5G illumination 137
7.5 EQE of the two basic device designs reported, including effect of bias on EQE 139
7.6 Capacitance-voltage data of the two devices 141
7.7 Carrier density as a function of junction depletion width as determined from the C-V measurement 142
7.8 External quantum efficiency measurements for 3 solar cells of varying doping 144
7.9 Comparison between measured IQE of N2627 and a one-dimensional model taking into account minority carrier diffusion and interface recombination . 147
7.10 Comparison of band profile and simulated EQE of different emitter design devices 148
7.11 DIV of different emitter designs 151
7.12 EQE of the improved emitter device designs 152
7.13 Overall MJSC short-circuit current as a function of the minority carrier diffusion length and background doping of the *nip* GaAsSbN sub-cell . . . 155
7.14 Overall MJSC efficiency as a function of the minority carrier diffusion length and background doping of the *nip* GaAsSbN sub-cell 156

B.1 Streak camera image of sample N2670 at room temperature (300 K), 900 nm incident excitation, 100μW incident power. 179

B.2 Streak camera image of sample N2671 at room temperature (300 K), 900 nm incident excitation, 100μW incident power. 180
B.3 Streak camera image of sample N2671 at room temperature (300 K), 900 nm incident excitation, 100μW incident power. 180
B.4 Streak camera image of sample N2671 at 3 K, 900 nm incident excitation, 100μW incident power. 181
B.5 Streak camera image of sample N2672 at room temperature (300 K), 900 nm incident excitation, 100μW incident power. 181
B.6 Streak camera image of sample N2672 at room temperature (300 K), 900 nm incident excitation, 900μW incident power. 182
B.7 Streak camera image of sample N2673 at room temperature (300 K), 900 nm incident excitation, 900μW incident power. 182
B.8 Streak camera image of sample N2673 at 3 K, 900 nm incident excitation, 100μW incident power. 183
B.9 Streak camera image of sample N2674 at room temperature (300 K), 900 nm incident excitation, 900μW incident power. 183
B.10 Streak camera image of sample N2675 at room temperature (300 K), 900 nm incident excitation, 100μW incident power. 184
B.11 Streak camera image of sample N2675 at room temperature (300 K), 900 nm incident excitation, 900μW incident power. 184
B.12 Streak camera image of sample N2676 at room temperature (300 K), 900 nm incident excitation, 100μW incident power. 185
B.13 Streak camera image of sample N2676 at room temperature (300 K), 900 nm incident excitation, 900μW incident power. 185
B.14 Streak camera image of sample N2677 at room temperature (300 K), 900 nm incident excitation, 900μW incident power. 186

List of Tables

2.1 Theoretical limits of multi-junction cells and achieved efficiency 52

4.1 Series resistance values for different components of MJSC 79
4.2 Power enhancement by parameter in each location (%) 94
4.3 Annual Energy Yield (kWh) 95
4.4 Potential efficiencies of different MJSC architectures incorporating a dilute nitride sub-cell. 97

5.1 References for dilute nitride alloy absorption coefficient data reproduced in Figure 5.1 104
5.2 Electroreflectance fitting parameters 110
5.3 Lattice constants of GaAs, GaSb, GaN used for interpolation of GaAsSbN properties 110

6.1 Double heterostructure sample set for time-resolved photoluminescence of GaAsSbN 118

7.1 GaAsSbN device basic sample designs 134
7.2 GaAsSbN device advanced sample designs 134
7.3 Improved device design simulated J_{SC} at > 870 nm 149
7.4 GaAsSbN improved device designs LIV results under AM1.5G unfiltered spectrum 150

A.1 Layer structure of N2264. Device. No antireflection coating. 172
A.2 Layer structure of N2265. Device. No antireflection coating. 173
A.3 Layer structure of N2436. Epilayer on polished substrate. No antireflection coating. 173
A.4 Layer structure of N2623. Device with antireflection coating. 173
A.5 Layer structure of N2627. Device with antireflection coating. 174
A.6 Layer structure of N2760. Double heterostructure, no antireflection coating. 174
A.7 Layer structure of N2761. Double heterostructure, no antireflection coating. 174
A.8 Layer structure of N2762. Double heterostructure, no antireflection coating. 175
A.9 Layer structure of N2763. Double heterostructure, no antireflection coating. 175
A.10 Layer structure of N2764. Double heterostructure, no antireflection coating. 175
A.11 Layer structure of N2765. Double heterostructure, no antireflection coating. 176
A.12 Layer structure of N2766. Double heterostructure, no antireflection coating. 176
A.13 Layer structure of N2767. Double heterostructure, no antireflection coating. 176
A.14 Layer structure of N2772. Device. No antireflection coating. 177
A.15 Layer structure of N2773. Device. No antireflection coating. 177
A.16 Layer structure of N2774. Device. No antireflection coating. 177
A.17 Layer structure of N2776. Device. No antireflection coating. 178
A.18 Layer structure of N2777. Device. No antireflection coating. 178

Chapter 1

Introduction

1.1 Basics of solar cells

Fossil fuel resources and most renewable resources are derived from processes powered by the sun. Solar cells convert sunlight to electrical power directly and hence offer an elegant and potentially efficient source of power.

Solar cells use the photovoltaic (PV) effect to produce energy. They are specially designed diode devices that produce power when illuminated. A basic cell is made from semiconductor material with a particular absorption threshold - the bandgap energy - below which no light is absorbed. This produces current through the load, determined by the current-voltage (IV) characteristics of the cell under illumination. An example is shown in Figure 1.1. The important electrical parameters of a cell are the short-circuit current, I_{SC}, open-circuit voltage, V_{OC}, and P_{max}, maximum power. The maximum power occurs at a point where the product of current and voltage is maximised. The ratio of the electrical power output to the optical power input defines the cell's efficiency.

A multi-junction solar cell is composed of several solar cells of different bandgap energies connected in series.

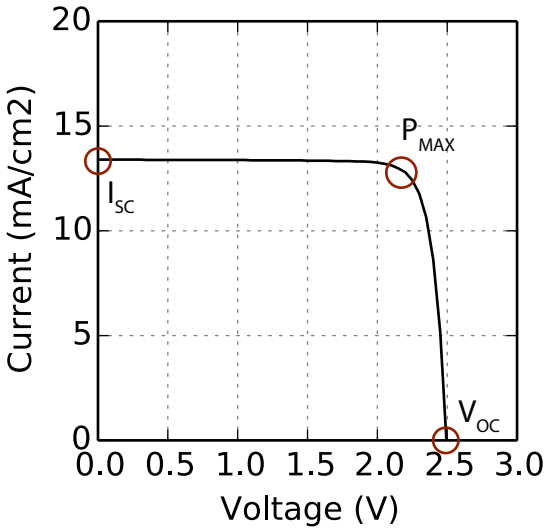


Figure 1.1: IV curve of a triple-junction solar cell. The important parameters of a cell are marked on the graph. The short-circuit current, I_{SC}, is where voltage is zero. Open-circuit voltage, V_{OC}, is where current is zero. P_{max} is maximum power.

1.1.1 Fundamental limits

One of the most prominent concepts in PV research is the Shockley-Queisser limit [1]. Using the detailed balance model in which materials emit a photon for every one they absorb, it considers a material that absorbs all photons above a given energy threshold. This sets an upper bound to single cell PV efficiency based on the assumption that all recombination is radiative and that the sun and the cell radiate as blackbodies with temperatures of 6000 K and 300 K respectively. This upper bound is found to be 31% at a band-gap of 1.1 eV (close to that of silicon) and without concentration of illumination.

Besides raising efficiency by concentrating sunlight, a number of device concepts have been proposed that could exceed the Shockley-Queisser limit, such as the hot carrier solar cell, intermediate band solar cell and the multi-junction solar cell [2]. Each of these is accompanied by a redefined limit and of these, the multi-junction cell has been the most

successfully implemented to date with record efficiencies of 38.8% for one sun and 46% under concentration [3]. It should be noted that while single junction research cells are approaching their theoretical limit, with a GaAs cell recently achieving 28.8% efficiency [3], multi-junctions have much room for improvement.

A detailed analysis of the magnitude of each intrinsic loss mechanism leading to the Shockley-Queisser limit can be found in [4].

1.1.2 The solar spectrum and concentration

The solar spectrum takes a distribution somewhat similar to blackbody radiation (at 5800 K) - a terrestrial version is shown in Figure 1.2. There are several standardised spectra available for solar irradiance including Air Mass 0 (AM0) (extraterrestrial), AM1.5G (terrestrial global irradiance) and AM1.5D (considering direct components for concentrator use). Air mass represents the path length through the atmosphere and quantifies the attenuation of light due to the atmosphere. Most cells are designed with one of the three standard spectra above in mind but in practice cell performance will vary due to location and atmospheric conditions. Variations in the spectrum of incident light can greatly affect multi-junction solar cells and this is discussed further in Chapter 4 below. As well as air mass, aerosols and precpitable water are important variables in the deviation of real spectra from standard spectra [5].

Reproducing the solar spectrum in laboratory conditions can be challenging, and solar simulators are rated for their closeness to the solar spectrum, temporal stability and spatial stability.

Concentration of sunlight leads not only to an increase in the input energy to the cell but also the efficiency at which it is converted.

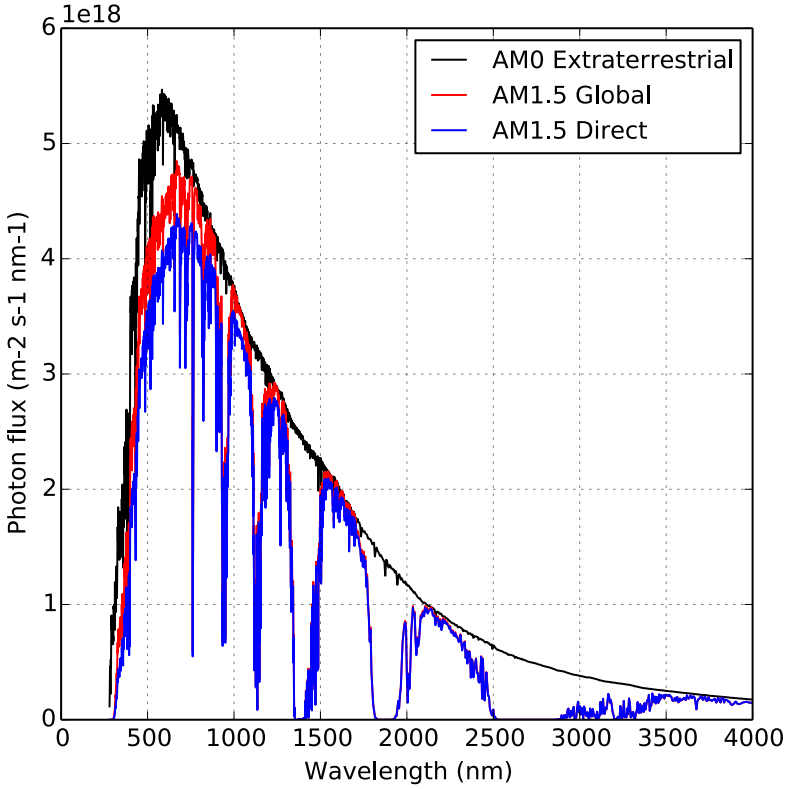


Figure 1.2: The solar spectrum for different air masses. The difference between extraterrestrial AM0 spectrum and terrestrial versions is caused by atmospheric absorption.

1.2 Applications of III-V solar cells

In terms of the fast-growing implementation of terrestrial solar generation, silicon-based technology greatly dominates the market, followed by 'thin film' technologies such as CIGS (Copper Indium Gallium Selenide) and CdTe. There are various reasons for this relating to cost and manufacturing. However, III-V compound semiconductors and related materials offer a number of advantages over these technologies in terms of physical performance, with the best GaAs cells outperforming the best Si cells since the 1970s and still maintaining a 3.5% absolute efficiency advantage (see Figure 1.3, [6]). Despite this superior performance, material costs have prevented the widespread implementation of

this technology for terrestrial electricity generation.

Due to the number of compounds and alloys available, III-V materials are also easily used in multi-junction solar cells (MJSCs) - a stack of different bandgap materials ordered with larger bandgaps on top (see Figure 1.4) that provide fundamentally higher efficiency than single junction cells [7]. The current record for efficiency is held by a quin-junction cell with 38.8% power conversion efficiency, compared to the leading Si cell of 25.6% [3]. In practice MJSCs are often characterised under concentrated illumination, raising the efficiency, with the current record solar cell having a 46% conversion efficiency under concentration [3]. Importantly, there remains a greater discrepancy between potential and achieved efficiency for MJSCs than for single junction cells, making them an interesting research topic.

In addition to exhibiting higher efficiency, III-V solar cells also benefit from high radiation tolerance and relatively low temperature sensitivity [8, 9]. The fabrication techniques used can lend themselves to substrate removal, but even without this step, cells can be much thinner and lighter than their Si counterparts. This is largely due to the fact that III-V compounds are often direct bandgap materials compared to the indirect bandgap Si, and therefore more photons can be absorbed for a given thickness of material. These properties have led to III-V solar cells being the dominant technology used in space power applications, where the cost of solar cell material is marginal compared to the cost of launch per unit weight.

Due to the vast difference in fabrication cost of semiconductor material between III-V-based MJSCs and Si cells, concentrator photovoltaics (CPV) has been proposed as a generation method that uses high performance MJSCs while maintaining a low levelised cost of electricity [10, 11]. In CPV, the cell is one component of a system designed to minimise semiconductor area, and hence cost, by using lenses and/or mirrors to focus light onto a cell, simultaneously increasing the incident power on the cell and the efficiency at which that power can be converted into electricity.

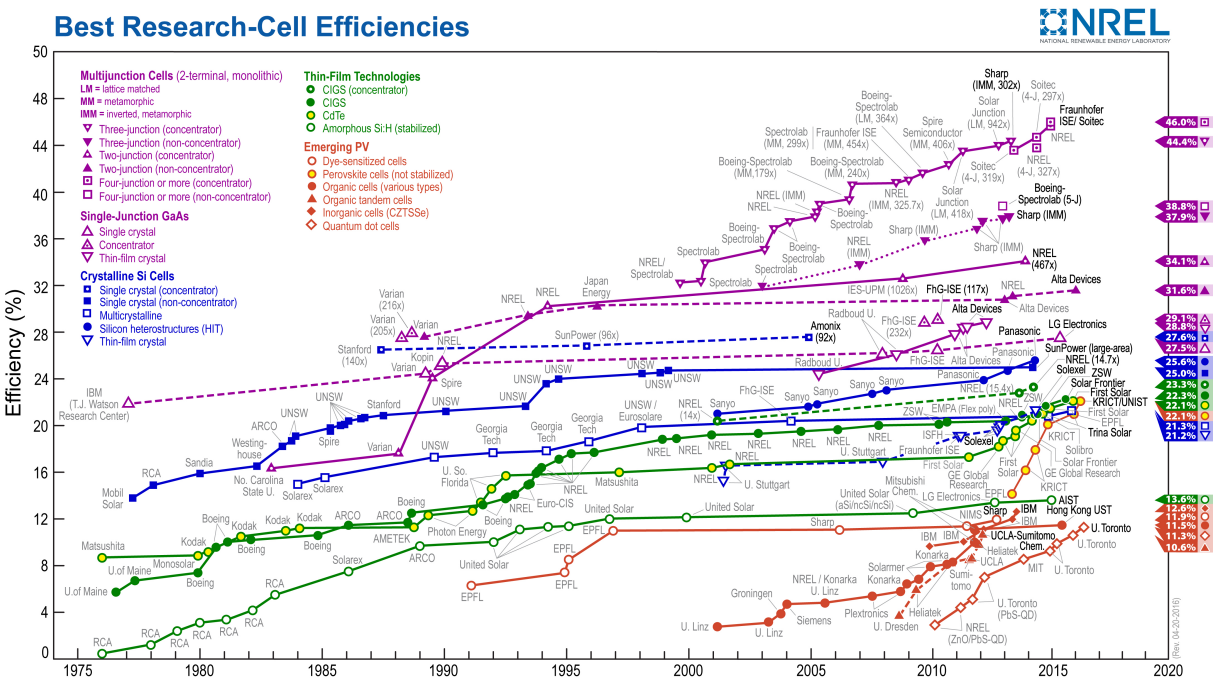


Figure 1.3: History of solar cell record efficiencies as recorded by the United States of America National Renewable Energy Laboratory. Note the advantage to efficiency of single junction GaAs over Si, as well as the rate of increase in MJSC efficiency compared to single junction GaAs and Si. The current record of 46% under concentration is held by a MJSC. This plot is courtesy of the National Renewable Energy Laboratory, Golden, CO.

CPV has faced many challenges to commercialisation. Both increased cell efficiency and increasing the concentration under which the cells operate should help to reduce costs relative to performance. Additional reductions in cost may come from manufacturing techniques, such as use of larger substrates. There is also the question of overall system design and reliability. For example, using several materials of different bandgaps in a MJSC can increase the spectral sensitivity of the cell and affect output due to variation of atmospheric conditions. This effect can also be mitigated with very high quality materials [12]. Besides the main routes of reduction of cost and increase in performance, it is also

helpful to have several possible configurations of materials capable of operating at high efficiencies. For this reason, several routes toward a particular sub-cell of 1 eV are being explored, one of which will be discussed in this thesis.

The following summarises the requirements of the two main applications of III-V solar cells:

Requirements of space applications:

- Radiation tolerant,
- Low mass,
- Low temperature sensitivity.

Requirements of CPV applications:

- Low-cost volume manufacturability,
- Low temperature sensitivity,
- Appropriate to local spectrum.

Most of the content in this thesis relates to the material and device properties of GaAsNSb, a quaternary alloy material capable of producing a range of bandgaps of interest for sub-cells in future MJSC designs. However, this will be placed into context for potential application in CPV, with attention paid to overall MJSC design, consideration of effects present under high concentration, and a brief discussion of spectral sensitivity.

1.3 Multi-junction solar cells

1.3.1 Structure of multi-junction solar cells

Unlike a simple photovoltaic cell based on a single junction, multi-junction solar cells use several junctions of different bandgap materials. The junctions are ordered with higher bandgaps on top and lower bandgaps below, allowing them to sequentially absorb photons from higher to lower energies. Connecting the sub-cells in electrical series produces a high voltage due to the summed voltage of each sub-cell. The attainable voltage for a given current exceeds that possible with a single junction and provides a fundamental efficiency advantage for multi-junction cells. However, fully exploiting this efficiency advantage requires additional engineering complexity. A major concern is that due to the series connection, the current of the device is limited to that of the lesser current producing sub-cell in the stack. This leads to an optimal set of bandgaps for a given input spectrum.

A schematic of a triple-junction solar cell is shown in Figure 1.4 and may be broken down into the following components:

Active layer The active layers in each sub-cell are responsible for photon absorption, subsequent photocurrent generation and voltage through the photovoltaic effect. The active layer of each junction is composed of the depletion region and a thickness of material equivalent to the minority carrier diffusion length. Usually a thick, lower doped base layer is used for the bulk of the absorption, with a thinner, highly doped 'emitter' layer on top. These are usually configured as *n-on-p* junctions in conventional MJSCs in order to benefit from the greater lifetime of minority electrons in the *p*-type base and the greater majority carrier conductivity at the top of the cell. Recently, an interesting variation in which the *n*-type emitter is the thick, absorbing region has been proposed [13] due to advantages in certain situations.

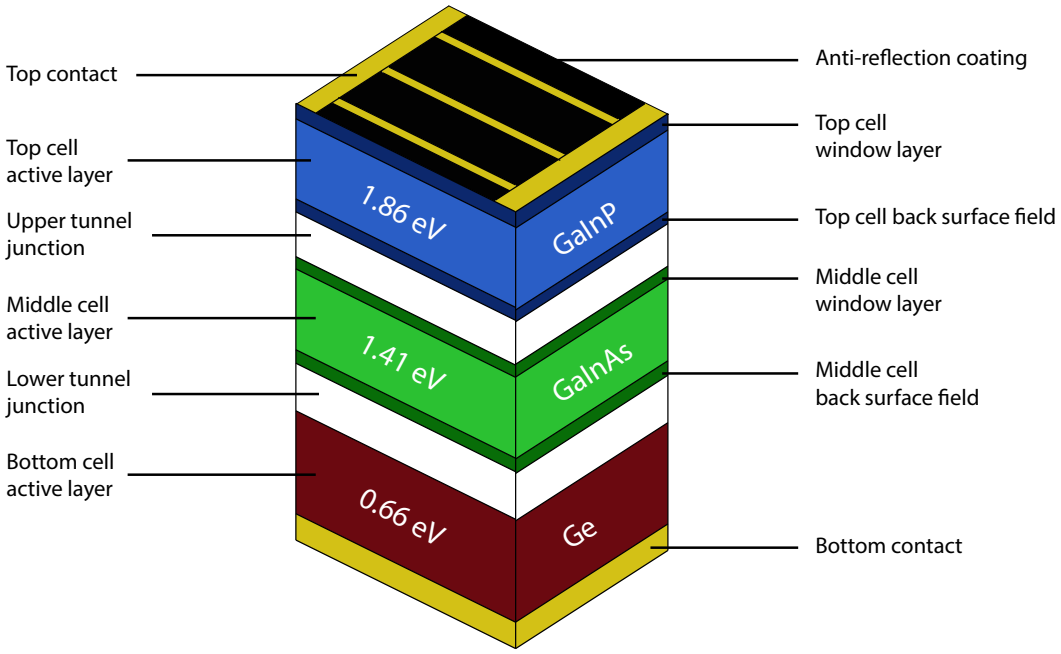


Figure 1.4: Schematic of a triple-junction solar cell with key constituent layers labeled. The labeled materials and bandgaps are that of the more conventional triple-junction architecture based on an active Ge substrate bottom cell. A 1 eV bottom cell from material such as GaAsSbN would be more optimal.

Window layer and back-surface field Layers either side of the junction act to reduce minority carrier recombination at the surfaces of the junction. The layer on top of the junction is known as the window layer, whereas the layer underneath the junction is known as the back-surface field. This occurs not only through passivating otherwise-exposed dangling bonds but by using either doping or material composition variation to provide an energetic disincentive to carriers diffusing towards the surfaces.

Tunnel junction In the vast majority of cases electrical connection between sub-cells is provided by tunnel junctions, with the advantages of maintaining the structural integrity of a monolithic semiconductor device and allowing the entire semiconductor content of

the device to be deposited without interruption. Tunnel junctions require highly doped, thin layers of material with precise, abrupt doping profiles. They have a highly non-linear current-voltage characteristic and are very important for maintaining effective operation under high concentration. The tunnel junction can be a source of series resistance power loss.

Anti-reflection coating Anti-reflection coatings are applied to the front surface of the cell and act to reduce the refractive index contrast between the air and semiconductor interface. Typically these involve multi-layer coatings with thicknesses tailored to providing reflectance minima at desirable wavelengths for balancing the sub-cell photocurrents. Application of appropriate anti-reflection coating can substantially reduce reflections compared to bare semiconductor. As MJSCs incorporate more junctions, the anti-reflection coating (ARC) must be effective over a broader wavelength range, leading to more complex multi-layer designs [14, 15].

Top contact grid and rear contact Due to the use of tunnel junctions to provide inter-sub-cell electrical connection, it is most common to have two terminal MJSC configurations. This ideally is made with a suitable metal making Ohmic contact through a highly doped semiconductor capping layer. Although the back contact is usually simply a planar sheet of metal, the design of the front contact is very important. Obscuration of the active area of the device must be minimised, yet the sheet resistivity of the surface semiconductor layers can introduce a series resistance power loss due to lateral current spreading. This concern is particularly important under concentration, leading to attempts to optimise grid design [16, 17].

1.4 Lattice-matched multi-junction solar cells

The most prevalent, commercialised MJSC structure is the lattice-matched GaInP/GaInAs/Ge triple-junction cell with 1.88/1.41/0.66 eV bandgaps [9], developed from depositing GaInP/GaInAs dual-junctions onto active Ge substrates. This has achieved efficiencies of 44% under 250 suns concentration in commercially available cells [8]. A major loss mechanism in this structure is the sub-optimally low bandgap of the Ge cell. The current produced in Ge is far greater than the upper two sub-cells but is not useful for electrical power due to the current-matching constraint. Sub-cell voltages are limited by the bandgap, and so the bandgap can be raised to the point at which all three sub-cells are current-matched, increasing efficiency. The optimal bandgap energy for this lower sub-cell is around 1 eV. Several approaches have been attempted to solve this problem, including:

Lattice-matched materials The standard lattice-matched solar cell has been based on Ge substrates, nearly lattice matched to GaAs. The possible binary and ternary combinations of III-V compounds and alloys (as well as germanium) in the lattice constant region of GaAs are shown in Figure 1.5. The standard lattice-matched triple-junction cell has been composed of GaInP/GaInAs/Ge cells with 1.88/1.41/0.66 eV bandgaps.

Using these conventional materials there is no possibility of producing a lower bandgap than GaAs with the same lattice constant. However, this energy range is of great interest to multi-junction solar cells in terms of increased efficiency for triple- and quad-junction cells and future designs including more sub-cells. A sub-cell with 1 eV has been identified as a particular priority and can be produced from dilute nitride alloys of GaAs.

Nitrogen has an anomalously large effect on bandgap when added in dilute quantities to GaAs-like materials. Adding strain-balancing elements such as In and/or Sb can create compounds lattice-matched to GaAs with a range of bandgap energies between 1.4 eV and 0.8 eV. The dilute nitride quaternary GaAsSbN will be the topic of most of this thesis.

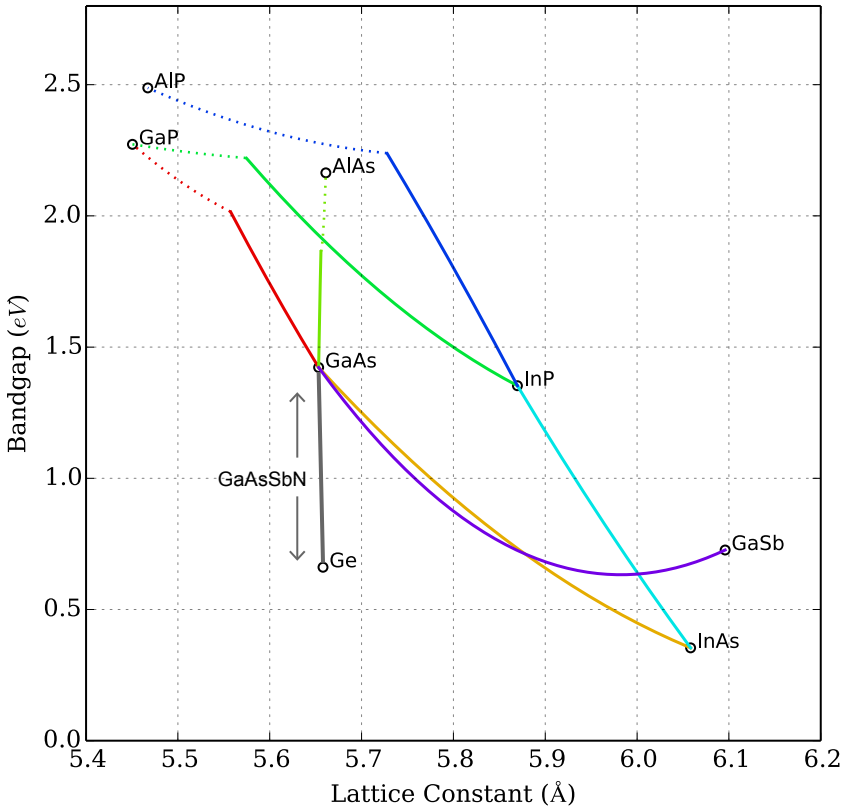


Figure 1.5: Lattice constant and bandgap for several binary compounds and ternary III-V alloys, as well as germanium and GaAsSbN. The coloured lines indicate lattice constant and bandgap as a function of ternary composition i.e. the line between GaAs and InAs describes GaInAs. Solid lines indicate direct gap materials whereas dotted lines indicate indirect gap materials. III-V parameters are calculated using data and suggestions given in [18]. Note the lack of conventional materials lattice-matched to GaAs or Ge with lower bandgap than GaAs. Dilute nitrides such as GaAsSbN can fill this parameter space.

For many years dilute nitride materials were found to have inadequate minority carrier diffusion lengths to improve on Ge-based triple-junctions. However, eventually triple junction solar cells with a 1 eV GaInAsSbN bottom cell achieved a record 44.1% efficiency [19] - still the record efficiency for an all-lattice-matched cell. Other proposals for lattice-

matched bulk materials for the lower sub-cells of future MJSC designs are Bi-containing compounds [20] and the group IV alloy SiGeSn [21].

Alternative fabrication techniques The perceived lack of lattice-matched materials with desirable bandgaps has been circumvented by using metamorphic growth techniques, in which thick buffer layers are grown to gradually switch from one lattice constant to another. Materials with different lattice parameters can then be monolithically grown. Despite the challenge of maintaining the quality of the subcells grown above the buffer layer, this approach successfully produced an 'upright metamorphic' cell in which the upper two sub-cells have their bandgaps lowered to compensate for the low bandgap of Ge [22]. Another successful variation of this is the 'inverted metamorphic' (IMM) growth technique in which the upper sub-cells are grown first, lattice-matched to GaAs with high material quality. The highest bandgap sub-cell is grown first, followed by the middle cell. This is followed by growth of buffer layers to transfer to the appropriate lattice constant, followed by the incorporation of a 1 eV GaInAs sub-cell into the device [23]. The device is then flipped and the substrate removed. This technique preserves material quality in the higher bandgap, higher voltage sub-cells while sacrificing the material quality of the lower voltage sub-cell, helping to maintain high efficiency. This technique has also produced very high efficiency quad-junction 'double IMM' cells with two metamorphic buffer regions and 1.0 eV and 0.7 eV GaInAs lower sub-cells [24]. However, there is extra cost to this processing complexity compared to lattice-matched monolithic growth as well as issues of manufacture yield.

A third way of fabricating high efficiency solar cells has been demonstrated in recent years: mechanically bonding sets of sub-cells grown on two different substrates with different lattice constants. This has the advantage of high material quality in every sub-cell and indeed the current record efficiency cell is a quad-junction wafer bonded structure containing two sub-cells grown on GaAs and two grown on InP [25]. However,

there is extra cost and processing complexity for this method. For example, larger area InP substrates are currently unavailable, and current InP substrates are expensive.

1.5 Outline of this thesis

Chapters 2 and 3 presents the theory and experimental methods used in the remaining chapters. Chapter 4 addresses the future direction of MJSCs through simulation and modeling of current state-of-the-art architectures and the associated loss mechanisms. In the remaining chapters, a candidate for a lattice-matched lower sub-cell material, 1 eV GaAsSbN, is evaluated in terms of material and device properties for its suitability in improving the current commercial standard of GaInP/GaAs/Ge cells. The main context considered will be for application to terrestrial CPV systems. Increased efficiency and lattice-matched growth may reduce cost and enhance the commercial prospects of high efficiency solar cells.

With the development of the quad-junction cell identified as the next step for the industry, this thesis will consider the challenges of reaching 50% efficiency. Models that consider the device physics of MJSCs will be used to demonstrate methods by which efficiency can be improved. The experimental work will focus on the material properties of GaAsSbN, a quaternary dilute nitride alloy that can exhibit a range of bandgaps useful for MJSCs while remaining lattice-matched to the common GaAs or Ge substrates. In Chapter 5 the absorption properties of the material are studied and evaluated using a model dielectric function and interpolation across material composition. In Chapter 6 the recombination mechanisms of the material are investigated and the minority carrier lifetime is measured for a range of samples. Chapter 7 reports device results for several designs and compares them to the necessary performance criteria established in Chapter 4. Possible improvements and limits to the material are identify. Conclusions are given in Chapter 8.

Chapter 2

Theory and previous work

2.1 Absorption and emission in semiconductors

The threshold of absorption of photons by semiconductor material is characterised in the most simple terms by a bandgap energy. Photons with energies above this value can be absorbed, promoting an electron from valence band to conduction band, whereas the material will appear transparent to photons with energies below the bandgap. This process can be macroscopically described by the complex and frequency dependent refractive index of the material. Semiconductor materials can be classified as either direct gap or indirect gap based on the nature of the lowest energy transition of the material. At the point of their fundamental energy gap (the lowest energy at which a photon can be absorbed), direct gap materials simply absorb a photon through imparting energy to an electron, as described above. Indirect materials involve momentum exchange with phonons in addition to energy exchange. Direct gap materials therefore absorb more strongly per unit volume close to the band edge. GaAsSbN is a direct gap material and so the following discussion will be specific to direct gap semiconductors. It is possible however, for both direct gap and indirect gap materials to have transitions of the other type that occur at higher energies than the fundamental energy gap.

Properties such as radiative recombination and the quantum efficiency (the ratio of the number of electrons extracted from the device to photons absorbed) of a cell are strongly linked to the optical constants of the cell - absorption coefficient and refractive index. These are dependent on the band structure and optical transitions within the semiconductor. III-V compound semiconductors have relatively high refractive index, with GaAs having an index of around 3.6 [26]. Accurate modeling of optoelectronic device performance must take into account the band structure and complex dielectric function of materials and several data sources and analytical functions are available, including methods that use material-specific parameters in a general form of model dielectic function [27]. Although tabulated data is available for common materials such as GaAs, in more complex materials such as GaInP (a common top cell material) the absorption is dependent on the degree of alloy ordering [28] and so it is not always straightforward to use tabulated data. Models can be particularly useful in determining the absorption coefficient of such materials. This is also the case for quaternary materials and the absorption properties of GaAsSbN will be investigated in this project by developing a model dielectric function based on experimental measurements.

In the physics of optoelectronic devices, it is often useful to begin by considering macroscopic absorption properties.

Eq. (2.1) defines the phenomenological, macroscropic absorption cofficient of light incident normal to the surface of a material. This is also known as the Beer-Lambert law.

$$\alpha(\omega) = -\frac{\mathrm{d}I(\omega)}{\mathrm{d}x}\frac{1}{I(\omega)} \tag{2.1}$$

α is the absorption coefficient, ω is the incident photon frequency, I is the incident radiant flux, x is the thickness of material.

If the absorption coefficient is known, the fraction of light absorbed (known as absorbance) can be expressed as:

$$A(\omega, x) = \log_{10} \frac{I(\omega)}{I_0} = \exp(-\alpha x) \tag{2.2}$$

where I_0 is the initial incident radiant flux.

Emission is the reciprocal process of absorption. In semiconductor devices there are fundamental, reciprocal links between the absorption properties of a device working as a solar cell and the emission properties of the same device working as a light emitting diode [29]. Radiative recombination of electrons and holes is a source of photon emission in any optoelectronic device. The absorption, emission and recombination properties of a material or device are therefore linked and dependent on the band structure and dielectric function of the material.

2.1.1 Band structure

Electronic and optical properties of semiconductors are dependent on the band structure of that specific material. Macroscopic optical properties such as absorption can be determined from the microscopic dielectric function, which is determined by the band strucure [30]. The dispersion of the dielectric function is dependent upon the joint density of states between valence and conduction band, which is usually determined at critical points in the band structure (known as van Hove singularities). These are points at which the density of states diverges. Several types of critical points are possible such as band separation minima, maxima or saddle points [30].

Several theoretical formalisms are available for calculating band structure of materials. The most simple is the assumption of parabolic bands, from which a number of results follow analytically. The link between band structure and absorption for a simple case of a pair of parabolic, isotropic conduction and valence bands is demonstrated below.

Firstly, a simple parabolic band dispersion will follow Eq. (2.3):

$$E_C(k) = E_g + \frac{\hbar k^2}{2m^*} \tag{2.3}$$

Where E_C is the conduction band, E_g is the energy gap, k is the reciprocal space vector and m^* is the effective mass of a carrier in that band i.e. electron effective mass in the case of the conduction band.

The effective mass also determines the densities of states, with the joint density of states for optical transitions between two bands being given by:

$$J_{cv}(\omega) = \frac{1}{2\pi^2}(\frac{2\mu}{\hbar^2})^{\frac{3}{2}}(\hbar\omega - E_g)^{\frac{1}{2}} \tag{2.4}$$

Where $\hbar\omega$ is the incident photon energy and μ is the reduced effective mass, given by:

$$\frac{1}{\mu} = \frac{1}{m_e^*} + \frac{1}{m_h^*} \tag{2.5}$$

where m_e^* and m_h^* are the electron and hole effective masses respectively.

The absorption coefficient is then proportional to the joint density of states [31]:

$$\alpha(\omega) = \|M\|^2 \frac{\pi q^2}{n_r c \epsilon_0 m_e^{*2} \frac{E_g}{\hbar}} J_{cv} \tag{2.6}$$

The $\|M\|^2$ parameter, the matrix element, is dependent on the effective masses, bandgap of the material and the overlap between wavefunctions of the two states. n_r is the refractive index of the material, c is the speed of light in a vacuum and ϵ_0 is the vacuum permitivitty constant.

Therefore, the absorption coefficient has a dependence on photon energy:

$$\alpha(\omega) \propto (\hbar\omega - E_g)^{\frac{1}{2}} \tag{2.7}$$

With the other terms in Eq. (2.6) being material dependent constants.

Although this single transition dipole approximation model is instructive, it is not always accurate in terms of reproducing real material absorption coefficients over a wide range of energy. This is because contributions from several transition points can occur for a given material and photon energy. These transitions may have different form to that described above.

For more complex band structures, it is common to use a semi-empirical parametric model to link transitions at multiple transitions in the band structure to the complex refractive index of the material using a model dielectric function. The dielectric function then determines the absorption coefficient. Information about the critical points and the refractive index may be obtained experimentally. This will be applied to GaAsSbN in Chapter 5.

2.1.2 Model dielectric functions

The optical properties of III-V semiconductor materials can be predicted using a semi-classical model that considers a dipole oscillator and parameterises the dielectric function based on the nature of various critical points in the band structure. The parameters related to these critical points - energy location, amplitude, broadening - can be measured through experiment. In this way analytical expressions for the dielectric function can be found through a summation of oscillators equivalent to contributions from different direct transitions, indirect transitions, or exciton effects. The dielectric function then determines the optical properties n, k (extinction coefficient) and α. For alloys, this may be taken further by introducing analytical expressions of interpolation for these parameters as a function of alloy composition. This is of great use in the design of optoelectronic devices. Below is described a model dielectric function method that has been applied to the optical dispersion relations of a variety of common III-V compounds and alloys [31]. This type of model is applied to GaAsSbN in Chapter 5. First we consider the complex dielectric function:

$$\epsilon(\omega) = \epsilon_1 + i\epsilon_2 \tag{2.8}$$

The imaginary part of the dielectric function, ϵ_2 is derived from the joint density of states at the band structure critical point [31]:

$$\epsilon_2(\omega) = \frac{4\hbar q^2}{\pi m^{*2}\omega^2}|(< c|p|v >)|^2 J_{cv}(\omega) \tag{2.9}$$

With J_{cv} as the joint density of states between valence and conduction band. This is comparable to Eq. (2.6) above but with the conduction and valence band explicitly defined as the states of the matrix element. The real part of the dielectric function can be obtained through a Kramers-Kronig transformation of Eq. (2.9):

$$\epsilon_1(\omega) = 1 + \frac{2}{\pi}\int_0^{\inf} \frac{\omega'\epsilon_2(\omega)}{(\omega')^2 - \omega^2} d\omega' \tag{2.10}$$

The contribution from the fundamental direct bandgap transition, labelled E_0 with split-off energy Δ_0, is given by:

$$\epsilon_2(\omega) = \frac{A}{(\hbar\omega)^2}(\hbar\omega - E_0)^{\frac{1}{2}} H(\frac{\hbar\omega}{E_0} - 1) + \frac{1}{2}(\hbar\omega - E_0 - \Delta_0)^{\frac{1}{2}} H(\frac{\hbar\omega}{E_0 + \Delta_0} - 1) \tag{2.11}$$

$$\epsilon_1(\omega) = AE_0^{-1.5}\{f(\chi_0) + \frac{1}{2}[\frac{E_0}{E_0 + \Delta_0}]^{1.5} f(\chi_{so})\} \tag{2.12}$$

Where A is the amplitude and E_0 the energy of the transition. $H(z)$ is a Heaviside function which $= 1$ for $z > 0$ and 0 if $z < 0$. The function $\chi_0(\omega) = \frac{\hbar\omega}{E_0}$ and $\chi_{so}(\omega) = \frac{\hbar\omega}{E_0 + \Delta_0}$. The function $f(\chi) = \chi^2[2 - (1+\chi)^{0.5}(1-\chi)^{0.5} H(1-\chi)]$.

The full model contains further contributions from the E_1, $E_1 + \Delta_1$ and E_2 transitions that have different general form, described in [27]. The E_1 and $E_1 + \Delta_1$ gap contributions to the dielectric function are given by:

$$\epsilon_2(\omega) = \pi(B_1\chi_1^{-2} H(\chi_1 - 1) + B_2\chi_{1s}^{-2} H(\chi_{1s} - 1)) \tag{2.13}$$

$$\epsilon_1(\omega) - 1 = -B_1\chi_1^{-2}ln(1-\chi_1^2) - B_2\chi_{1s}^{-2}ln(1-\chi_{1s}^2) \tag{2.14}$$

Where B_1 and B_2 are material specific parameters, $\chi_1 = \frac{\hbar\omega}{E_1}$, $\chi_{1s} = \frac{\hbar\omega}{E_1+\Delta_1}$.

The $E2$ structure is characterised as a damped harmonic oscillator:

$$\epsilon_2(\omega) = \frac{C\chi_2\gamma}{(1-\chi_2^2)^2 + \chi_2^2\gamma^2} \tag{2.15}$$

$$\epsilon_1(\omega) - 1 = \frac{C(1-\chi_2^2)}{(1-\chi_2^2)^2 + \chi_2^2\gamma^2} \tag{2.16}$$

Where C represents the strength of the interaction between the oscillator and the photon and γ is the damping factor.

Additionally, it is found by the author of the model that an indirect contribution is required and that excitonic effects are not notable at room temperature [27]. The results of the full calculation using parameters for GaAs can be seen in Figure 2.1.

The complex refractive index $n + \mathrm{i}k$ can then be obtained through:

$$n(\omega) = \Big(\frac{[\epsilon_1(\omega)^2 + \epsilon_2(\omega)]^{0.5} + \epsilon_1(\omega)}{2}\Big)^{0.5} \tag{2.17}$$

$$k(\omega) = \Big(\frac{[\epsilon_1(\omega)^2 + \epsilon_2(\omega)]^{0.5} - \epsilon_1(\omega)}{2}\Big)^{0.5} \tag{2.18}$$

And finally the absorption coefficient from:

$$\alpha(\omega) = \frac{4\pi k(\omega)}{\lambda} \tag{2.19}$$

Where λ is the wavelength corresponding to photons with energy $\hbar\omega$. These properties are calculated for GaAs and shown in Figure 2.2, with a comparison of the absorption coefficient to experimental data [32]. A variation of this model dielectric function is applied to GaAsSbN in Chapter 5.

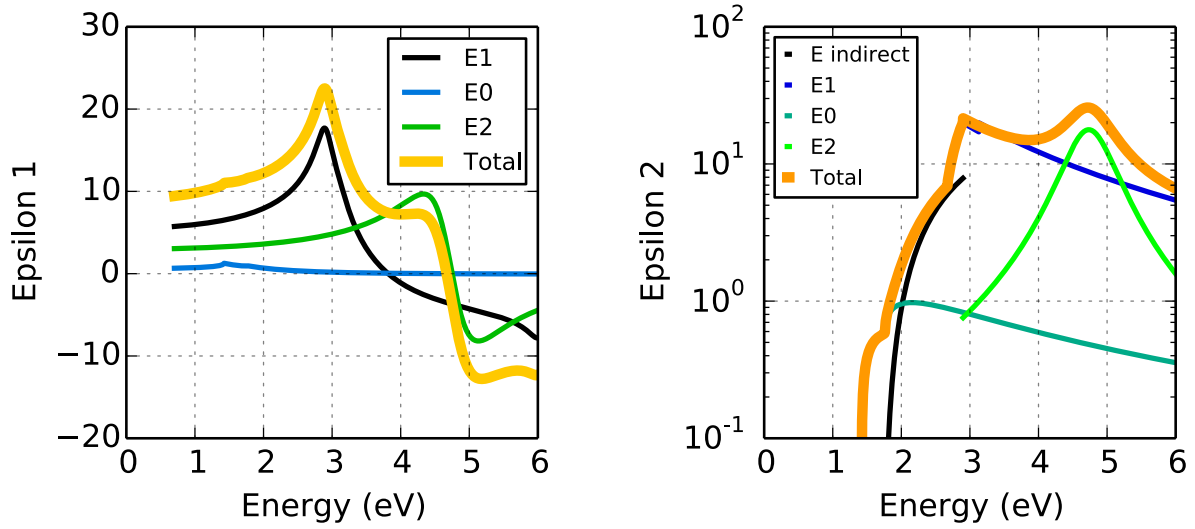


Figure 2.1: Calculation of the dielectric functions ϵ_1 and ϵ_2 of GaAs based on parameters given in [27]. The contributions of different transitions, E_0, E_1 etc., are shown as well as the total dielectric function.

2.2 Electron and hole recombination in semiconductors

Recombination of electrons and holes in semionductors constitutes a loss mechanism for solar cells. Three main mechanisms are considered in direct gap III-V materials:

- radiative recombination, in which electrons and holes recombine band-to-band, emitting a photon close to the bandgap energy,
- non-radiative recombination of the two carrier type, linked to defects in the material,
- three carrier Auger recombination.

All three recombination mechanisms are illustrated in Figure 2.3. Radiative and Auger recombination are unavoidable in any device or material, although partly design depen-

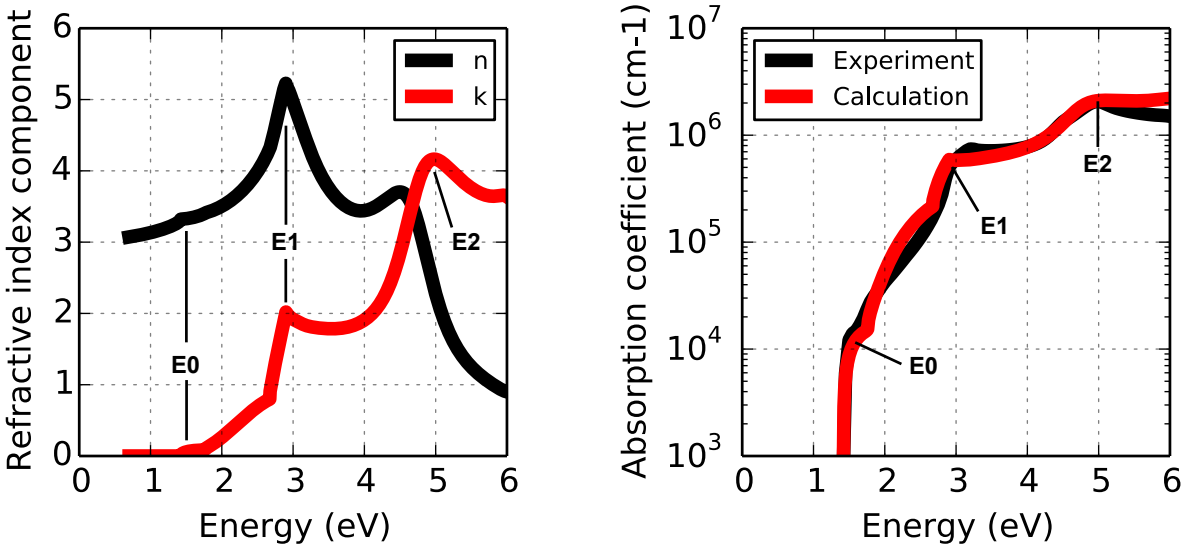


Figure 2.2: (Left) Calculation of the refractive index and extinction cofficient n and k of GaAs based on [31]. (Right) The calculated absorption coefficient of GaAs compared to experimental data [32]. Contributions from different energy transitions in the band structure are indicated in both plots.

dent. Non-radiative Shockley-Read-Hall (SRH) recombination occurs through recombination centres, defects and disorder in crystalline material quality.

2.2.1 Radiative recombination

Band to band radiative recombination is the reverse process of the creation of an electron-hole pair through absorbing a photon - i.e. a minority carrier electron or hole is lost and energy is released in the form of a photon. It is the process through which a light emitting diode functions. It is intrinsic to a given sample or device.

The rate of radiative recombination is determined by the excess concentration of both types of carrier above the equilibrium carrier concentration as well as a material specific constant:

$$U_{rad} = B(np - {n_i}^2) \tag{2.20}$$

Where U_{rad} is the net rate of recombination (m^{-3} s^{-1}), n and p are the electron and hole concentrations, n_i is the intrinsic carrier concentration and B is a material specific parameter dependent upon the joint density of states for optical transitions.

A general equation for the emission of radiative recombination from semiconductors is the generalised Planck equation [33]:

$$\phi(V, E) = \frac{2\pi E^2}{h^3 c^2} \frac{a(E)}{exp((E - qV)/k_B T) - 1} \tag{2.21}$$

where ϕ is the emitted photon flux of photons of energy E for a cell under bias V, h is the Planck constant, c is the velocity of light in vacuum, $a(E)$ is the absorptance and emissivity of the solar cell, and $k_B T$ is the thermal energy.

2.2.2 Non-radiative recombination

Non-radiative recombination through recombination centres or surface states is a source of theoretically avoidable loss in solar cells. The extent to which it is present can depend on material quality and device design. Shockley and Read [34] and Hall [35] described recombination through a trap state and this formulation is commonly used to analyse results such as carrier lifetimes.

$$U_{SRH} = \frac{pn - {n_i}^2}{p + n + 2n_i cosh(\frac{E_i - E_t}{k_B T})} N_t v_{th} \sigma \tag{2.22}$$

Here, p and n are the hole and electron concentrations respectively, n_i is the intrinsic carrier concentration, E_i is the energy of the Fermi level and E_t the trap energy location. N_t is the trap density, v_{th} the thermal velocity of the carrier and σ the trap capture cross-section.

For a material with a dominant carrier type such as $p >> n$ this simplifies to:

$$U_n = \frac{n_p n_{p0}}{\tau_n} \tag{2.23}$$

and for $n >> p$:

$$U_p = \frac{p_n p_{n0}}{\tau_p} \tag{2.24}$$

where τ is the minority carrier lifetime, $\tau = \frac{1}{N_t v_{th} \sigma}$. n_p is the concentration of electrons in the p-type material, n_{p0} is the equilibrium concentration of electrons in the p-type material, p_n is the concentration of holes in the n-type material, p_{n0} is the equilibrium concentration of electrons in n-type material.

2.2.3 Auger recombination

Although Auger recombination is a non-radiative process involving three carriers, it is ofen neglected in studies of III-V photovoltaics because of the very low Auger coefficients of III-V materials.

2.3 Semiconductor transport

Solar cells can be described more generally by the semiconductor device equations, for which the ideal diode equation is a particular solution. These are a set of coupled partial differential equations that describe charge transport in semiconductors. First consider Poisson's equation relating electrostatic potential (or an equivalent term for electric field) and charge density:

$$-\nabla^2 \phi = \nabla \vec{E} = \frac{q}{\epsilon_s}(p - n + N_d^+ - N_a^-) \tag{2.25}$$

General continuity equations for electron and hole densities per unit volume can be derived from the Boltzmann transport equation [36] and are given by:

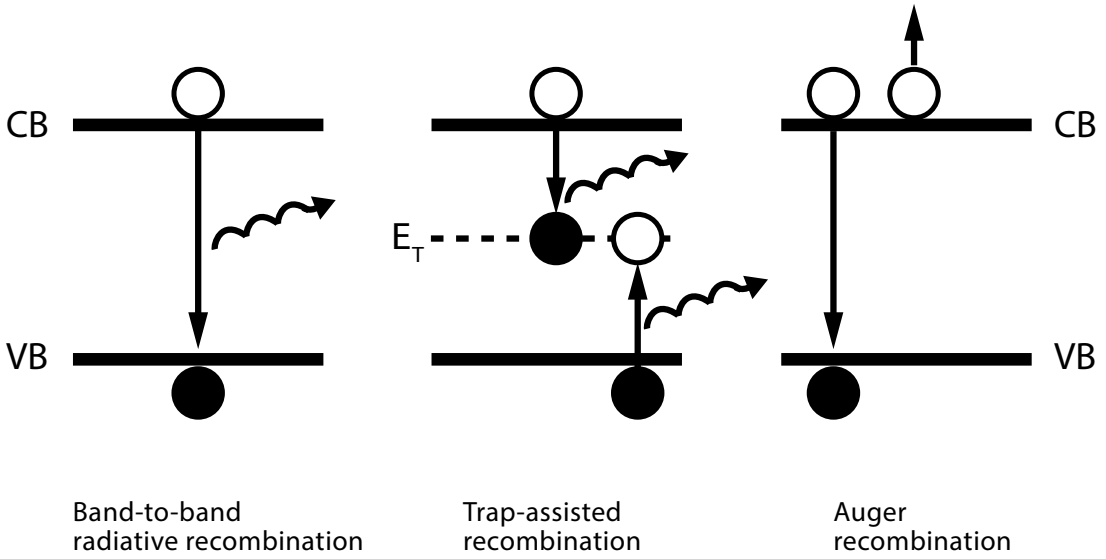


Figure 2.3: Illustration of three carrier recombination processes in III-V semiconductor materials. Generally, Auger recombination is insignificant in applications of III-V photovoltaics. Band-to-band recombination is a radiative process intrinsic to semiconductors. Trap-assisted recombination is generally non-radiative and related to material quality.

$$\frac{\partial n}{\partial t} = \frac{1}{q}\nabla \cdot \boldsymbol{J_n} + G_n + U_n \tag{2.26}$$

$$\frac{\partial p}{\partial t} = \frac{1}{q}\nabla \cdot \boldsymbol{J_p} + G_p + U_p \tag{2.27}$$

And transport equations are:

$$J_n = q(\mu_n n\vec{E} + D_n \nabla n) \tag{2.28}$$

$$J_p = q(\mu_p p\vec{E} - D_p \nabla p) \tag{2.29}$$

For simplicity these equations are often considered in one dimension, with $\nabla \rightarrow \frac{\partial}{\partial x}$ and so on. ϕ is the electrostatic potential, $E(x)$ is the electric field, q is the charge on an electron, ϵ_s is the dielectric constant of the semiconductor, $p(x,t)$ is the hole density, $n(x,t)$ is the electron density, $N_a^-$is the density of ionized donor atoms, N_d^+ is the density of ionized acceptor atoms, t is time, G is the generation term, U is the recombination term, μ is the carrier mobility and D is the diffusion coefficient.

The current has drift and diffusion components, with the terms proportional to μ representing drift current due to electric field (fields go from positive to negative voltage with electrons going the opposite way) and terms proportional to D representing diffusion currents.

A number of simplifications and approximations can be applied to these equations to give useful analytical expressions for device behaviour. The depletion approximation is the most common, in which the device is split into 3 regions; two quasi-neutral regions and a region depleted of free charge carriers, in which there is an electric field. The equations can be solved for the three regions separately to find the minority and majority carrier densities and currents, the generation profile and recombination profile, amongst other properties. By specifying boundary conditions, particular solutions can be found which lead to equivalent expressions to Eq. (2.40). Analytical solutions and numerical 1D drift-diffusion simulation models will be used in this thesis to model experimental data as well as predict potential performance of solar cell designs. The numerical drift-diffusion model was developed by Diego Alonso Álvarez of Imperial College London [37].

2.3.1 The *pn* junction

The most common physical physical implementation of photovoltaic (PV) conversion of sunlight uses the semiconductor *pn* junction. The interface of two differently doped semiconductor layers has asymmetrical properties, as can be seen in the band diagram in Figure 2.5. In a *pn* junction, one layer is doped *p*-type, with acceptor impurities introducing excess holes, while the other layer is doped *n*-type, with donor impurities introducing excess electrons. A variation is the *pin* junction, in which an undoped, intrinsic layer of material features between the two differently doped layers. The absorption of photons with requisite energy will excite electrons from valence band to conduction band of the material. The asymmetry caused by the built-in bias of the *pn* junction causes the electron-hole charge carrier pairs to be separated and driven to different contacts of the device. Their excess energy generates a potential difference that drives them to do electrical work on an externally connected load [38]. Figure 2.4 illustrates how illumination can induce both voltage and current within the *pn* junction. The performance and current-voltage characteristic of a solar cell is therefore greatly dependent on the transport of excess minority carriers.

The depletion approximation can be used to describe of the properties of the junction. The depletion region occurs at the junction under equilibrium. Mobile carriers are depleted near the interfacial region and the space charge of the ionised impurities establishes an electric field. The depletion approximation assumes that the doping profile is uniform and that the interface between this region and the neighbouring quasi-neutral regions is abrupt. The width of the depletion region is determined by:

$$W = (\frac{2\epsilon}{q} V_{bi} (\frac{1}{N_A} + \frac{1}{N_D}))^{0.5} \tag{2.30}$$

N_A and N_D are the acceptor and donor concentrations respectively. V_{bi} is the built-in voltage, the potential across the depletion region at equilibrium, determined by:

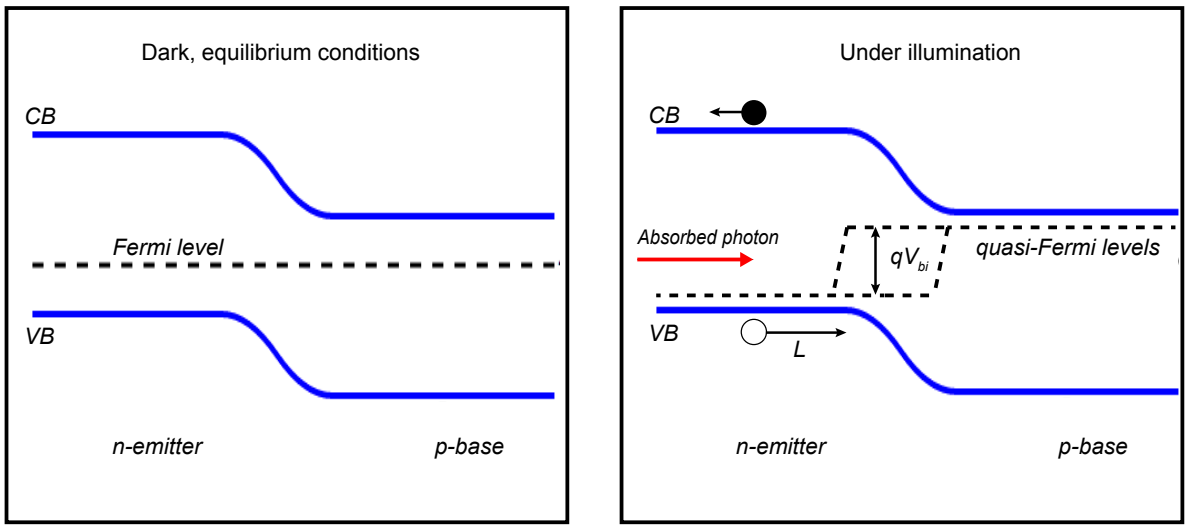


Figure 2.4: Illustration of effect of illumination on minority carrier transport in a *pn* junction. Left: in the dark, under equilbirum conditions, the device has constant Fermi level. Right: under illumination, excess minority carriers are generated, splitting the Fermi level into quasi-Fermi levels. This generates a built-in voltage, V_{bi}, across the junction. Carriers within a diffusion length, L, are collected at the junction, producing current. This is illustrated for a hole generated by photon absorption within the n-type emitter region.

$$V_{bi} = \frac{k_B T}{q} log(\frac{N_D N_A}{n_i^2}) \tag{2.31}$$

where n_i is the intrinsic carrier concentration, itself dependent on the effective masses and bandgap of the material.

The depletion approximation can be useful in investigating whether excess carriers are being transported by the electric field or are diffusing in the non-depleted quasi-neutral regions. In particular, the current contributions from different regions of a device can be

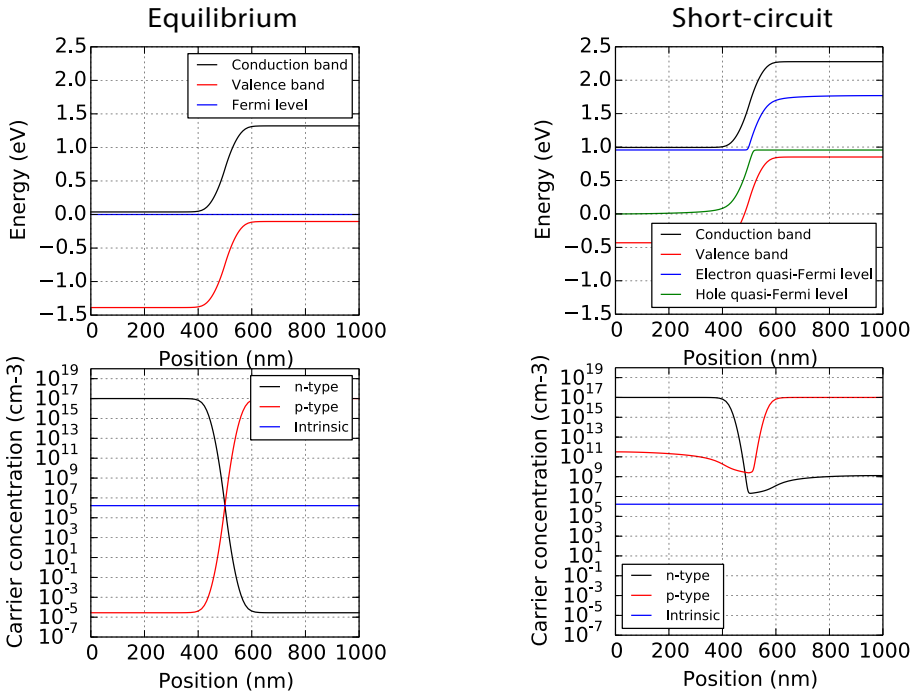


Figure 2.5: Illustration of *pn* junction properties for a 1 μm thick *np* GaAs junction calculated using drift-diffusion modeling. Top left: Energy bands and Fermi level with position under equilibrium conditions. Bottom left: Carrier concentration with position under equilibrium conditions. Top right: Energy bands and Fermi level with position under short-circuit conditions. Bottom right: Carrier concentration with position under short-circuit conditions.

determined by:

$$J_{depletion} = qb_{depletion}(1 - exp(-\alpha_i x_i - \alpha_N w_n - \alpha_P w_p)) \tag{2.32}$$

for the depletion region contribution, in which all carriers are assumed to be collected due to the electric field. $b_{depletion}$ is the photon flux incident on the depletion region, the α terms are the absorption coefficients of the intrinsic (i), n-type and p-type material of the depleted region and the w terms are the widths of the respective sections.

The contributions from quasi-neutral emitter and base material are reliant on diffusion of minority carriers and are given by [38]:

$$J_{emitter} = \frac{qb_s\alpha L}{\alpha^2 L^2 - 1}\left(\frac{\frac{Ls}{D} + \alpha L - e^{\alpha(x-w)}\left(\frac{Ls}{D}\cosh\left(\frac{x-w}{L}\right) + \sinh\left(\frac{x-w}{L}\right)\right)}{\frac{Ls}{D}\sinh\left(\frac{x-w}{L}\right) + \cosh\left(\frac{x-w}{L}\right)} - \alpha L e^{-\alpha(x-w)}\right) \tag{2.33}$$

$$J_{base} = \frac{qb_s\alpha L}{\alpha^2 L^2 - 1}\left(L\alpha - \frac{\frac{Ls}{D}\left(\cosh\left(\frac{x-w}{L}\right) - e^{-\alpha(x-w)}\right) + \sinh\frac{x-w}{L} + L\alpha e^{-\alpha(x-w)}}{\cosh\left(\frac{x-w}{L}\right) + \frac{Ls}{D}\sinh\left(\frac{x-w}{L}\right)}\right) \tag{2.34}$$

Where b_s is the photon flux density incident on that layer of the device (i.e. accounting for absorption in the layers above), L is the minority carrier diffusion length in that layer of the device, s is the surface recombination of that layer of the device, w is the depletion width in that layer of the device, x is the remaining quasi-neutral thickness of the layer, α is the absorption coefficient of the layer. D is the minority carrier diffusion coefficient of the layer:

$$D = \frac{\mu k_B T}{q} \tag{2.35}$$

μ is the carrier mobility:

$$\mu = \frac{L^2}{\tau}\frac{q}{k_B T} \tag{2.36}$$

τ is the minority carrier lifetime.

2.3.2 Quantum efficiency

Although the maximum generation of carriers is determined by photon absorption, even at short-circuit it is possible that not all carriers are collected by the junction. The collected

photocurrent is given by the integral of the product of the total generated current with the quantum efficiency:

$$J_{SC} = q \int b_s(E) EQE(E) dE \tag{2.37}$$

Where J_{SC} is the photocurrent density, q is the charge on al electron, $b_s(E)$ is the flux density of photons of energy in the range E to $E + dE$ that are incident on unit area in unit time, EQE is the cell's external quantum efficiency (the fraction of incident photons of energy E that result in a charge passing through the external circuit). QE is the ratio of electrons extracted from the device to photons incident on a device. It is closely related to spectral response, which is measured in units of A/W rather than as a dimensionless ratio. Eq. (2.38) describes the external quantum efficiency of a solar cell.

$$EQE(\lambda) = \frac{1}{q} \frac{I(\lambda)}{\phi(\lambda)} \tag{2.38}$$

Here λ is the photon wavelength, I is the current measured and ϕ is the incident photon flux on the sample. EQE is the external quantum efficiency, which includes photons lost to reflection. The quantum efficiency as measured is often referred to as the external quantum efficiency and will be dependent on the optical properties of the sample (reflection and transmission) as well as the electrical properties. To investigate purely the electrical properties of the sample it is useful to consider the internal quantum efficiency (IQE). In most solar cells the material is optically thick enough that photons lost to transmission can be neglected and the IQE is given by:

$$IQE(\lambda) = \frac{EQE(\lambda)}{1 - R(\lambda)} \tag{2.39}$$

Where R is the reflectance of the sample. This quantity itself can be modeled by considering the transport properties of minority carriers within the device.

The IQE of a cell can be calculated by making use of Eq. (2.32), Eq. (2.33) and Eq. (2.34). $I(\lambda)$ is calculated by summing the current generated in the depletion, emitter and base regions. If the depletion width and absorption coefficient of the device is known, the measured IQE can be modeled by using estimates for the minority carrier diffusion lengths L and interface recombination velocities s in the emitter and base regions. This allows the values of those parameters to be inferred from IQE measurement.

This model is used in Chapter 7 to investigate the contributions of different device regions to the photocurrent of GaAsSbN.

2.3.3 Current-voltage characteristic

This photo-generated current is not the only current component of the cell. Photocurrent is opposed by a 'dark' current with opposite sign that arises due to the radiative and non-radiative recombination of carriers. Photovoltaic cells are operated in forward bias (a positive bias applied to the p-type material and a negative bias applied to the n-type material) in order to extract power. This has the effect of reducing the built-in bias (equivalent to the separation of quasi-Fermi levels of the carrier populations) of the pn junction and allowing majority carrier diffusion and recombination, increasing the dark current exponentially with voltage. Each cell will therefore have a maximum power point at which the product of current (I) and voltage (V) output by the cell reaches a maximum, before a further increase in voltage causes the increased dark current to reduce the power output. IV curves provide a description of the electrical characteristics of the cell and enable the calculation of key parameters, including efficiency, short-circuit current, open-circuit voltage and fill factor.

Eq. (2.40) describes the IV curve with the ideal diode equation of a solar cell. This is a particular solution to the semiconductor transport equations for an abrupt junction with the depletion approximation.

$$I(V) = I_L - I_0(e^{(q\frac{(V+IR_S)}{nk_BT})} - 1) - \frac{V + IR_S}{R_{SH}} \tag{2.40}$$

Where I is the total device current, I_L is the photocurrent (often assumed to be equivalent to I_{SC} at all voltage points), I_0 is the recombination current, q is the charge on an electron, V is the bias across the cell, R_S is the series resistance, n is the diode ideality factor, k is Boltzmanns constant, T is temperature and R_{SH} is the shunt resistance. It should be noted that since I appears on both sides this is a transcendental equation and is often simulated numerically.

The equivalent circuit of the solar cell described by Eq. (2.40) is shown in Figure 2.6.

Eq. (2.40) shows that under short-circuit conditions (V=0), short-circuit current $I_{SC} = I_L$. The open-circuit voltage (where $I = 0$) can be expressed as:

$$V_{OC} = \frac{k_BT}{q} ln(\frac{I_{SC}}{I_0} + 1) \tag{2.41}$$

This result is important for concentrator applications since an increase in I_{SC} due to higher illumination intensity will also cause an increase in V_{OC} and hence an increase in power conversion efficiency. This allows the efficiency of a cell under concentration to exceed the Shockley-Queisser limit. The efficiency of light energy to electrical energy conversion is determined from the IV curve as described by Eq. (2.42).

$$\eta = \frac{J_mV_m}{P_{in}} = \frac{J_{SC}V_{OC}FF}{P_{in}} \tag{2.42}$$

Where η is power conversion efficiency, J_m is current density at maximum power, V_m is voltage at maximum power, P_{in} is the incident light power density, J_{SC} is the short-circuit current density and FF is the fill factor.

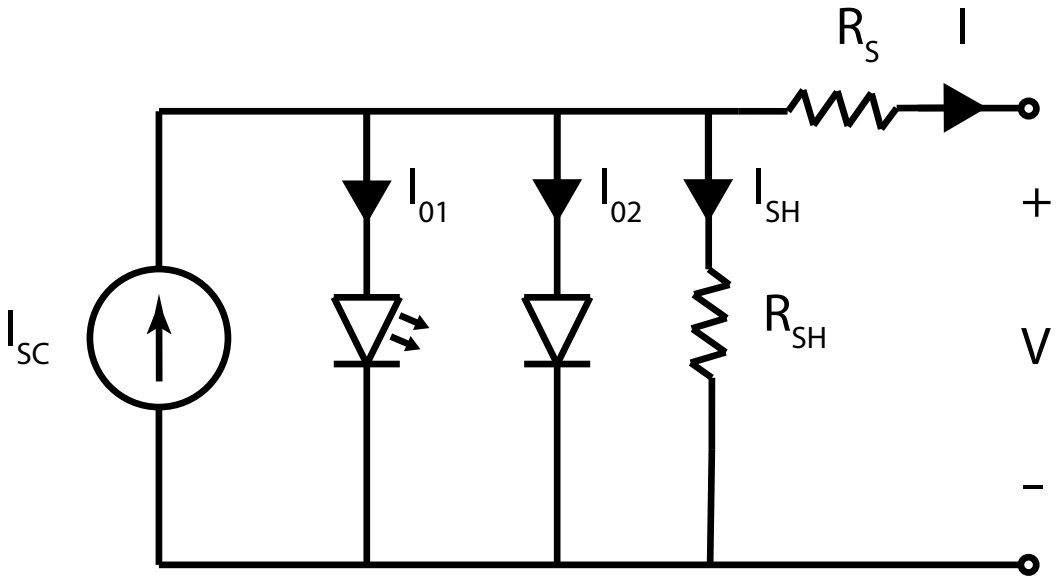


Figure 2.6: Equivalent circuit model of single junction solar cell. The solar cell acts as a current source with two recombination diodes. The series and shunt resistances of the sub-cell are also included. For a multi-junction model, several of these circuits are connected in series with a small series resistance loss due to the tunnel junction.

2.3.4 Current-voltage characteristic analysis

Eq. (2.40) and Figure 1.1 display the illuminated IV curve of a solar cell from which the key parameters, including efficiency, may be extracted. Different parameters may be extracted from dark IV (DIV) and light IV (LIV) measurements. The effects of recombination series resistance and shunt resistance may be observed. Recombination in the quasi-neutral regions (I_{01}) is assumed to occur with diode ideality factor $n = 1$ and recombination in the depletion region (I_{02}) is assumed to occur with diode ideality factor $n = 2$. These parameters can be identified from DIV measurements. I_{02} recombination

Table 2.1: Theoretical limits of multi-junction cells and achieved efficiency. The single junction values are for unconcentrated light (no record exists for single junction concentrator efficiency) whereas multi-junction efficiencies are under concentration.

Junctions	Theoretical efficiency [7] (%)	Achieved efficiency (Figure 1.3)(%)
1	31	29
2	55	34.1
3	63	44.4
4	68	46.0
Infinite	86.8	-

is mainly a function of depletion width and intrinsic carrier concentration whereas I_{01} recombination depends on factors such as diffusion length, carrier lifetimes and doping levels. Empirically, high quality solar cells have a V_{OC} of around 0.3 - 0.4 V less than their bandgap, but significant recombination through bulk or surface trap states may reduce this.

2.4 Multi-junction solar cell efficiency

Two notable analyses are available of the limits to multi-junction cells under concentration [39], [7]. An extension of the Shockley-Queisser limit to apply to terrestrial multi-junction CPV cells by Henry [39] describes how cell efficiency increases with number of junctions, with an infinite number of junctions partitioning infinitesimal slices of the solar spectrum approaching the thermodynamic limit to efficiency (the efficiency of a multi-junction is still lower than the thermodynamic limit due to radiative recombination losses).

The theoretical limits are reproduced in Table 2.1 and compared to achieved efficiency.

2.4.1 Optimal bandgaps

The efficiencies referred to in the section and table above are only achievable with the optimal combination of multiple bandgaps. This leads to an ideal set of bandgap energies for each multi-junction cell that is based on the optimisation of current and voltage for each sub-cell, comparable to the Shockley-Queisser limit formulation for single junction cells. This calculation is dependent on the type of spectrum, whether blackbody or tabulated data, as well as its intensity. Additionally, in practice, the desired combination of bandgaps may not be technologically achievable with III-V semiconductors and/or common substrates. Therefore it is important to optimise remaining free sub-cell energies with the given constraints of an application. This has been done to investigate the reported optimal 1 eV bandgap in Chapter 4.

2.4.2 Extrinsic loss mechanisms

From the observed discrepancy between intrinsic efficiency limits and achieved cell efficiency it is clear that theoretically avoidable extrinsic losses are reducing solar cell efficiency. There are several loss mechanisms present in multi-junction cells for CPV and these will be calculated in detail in Chapter 4. In this section they are summarised.

Series resistance is a major cause of efficiency loss at high concentration and may be seen through a reduction in fill factor (as well as I_{SC}) of the IV curve, becoming more pronounced with concentration level due to the I^2R nature of the loss. Sources of series resistance include the lateral spreading of current at the surface of the solar cell to metal grid fingers, tunnel junctions and material resistivity.

Shunt resistance results from pathways in the semiconductor material that provide a short-circuit between top and bottom contacts. A good solar cell should have high shunt resistance of the order of 10^6 Ω. Typically, shunt resistance effects do not cause a power loss under ideal operating conditions but can complicate cell measurements.

Shading loss due to the obscuration of the top surface of the solar cell by metal contacts is also present. However, the closer together the metal fingers are, the less series resistance loss due to sheet resistivity there is under high illumination conditions. This leads to a compromise with an optimal grid spacing for a given cell and concentration condition.

Reflection loss can be significant in terms of current-loss and is an important consideration in current-matching sub-cells. Appropriate anti-reflection coating design is essential.

2.4.3 Radiative coupling

Radiative coupling, also known as luminescent coupling, is an important effect in high material quality multi-junction cells and has recently been factored into cell design and simulation [[40] & references therein]. The phenomenon is based on the radiative recombination of carriers in one sub-cell being absorbed by a subsequent sub-cell. A schematic of this process is shown in Figure 2.7.

Photons emitted by upper sub-cells can be absorbed in lower sub-cells causing a downward transfer of current generation. Due to the transparency of the upper bandgap sub-cells to lower energy photons, this process does not work in the reverse direction. In addition, if a particular lower sub-cell is current limiting, other sub-cells will be driven to higher voltage to current-match. The higher voltage will produce greater recombination in the higher sub-cell and therefore greater transfer of photons to the (lower) sub-cells, helping to bring the limiting sub-cell closer to the current generation of the other sub-cells. This change in the current-balance between the sub-cells is illustrated in Figure 2.8 by considering the sub-cell IV curves with and without radiative coupling. The voltage dependency is also important with regard to operation under concentration, where the whole device operates at higher voltage and hence a higher proportional of recombination is radiative.

This effect can be included in simulations of MJSC IV curves by including an additional

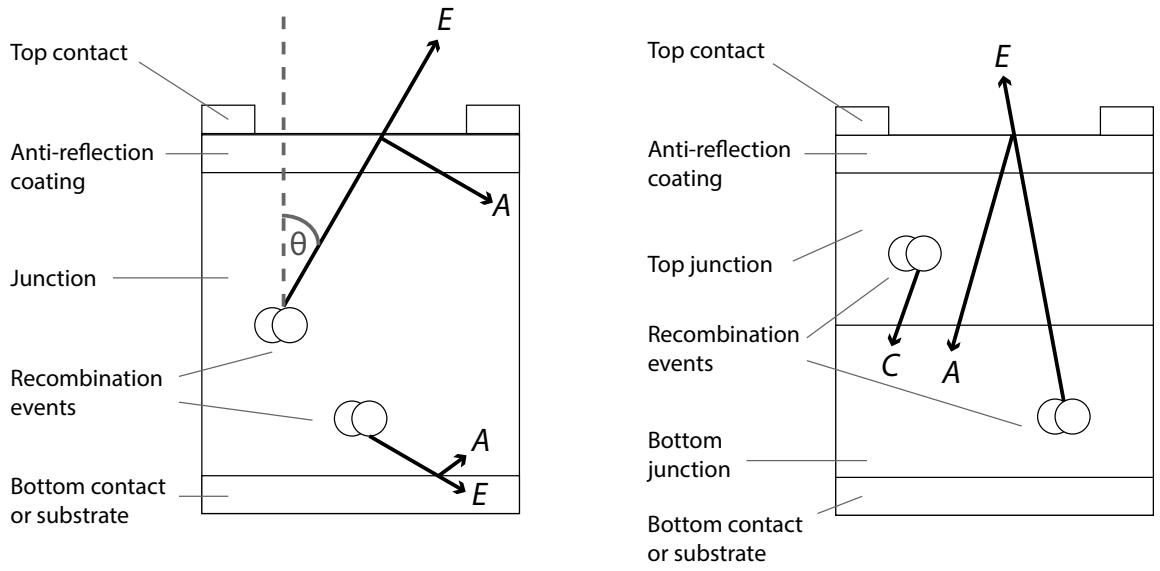


Figure 2.7: (Left): schematic of possible outcomes from radiative recombination in a single junction solar cell. Photons can escape to air, escape to substrate or reflect and be reabsorbed or 'recycled'. (Right): schematic showing how radiative coupling can arise from radiative recombination in multi-junction solar cells - photons emitted by the top cell are absorbed by the bottom cell. A indicates photon absorption, E indicates photon escape and C indicates coupling to the lower sub-cell.

current generation term for lower sub-cells:

$$J_{coupled,x} = F_c J_{01,x-1}(e^{\frac{qV_{x-1}}{k_B T}} - 1) \tag{2.43}$$

where F_c is the fraction of the radiative recombination from the sub-cell above that is transmitted to the cell below dependent on the geometry and optical environment of that sub-cell. The J_{01} exponential term is the current produced by a photon flux for the operating voltage and magnitude of radiative recombination in cell $x-1$, the cell above

the cell of interest x.

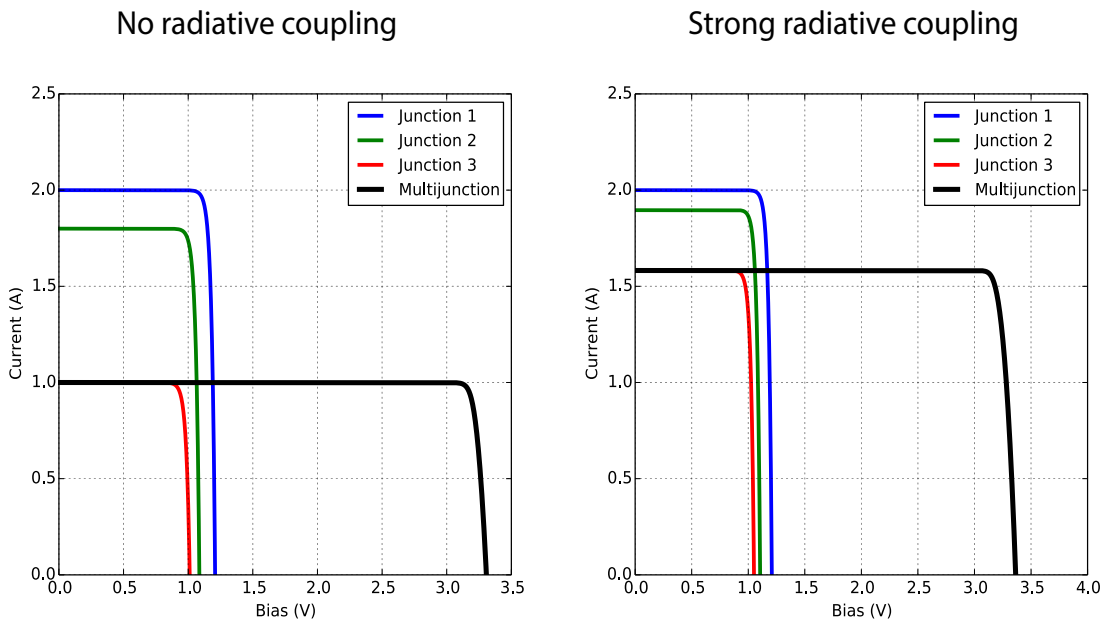


Figure 2.8: Simulated example of the beneficial effect of radiative coupling on the IV curve of a multi-junction solar cell. A current limiting lower sub-cell receives additional photocurrent from the radiative recombination of sub-cells above it. This raises the overall short-circuit current of the device and is compounded if more than one higher energy sub-cell has excessive current.

A number of authors have explored the concept of radiative coupling [41–43], applying the principle of detailed balance to the multi-junction solar cell and establishing limiting efficiencies for multijunction solar cells [44]. Brown and Green expanded on this idea in their detailed-balance treatment of a 2-junction MJSC [45] and pointed out that strong radiative coupling in a 2-junction MJSC can result in a cell that offers relatively high efficiency over a wide range of air-mass values. In the case of a blue rich incident solar spectrum (relative to the cell design), radiative coupling enables optical power to cascade down through sub-cells.

2.5 Dilute nitride alloys

Efficiency calculations that consider only radiative recombination show that replacing Ge with a more optimal 1 eV absorber could improve the triple-junction maximum efficiency by 4 percentage points under 1-sun AM1.5 illumination and that a quad-junction GaInP/GaAs/GaAsSbN/Ge cell could reach 50% efficiency under 2000 suns concentration. Due to the large bandgap reduction achieved when alloying GaAs with small concentrations of nitrogen, dilute nitride materials have been investigated for 1eV sub-cells for some time, notably GaInNAs [46] and GaInNAsSb [47]. These materials have exhibited poor minority carrier diffusion [48] and collection [49] properties and typically devices rely on wide depletion regions or undoped layers to produce current (at the expense of a reduced open-circuit voltage) [50]. GaAsSbN has been developed [51] as an alternative dilute nitride material that may be of interest due to enhanced nitrogen incorporation in comparison with GaInNAs [52], with the Sb acting as a surfactant during growth. Photodetectors [53] and solar cell prototypes made from GaAsSbN [54, 55] have been demonstrated.

Dilute nitride alloys of GaAs, the most basic being GaAsN, exhibit a number of properties different to those of other III-V semiconductor alloys found in MJSCs, such as GaInP and GaInAs. Furthermore, dilute quantities of nitrogen in GaAsN produce a material with different properties to N-rich GaN-like material. In particular, the introduction of N atoms to GaAs produces an anomalously large bandgap reduction combined with a smaller lattice constant, whereas the general trend for III-V compounds is an decrease in lattice constant with an increase in bandgap (see Figure 1.5). This effect is often most simply described using a band anti-crossing (BAC) model in which the N impurity splits the conduction band into a lower and an upper energy band.

Historically, the fabrication of dilute nitrogen alloys has proven to be challenging and device properties have also been found inappropriate for useful application in solar cells.

Early studies using metal-organic vapour chemical depositon (MOCVD) growth showed particularly poor properties for solar cells [46]. It is generally observed that electron transport degrades with the inclusion of nitrogen in the material. However, research on the dilute nitride alloy GaAsSbInN [47] led to the successful implementation of a 1 eV GaAsSbInN sub-cell in a one-time world record solar cell by the company Solar Junction [56]. This cell currently retains the record for efficiency for a monolithically grown, lattice-matched cell, making it interesting for manufacture. Despite offering the same advantages, compared to GaInNAs and GaInAsNSb, GaAsSbN is relatively less studied. However it may offer some interesting advantages over the In-containing compounds, such as enhanced nitrogen incorporation [52] and lack of In-related defects [54]. Considering that the Solar Junction record efficiency MJSC was developed using a thorough understanding of the interaction of material properties of GaAsSbInN with the overall multi-junction cell design, these aspects will be considered in this thesis.

2.5.1 Band anti-crossing

Band anti-crossing (BAC) is a band structure phenomenon specific to highly-mismatched alloy systems. Both GaAsN alloys and GaAsSb have been postulated to exhibit this effect in the conduction band [57] and valence band [58] respectively - GaAsSbN therefore exhibits band anti-crossing in both conduction and valence band.

The effect is caused by the introduction of dilute quantities of a fixed impurity level. This causes a splitting of the band - the conduction band in the case of the introduction of nitrogen - into two, with higher and lower energies than the original band. This is the origin of the anomalously large bandgap bowing effect in dilute nitride alloys. Figure 2.9 shows the effect with GaAsN with 2% N content calculated using the formalism developed in [57]. The two new energy bands are described as a function of the composition:

$$E_{\pm}(y) = \frac{1}{2}(E_N + E_C B \pm ((E_N - E_i)^2 + 4{C_N}^2 y)^{\frac{1}{2}}) \tag{2.44}$$

where y is the nitrogen fraction, E_i is the unperturbed band energy and E_N and C_N are constants for the impurity energy and interaction strength respectively.

A comparable but weaker effect is present in the valence band due to Sb. This splits both the light hole and heavy hole valence band (degenerate at the Γ point) into an additional two bands. As can be seen from Eq. (2.44), the BAC effect is increased with increasing N or Sb concentration.

Further information on the band structure of dilute nitrides has been provided by the use of k.p theory, with Lindsay et al. extending the conventional 8-band k.p model to a 10-band model for GaInNAs and showing compatibility with BAC [59].

2.5.2 Localised and excitonic recombination

Dilute quantities of an alloy constituent can lead to a disordered material. In disordered materials, fluctuations in band structure can cause fluctuations in potential and localise carriers as trapped excitons [60]. These can then recombine at different energy to the de-localised band-to-band recombination, producing separate effects that can be observed through several signature photoluminescence measurement features. It will be shown that GaAsSbN exhibits this property in Chapter 6. One particular consequence of localised states is observed by measuring the peak photoluminescence energy as a function of temperature. For a regular compound semiconductor the photoluminescence energy varies with the bandgap of the material - higher energy at lower temperature and lower energy at higher temperature. This is described by Varshni's empirical expression:

$$E_g(T) = E_g(0) - \frac{\alpha T^2}{T + \beta} \tag{2.45}$$

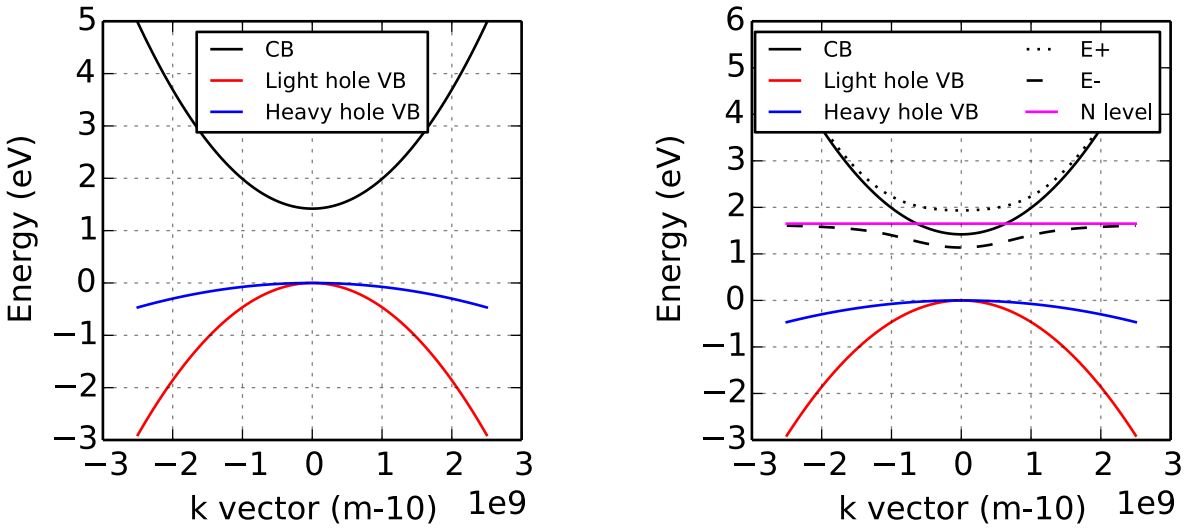


Figure 2.9: Illustration of the effect of 2% N impurity on simple parabolic band structure of gallium arsenide through band anti-crossing mechanism. (Left) shows the band structure of gallium arsenide at 300 K using the isotropic effective mass approximation with parabolic conduction and valence bands. The introduction of a fixed nitrogen impurity level at 1.7 eV above the valence band is illustrated (right). In the band anti-crossing model, the host conduction band is split into upper and lower energy bands, $E+$ and $E-$ respectively, the effect increasing with increasing N content. This leads to greater bandgap reduction with N composition than conventional alloying.

where $E_g(0)$ is the bandgap of the material at 0 K and α and β are material constants.

For a disordered semiconductor the bandgap does not vary so simply with temperature but exhibits an 's-shape' temperature dependence [61]. Starting from low temperature, the apparent bandgap as measured by photoluminescence first decreases with increasing temperature, then begins to increase, then starts decreasing again. This behaviour is determined by the interaction of carriers with localised states. At very low temperatures, carriers that are excited into a state remain frozen there. Therefore if there are lower energy states available due to fluctuations in potential, they are unable to reach them. As

the temperature increases and the carriers are given thermal energy they are able to 'hop' to local states of lower energy, giving an apparent reduction in bandgap below that of the expected bandgap of the material. As the carriers are given yet more thermal energy due to further increasing temperature, they escape the localisation potential, enter the delocalised band of states and the temperature behaviour of the bandgap follows Varshni's equation. Figure 2.10 is a schematic showing the three stages of this process.

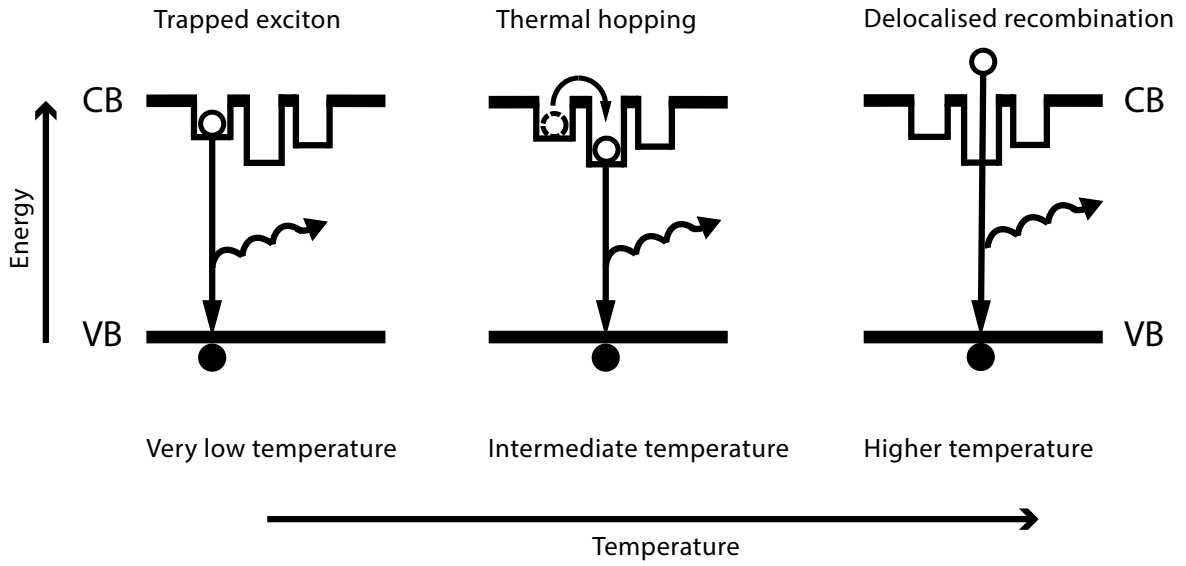


Figure 2.10: Schematic showing disordered conduction bands and the effect on localised recombination processes with changing temperature. This leads to a characteristic 's-shape' measurement of photoluminescence emission energy as a function of temperature.

Tsai et al. describe how sufficiently high level of p-type doping in GaInAsN leads to elimination of the effects of disorder-induced localised exciton recombination at low temperature, with recombination occurring through free excitons [62]. They explain this using a model whereby N-related traps are present near the conduction band. p-type

doping depletes these traps of electrons and holes are unable to recombine through them, preferring instead to recombine in a delocalised band-to-band mechanism.

Chapter 3

Experimental methods

The samples and devices studied in this thesis were largely designed by the author but grown by collaborators. The experimental characterisation was done by the author unless otherwise noted. As well as the growth method, optical and electrical characterisation techniques are described. These include electroreflectance and photoluminescence spectroscopy, quantum efficiency measurements, illuminated and dark current-voltage measurements and capacitance-voltage measurements.

3.1 Molecular beam epitaxy

Molecular beam epitaxy is a common technique for fabrication of semiconductor thin films and heterostructures. The samples in this study were grown by molecular beam epitaxy (MBE) at Nanyang Technological University, Singapore by the group of Professor Yoon Soon Fatt. A schematic of the machine is shown in Figure 3.1. GaAsSbN material was grown using MBE in conjunction with a radio frequency plasma-assisted nitrogen source and a valved antimony cracker source. The GaAsSbN layers were grown at RF plasma power of 420 W at a substrate temperature of 500 °C. The beam equivalent pressure of the Sb flux was 1.4×10^7 Torr. The As/Ga beam equivalent pressure ratio

was 8. Under these conditions, nominal concentrations of 1.8% nitrogen and 8.5% Sb were incorporated into the GaAsSbN layer. The concentrations of N and Sb in the material were determined using X-ray diffraction analysis based on the separate analysis of GaAsN and GaAsSb layers. Consistently throughout all samples in this thesis, Si was used as n-type dopant and Be was used as p-type dopant. The dopant sources were calibrated by taking into account the unintentional p-type background doping level of the GaAsSbN layer grown under these conditions. In-situ post-growth annealing was performed on all samples. Part of this process involved the deposition of a 50 nm $Al_{0.7}Ga_{0.3}As$ layer on top of every sample. The devices were fabricated using standard lithography and wet etch processing, with anti-reflection coating applied. Detailed information about the growth method has been published previously [63]. Further information on the development of a dilute nitride-specific MBE process can be found in [47].

3.2 Transmission and reflection spectroscopy

The absorption coefficient of a semiconductor material may be measured using transmission and reflection spectroscopy. This technique is particularly effective at lower values of absorption close to the bandgap, where transmission is greater. The transmission and reflection of light at a planar interface between two media are linked to the refractive indices of the media by Fresnel's equations for field reflection and transmission coefficients.

A simple relation between these two properties is based on the conservation of photons:

$$A(E) = 1 - R(E) - T(E) \tag{3.1}$$

With $A(E)$ defined as the ratio of absorbed light to incident light as a function of photon energy, $R(E)$ the ratio of reflected light to incident light as a function of photon energy and $T(E)$ the ratio of transmitted light to incident light as a function of photon

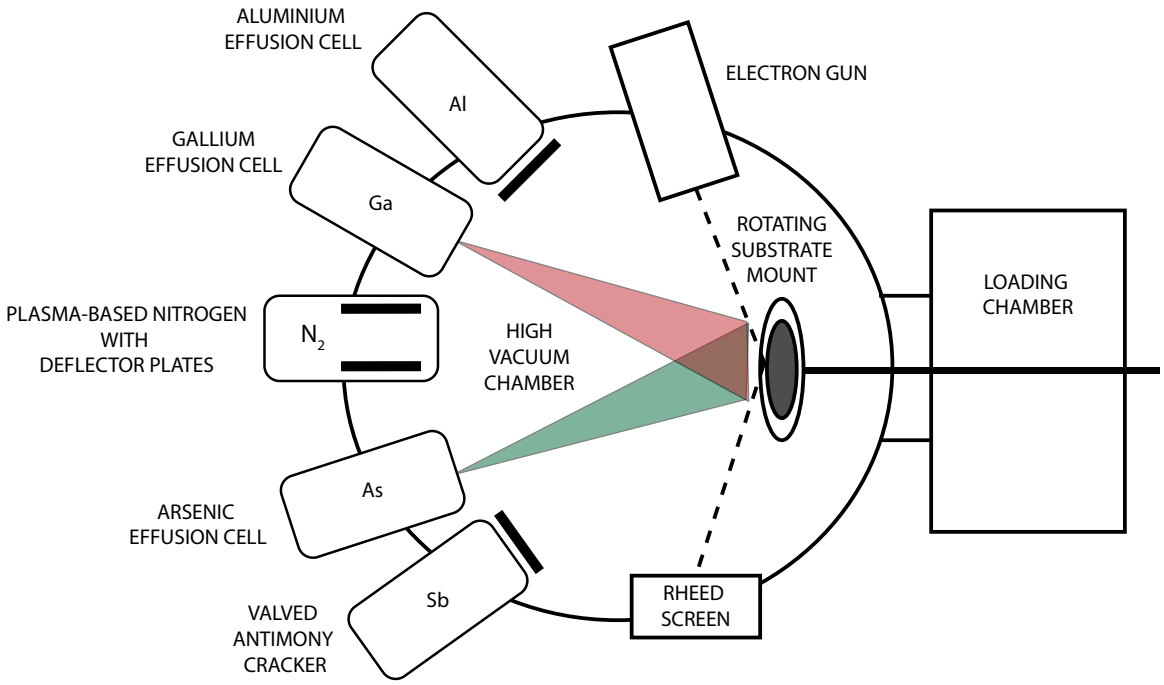


Figure 3.1: Schematic of MBE process. Elemental sources are used except in the case of nitrogen. The nitrogen source is fitted with deflector plates. Atoms are incident on the substrate which rotates to provide even growth. The walls of the chamber are cooled to prevent excess material from re-circulating. Growth speed and composition can be controlled by changing the species flux. Reflection high-energy electron diffraction (RHEED) is used to determine the surface properties.

energy. $A(E)$ may be related to the absorption coefficient of the material through the Beer-Lambert law:

$$A(E) = \exp(-\alpha(E)t) \tag{3.2}$$

where $\alpha(E)$ is the absorption coefficient of the material and t is the thickness of material.

In a sample with several interfaces or composed of multiple semiconductor materials further considerations are required. The lack of doping in the GaAs substrate limits free carrier absorption and produces high transparency below the GaAs bandgap. The energy

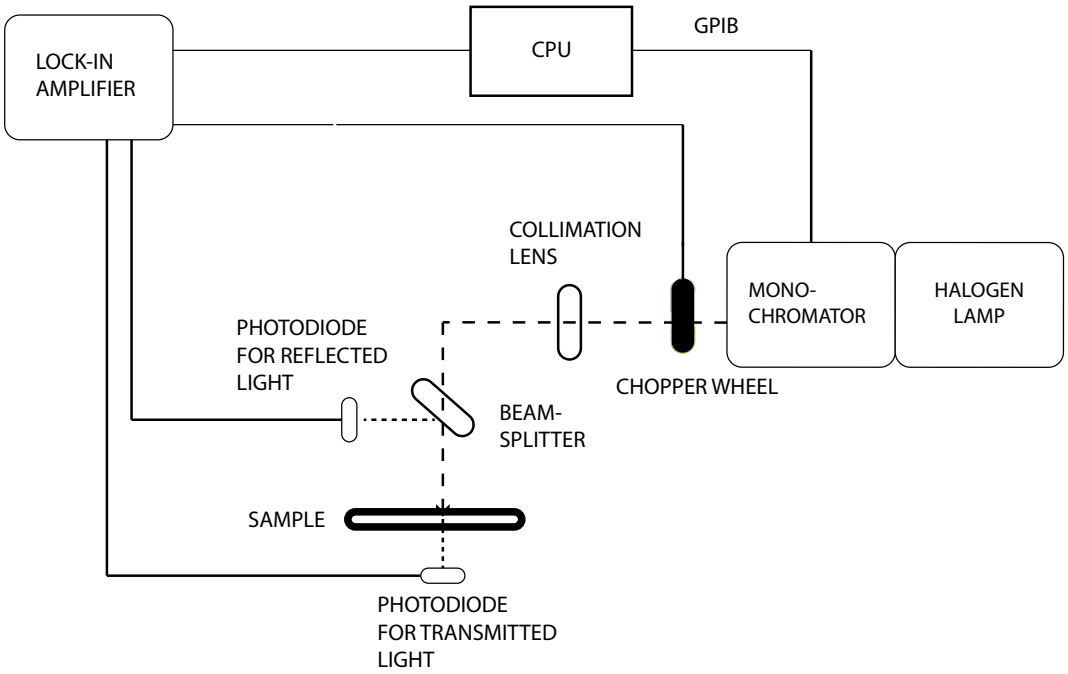


Figure 3.2: Transmission and reflection set-up used in this thesis. Chopped, monochrome light is incident on a sample. The reflected light and transmitted light is collected and detected by an appropriately placed calibrated photodiode.

range over which the absorption coefficient of GaAsSbN may be determined through measurement of transmission and reflection is limited to an upper value of 1.42 eV due to absorption of the GaAs substrate. Below 1.42 eV, the GaAs substrate is transparent and so any absorption in the sample is due to GaAsSbN. There is also the issue of multiple passes occuring through reflections within the sample or at the rear interface. It is assumed that the refractive index difference between GaAs and GaAsSbN is relatively small compared to the difference between a III-V compound and air - air is assumed to have $n = 1$ whereas III-V compounds typically have refractive indices on the order of 3.6. Therefore, of the reflections shown in Figure 3.3, those at the semiconductor/substrate interface are discounted.

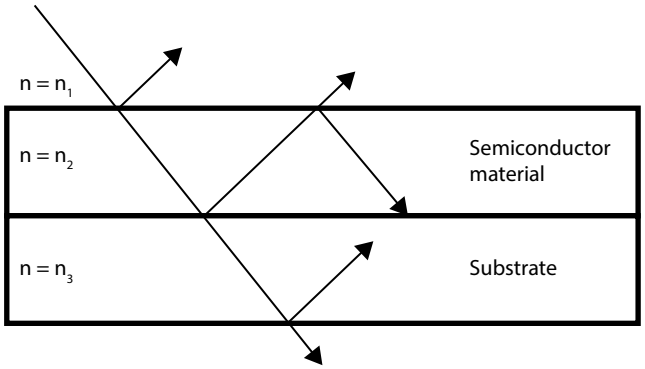


Figure 3.3: Illustration showing how multiple reflections can occur within the sample or at the rear interface, leading to multiple passes through the sample by photons. At each interface with a refractive index difference, transmission or reflection can occur (dependent also on incident photon energy and angle of incidence).

An equation for determination of absorption coefficient can then be written [64]:

$$\alpha(E) = \frac{1}{t} ln([\{(1-R)^4 + 4T^2R^2\}^{\frac{1}{2}} - (1-R)^2]/2TR^2) \tag{3.3}$$

The measurement of reflection and transmission of the sample was undertaken using a chopped monochromated light source with lock-in amplifier detection. Reflectance was measured with reference to a previously calibrated silver mirror. Two calibrated photodiodes, of Si and Ge material, were used to measure absolute reflected/transmitted light intensity at different wavelengths of interest. Reflection and transmission were measured at normal incidence with unpolarised light.

3.3 Electroreflectance

Electroreflectance is a type of modulated reflectance spectroscopy. These techniques periodically modulate the electric field within a sample, through directly applied voltage in the case of electroreflectance. Reflection of light from a sample is dependent upon its refractive index and hence dielectric function. This in turn is related to the band

structure of the material. In reflectance or absorption spectra the interband transitons are present as broad, inter-mixed features. However, by making appropriate use of modulation of electric field across the sample, the third derivative of the dielectric function can be directly observed [65]. An example of the form of data obtainable is shown in Fig. 1 and Fig. 5 of [65]. Modulation spectroscopy therefore provides sharper resolution of features at the energies of interband transitions, removing the broader background. In addition, the types of critical point can be determined. This can be used in models of the complex refractive index of the material. In this thesis absorption models for GaAsSbN derived from electroreflectance measurements are compared with the absorption coefficient directly measured using reflection and transmission spectroscopy.

An electroreflectance experimental set-up was assembled and is illustrated in Figure 3.4. A halogen lamp and Bentham TMc300 30 cm Czerny-Turner monochromator were used to provide incident illumination, which was reflected from the device and focused onto either a silicon or germanium calibrated photodiode (depending on wavelength range of interest). A modulated voltage was applied to the sample using a waveform generator. Detection of either the reflectance or the change in reflectance due to the modulation can be performed using a lock-in amplifier synchronised with either an optical chopper or the frequency of voltage modulation, depending on the desired measurement.

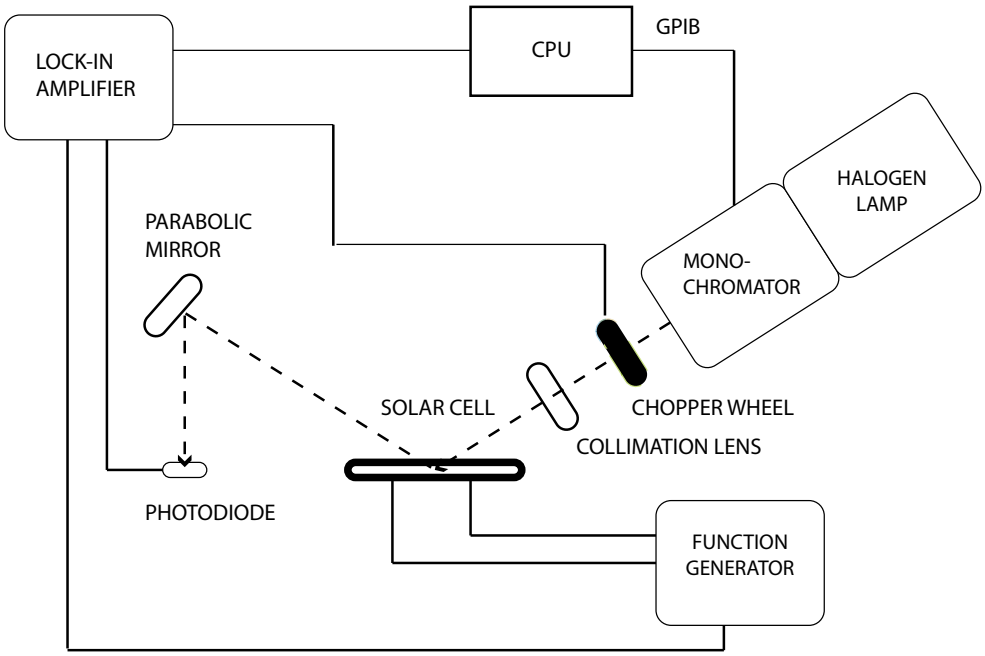


Figure 3.4: Electroreflectance set-up used in this thesis. Chopped, monochrome light is incident on a solar cell device with electrical contacts. The reflected light is collected and detected by a calibrated photodiode. A function generator can be used to apply alternating voltage to the device with the frequency synchronised to the lock-in amplifier for detection of the modulated reflectance.

3.4 Photoluminescence

Photoluminescence (PL) is the emission of photons subsequent to excitation of a sample, usually by laser source. The technique can provide information on electronic structure such as the band-gap of materials, defects and recombination mechanisms. In particular, time-resolved PL (TRPL) describes carrier dynamics and carrier lifetimes within a sample. To measure GaAsSbN, which exhibited short carrier lifetimes, a streak camera apparatus was utilised. This was performed during a visit to the University of Kobe.

3.4.1 Continuous wave

Steady state, wavelength resolved photoluminescence was obtained either with a 532 nm Millenia V continuous wave laser or with a tunable Ti:saph laser emitting at 900 nm. A 785 nm PicoQuant LDH pulsed diode laser operating at 80 MHz was also able to produce quasi-steady state photoluminescence. A Hamamatsu H10330B-45 near infrared photomultiplier tube detector was available with spectral response between 950 and 1400 nm. This was used with mechanical light modulation and a lock-in amplifier for continuous wave PL measurement. Wavelength resolution was provided by a 0.5 m focal length spectrometer.

3.4.2 Time-resolved

At the University of Kobe (the research group of Professor Takashi Kita), a tunable mode-locked Ti:sapphire laser was available along with a streak camera detector, allowing high resolution TRPL to be measured. The Ti:sapphire laser was mode-locked with pulse width of 140 fs. Laser repetition rate of either 1 MHz or 4 MHz and emission of 900 nm was achieved via an acousto-optic pulse picker, directly exciting the GaAsSbN. Incident average power of either 100 μW or 900 μW was used for various measurements, creating a low level of minority-carrier injection. The laser spot was 50 μm diameter. A Hamamatsu C11293-02 near-infrared streak camera with temporal resolution of 20 ps was used to detect PL resolved both spectrally and temporally. The spectral range was 1000 nm to 1650 nm. A cryostat was available for sample temperature control between 300 K and 3 K.

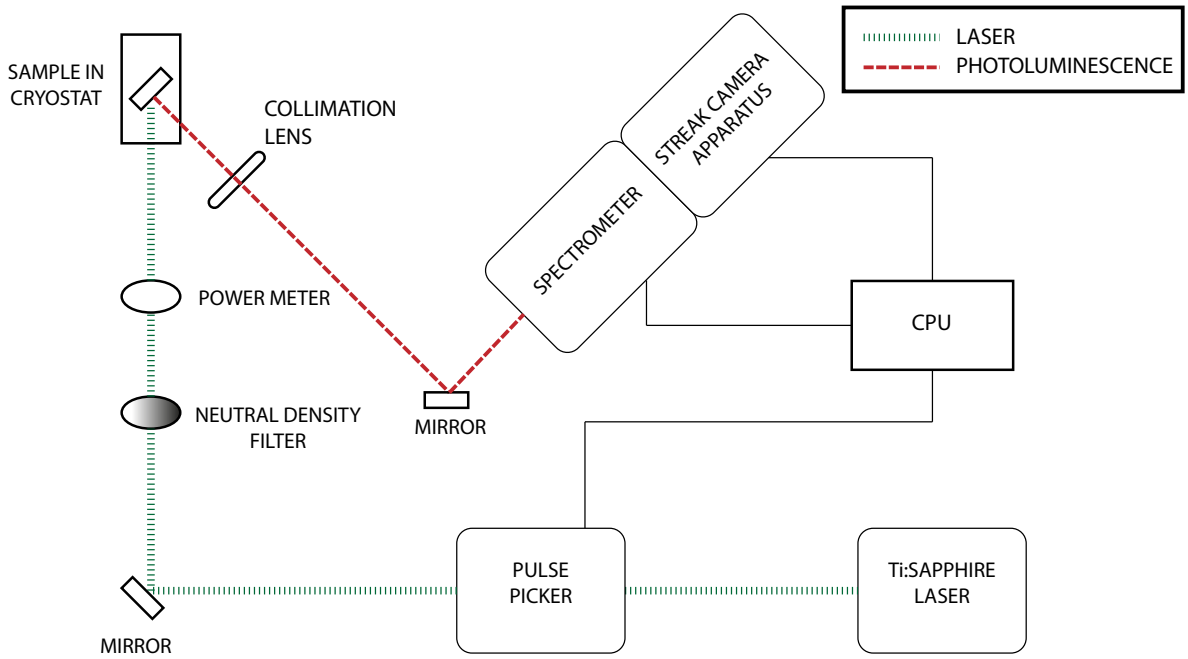


Figure 3.5: Schematic showing experimental set-up for time-resolved photoluminescence of GaAsSbN using streak camera detection.

3.5 Device electrical characterisation

3.5.1 Current-voltage characteristic

The current-voltage characteristic is a valuable measurement of solar cell electrical properties.

Semi-log plotting of dark IV and fitting to the double diode equation Eq. (2.40) can be used to calculate recombination currents and series and shunt resistance - although the dark IV current flows the opposite way to photogenerated current and therefore follows different current paths. For this reason DIV-calculated series resistance is usually lower than under illumination conditions.

Due to the nature of semiconductor growth, where many devices are grown on one

wafer, IV measurements will be used as a screening process. DIV was used to check the diode characteristics, with the best devices being selected for further characterisation.

Light IV (LIV) measurement provides the short-circuit current, open-circuit voltage and efficiency of a solar cell. When measuring any IV-curve under an illumination source, there will be errors in terms of the accurate measurement of the spectrum input power as well as spectral mismatch - the fill factor of different band-gap cells will be affected differently depending on the exact composition of the illumination. A GPIB-controlled Keithley 2400 source meter was available for measuring IV curves. Contact to the cell was made by a specially designed vacuum-controlled wafer chuck for the bottom contact and BeCu probe needles for the top contact. A class AAA TS Space Systems Unisim Compact solar simulator was used for illumination of the devices. This has two independently adjustable lamps providing different regions of the spectrum. A metal halide source and an incandescent source are combined with a filter system to produce the AM1.5 spectrum. The simulator was calibrated using a triple-junction GaInP/GaInAs/Ge cell, as well as three isotype cells of each junction, provided by the Fraunhofer Institute for Solar Energy Systems. A comparison of the measurement at Imperial College London with that of the Fraunhofer Institute is shown in Figure 3.6.

3.5.2 Capacitance-voltage characteristic

Capacitance-voltage (CV) measurements of a diode can be used to determine the junction properties, including depletion width and doping level. In the case of an intrinsic sample, this can include the unintentional background doping of the material. A Keysight E49990A impedance analyser was used to determine the CV characterstic of samples. A four terminal configuration was used to apply AC voltage to detect capacitance and sweep DC voltage.

Capacitance of a diode has two components: junction capacitance and diffusion capacitance. The depletion width of the junction and the doping level can be determined from

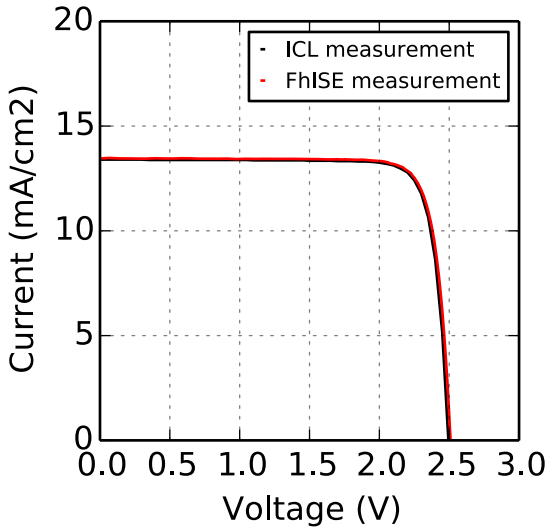


Figure 3.6: Experimental IV curve of a triple-junction solar cell used to calibrate the intensity of the two spectral zones of the AM1.5 solar simulator. Comparison is made between that measured at Imperial College London and that measured at the Fraunhofer Institute for Solar Energy under AM1.5 illumination.

the junction capacitance and so it is necessary to minimise the contribution of diffusion capacitance to the measured value. This can be done by observing the change in the CV curve with varied frequency of AC signal. The junction properties can be linked to capacitance using the following equations:

$$\frac{1}{C^2} = \frac{2}{q\epsilon_r\epsilon_0 A^2 N_c}(V_{bi} - \frac{2k_B T}{q} - V) \tag{3.4}$$

Where N_c equals:

$$N_c = \frac{N_A N_D}{N_A + N_D} \tag{3.5}$$

V_{bi} is the built-in voltage at the junction and A is the cross-sectional area of the junction. The depletion width can also be determined as:

$$W = \frac{\epsilon_r \epsilon_0 A}{C} \tag{3.6}$$

Another experimental consideration is to limit the forward DC bias to prevent large increase in the conductance of the cell.

3.5.3 Quantum efficiency

QE is the ratio of electrons extracted from the device to photons incident on a device, discussed in Section 2.3.2. The measurement consists of halogen/xenon light sources with power supplies. The light is monochromated with a Bentham TMc300 Czerny-Turner layout monochromator. Light is transmitted to a parabolic mirror, where it is focused onto the device under test, which is vacuum fixed to a wafer chuck with probe. In order to measure the response, a frequency generator and optical chopper are employed along with a lock-in amplifier. The photocurrent of the device induced by the alternating light source can then be measured. Finally, to convert the measured photocurrent to quantum efficiency, calibrated reference photodiodes of Si (350 to 780 nm) and Ge (780 to 1800 nm) are used to measure the incident photon flux. This set-up can be modified to measure reflectivity of samples as well as transmission. The set-up is shown in Figure 3.7.

QE response curves can reveal information about carrier transport, for example voltage dependence of the QE can indicate that there is poor diffusive transport of minority carriers within the device. The response at different wavelengths also represents the response at different penetration depth, with higher energy photons being absorbed nearer the top of the device. Minority carriers generated near the top and rear of the device can be more susceptible to interface recombination issues. Combined with modeling based on the semiconductor transport equations, this can be used to calculate the carrier diffusion lengths and surface recombination of a sample [38]. Importantly for a material such as a dilute nitride alloy that may be expected to exhibit short minority carrier diffusion lengths,

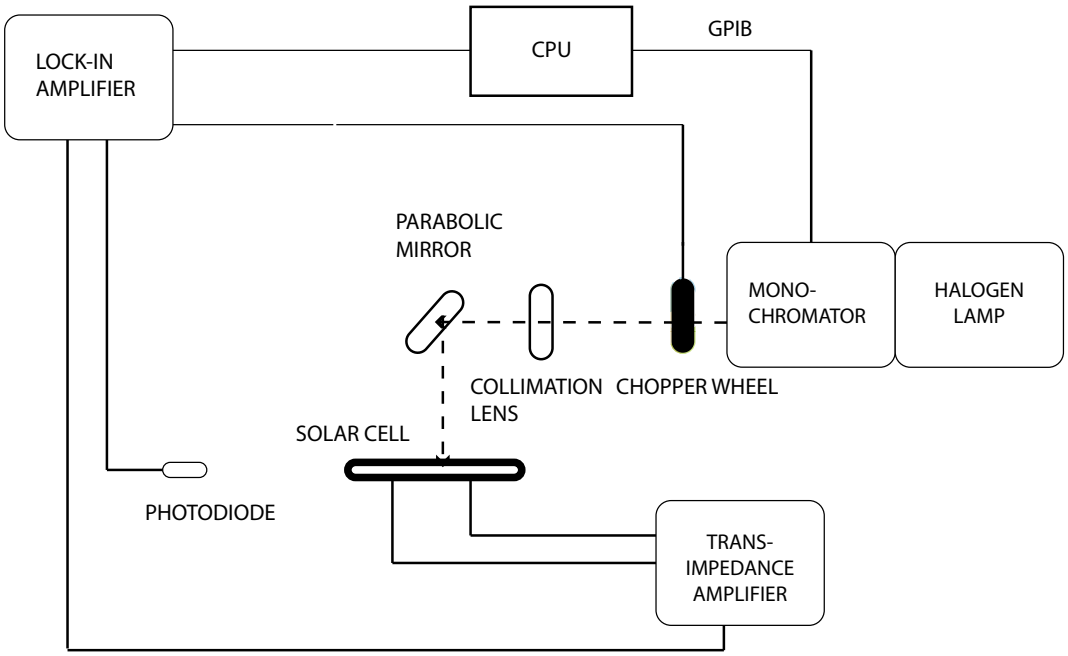


Figure 3.7: Schematic of experimental set-up to measure external quantum efficiency. To measure the photon flux, the calibrated photodiode is first placed in the position of the solar cell.

the IQE of a device can be used to determine the relative contributions of minority carrier drift current and diffusion current. This will be applied in Chapter 7.

Chapter 4

Multi-junction solar cell radiative coupling and series resistance

In this chapter the present loss mechanisms in current III-V compound semiconductor multi-junction structures are reviewed and the effects of separate mechanisms on device efficiency are isolated. This is first applied to determine the limits of the conventional triple-junction structure and then applied to four potential high efficiency lattice-matched architectures with 4-5 sub-cells. Although the value of 1 eV sub-cells is confirmed, a quad-junction concept utilizing a 1.15 eV junction is proposed. This has the potential to reach 50% efficiency under concentration even with realistic extrinsic losses.

This chapter also presents calculation of the practical limit of performance enhancement due to the radiative coupling effect for multi-junction solar cells (MJSCs) under a wide range of atmospheric conditions encountered in potential sites for CPV systems. It is shown that under high concentration, with very radiative material, even a 1.9/1.42/1.15/0.66 eV cell may be efficient. Radiative recombination is the only recombination process that is necessarily present in an otherwise optimal solar cell, and increasingly III-V solar cells are being grown with sufficiently high material quality that radiative recombination is the dominant recombination process. Radiative (or lumines-

cent) coupling occurs when photon emission takes place in a high band gap junction and is absorbed by a subsequent lower band gap junction. In a series connected solar cell this can result in an efficiency gain, if the lower-gap junction is limiting the current flowing through the entire multijunction device.

This chapter presents quantitative analysis of the power and energy yield enhancement that can be expected from radiative coupling in multi-junction solar cells of various designs under realistic spectral conditions in different locations with high CPV potential. The performance of cells with the likely variation in spectral irradiance due to variation in atmospheric aerosols and precipitable water is examined. MJSCs with both optimal and sub-optimal band gap combinations with respect to the AM1.5D spectrum were considered. The energy yield improvement over an annual period is calculated.

4.1 Simulation method for MJSC IV including radiative coupling

In this section the various terms of the multi-junction solar cell IV curve simulation method are described. An equivalent circuit for each sub-cell is shown in Figure 2.6.

4.1.1 Short-circuit current

The externally-induced short-circuit current for each sub-cell is calculated using the Beer-Lambert law by considering the absorption coefficient of the sub-cell, a typical anti-reflection coating (dual-layer MgF/ZnS) and a sub-cell thickness, optimised to provide the best current match for the whole structure. This is then integrated with the AM 1.5D solar spectrum under 1000X (suns) concentration. Some fraction of illumination is considered lost to shading by the front metal contact. In this simple model of current calculation based on the Beer-Lambert law, it is therefore implied that all minority carriers

reach the junction of the sub-cell. Short-circuit current is assumed to scale linearly with concentration.

4.1.2 Extrinsic losses

The following extrinsic solar cell losses are considered:

- Non-radiative recombination,
- Reflection loss due to imperfect (MgF/ZnS) ARC,
- Front contact shading,
- Series resistance.

The nonradiative $n = 2$ component of each sub-cell is estimated using a radiative efficiency method [66], with each sub-cell being assumed to be state-of-the-art material. This method considers radiative efficiency as a parameter for material quality, defined as:

$$\eta(V) = \frac{J_{01}e^{(q\frac{V}{k_BT})} - 1)}{J_{01}(e^{(q\frac{V}{k_BT})} - 1) + J_{02}(e^{(q\frac{V}{2k_BT})} - 1)} \tag{4.1}$$

Where J_{01} is assumed to be purely radiative and is determined itself from the multiplying the charge on an electron with the photon flux from the generalised Planck equation, proportional to the bandgap and absorptance of the cell. J_{02} can then be determined by using the radiative efficiency of the cell, which can itself be determined by fitting the IV curve. High quality GaInP and GaAs sub-cells were found to have radiative efficiency of around 0.4. This method is less applicable to Ge as an indirect semiconductor and so radiative efficiency of 0.01 was used for this sub-cell to obtain a realistic open-circuit voltage. In the following work all sub-cells were simulated with radiative efficiency of 0.4 except for those assumed to be germanium.

Table 4.1: Series resistance values for different components of MJSC

Component	Series resistance (Ω)	Reference
2% shading grid	0.119	[16]
5% shading grid	0.023	[16]
5% shading 'developed' grid	0.009	[16]
Tunnel junction 1	0.0012	[16]
Tunnel junction 2	0.0008	[16]
Whole device (0.16 cm^2)	0.128	[68]

Under the 1000X concentration considered here, non-radiative recombination becomes a less significant loss mechanism than at one sun concentration.

The front contact shading and series resistance are often intrinsically linked by the design of the front contact metalisation [67]. Although there are other components to the series resistance of a solar cell, such as tunnel diodes, under normal concentrated operation they are less significant than the contribution of the lateral resistance between grid fingers of the front contact. This is detailed in Table 4.1. There is therefore an optimum grid finger spacing for a given illumination concentration that gives sufficient metal coverage to lower voltage loss due to series resistance without over-obscuring the device and limiting short-circuit current.

The effects of varying both shading and series resistance independently are first investigated in Section 4.2 below to show that there are limits to efficiency from these losses even if both could be minimised simultaneously. In further calculations, the values are fixed at 12.5 Ω cm^2 with 5% shading, typical for current technology.

4.2 Limits to triple-junction cell from series resistance and shading

This section presents the simulation of LIV characteristics of solar cells considering the extrinsic losses of series resistance and shading. ARC is not included in this section and EQE is considered a constant 92% across sub-cells. Figure 4.1 shows the change in efficiency with concentration and the effect of series resistance and shading for a triple-junction 1.90/1.42/1.03 eV cell. Changing the shading fraction results in a linear shift of the profile along the y axis due to the change in short-circuit current. The series resistance value determines the concentration at which peak efficiency occurs. It can be seen in the figure that if higher concentrations can be reached due to lower series resistance, higher efficiencies will be reached.

Figure 4.2 shows the effect of changing these two parameters independently as a contour plot for the same triple-junction cell. With the front contact metalisation contributing the majority of series resistance in the cell as well as obscuring the active area, it is not currently possible to simultaneously reduce both parameters by a significant amount. Therefore, even with designs that optimise the trade off between cell coverage and series resistance loss, there is a limit of $< 50\%$ imposed on triple-junction solar cells under concentration. The maximum efficiency calculated for a triple-junction cell was 48% at 2000 suns concentration. Figure 4.3 shows the same calculation for a 1.9/1.42/1.03/0.66 eV quad-junction cell. By comparison with Figure 4.2 it can be seen that for similar extrinsic losses, a quad-junction cell provides superior efficiency to a triple-junction cell and can even reach 50% at 1000 suns concentration. This is because the power loss due to series resistance is proportional to I^2R_s and the current of a quad-junction cell is lower than a triple-junction cell.

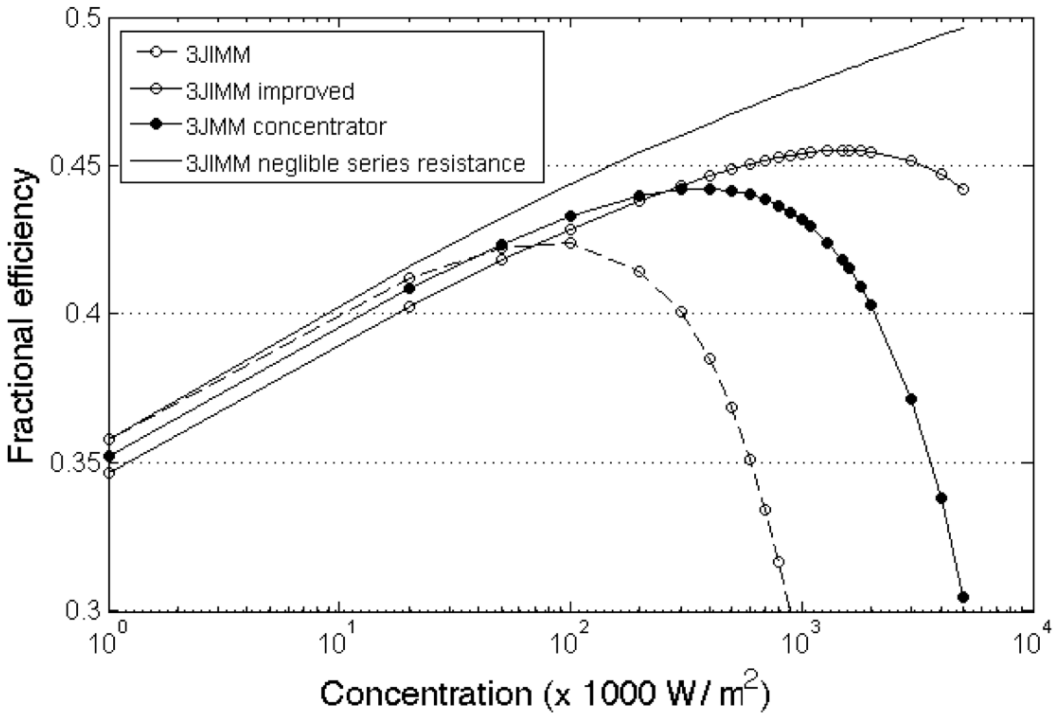


Figure 4.1: Calculation of several triple-junction solar cell efficiencies showing the importance of designing front grid adequately for series resistance and the limit to efficiency imposed by series resistance. The bottom cells here are 1 eV: '3JIMM' refers to Takamoto et al.'s one-sun world record cell [23]. '3JIMM concentrator' refers to Yoshida et al.'s concentration optimised front grid cell [68]. '3JIMM improved' describes an upper limit of practical improvements from reduction of series resistance ($R_s = 9.133 \times 10^{-3}\ \Omega$).

4.3 Effect of radiative coupling on spectral sensitivity of multi-junctions

4.3.1 Radiative recombination model

The radiative recombination emitted from a given junction is derived from the Generalised Planck expression, Eq. (2.21). The absorptivity is dependent on the absorption coefficient,

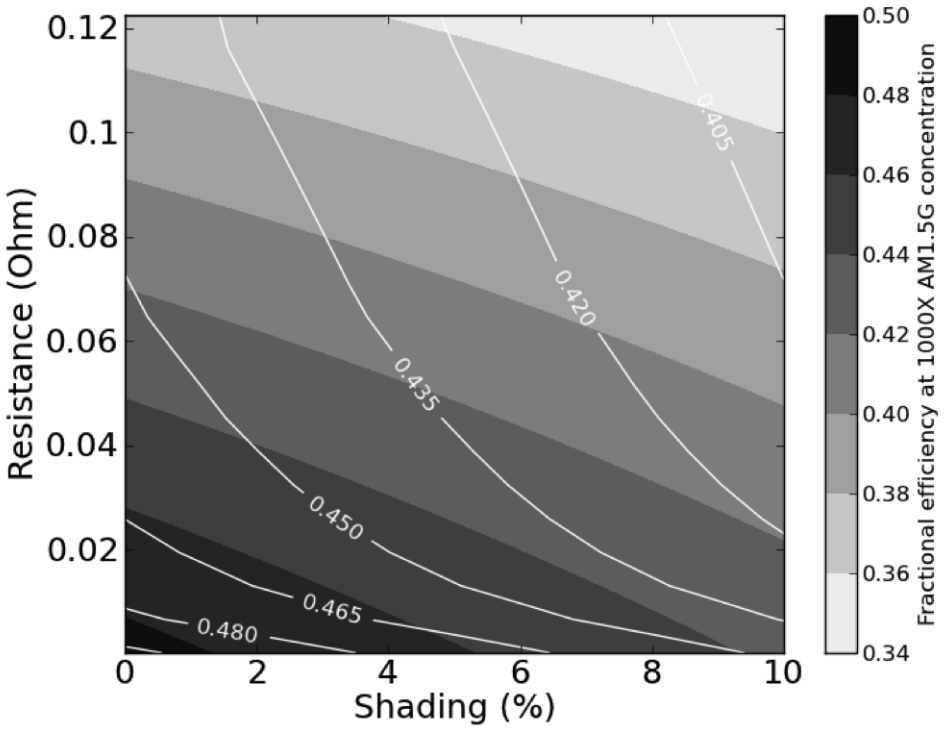


Figure 4.2: Calculation of 1.90/1.42/1.03 eV triple-junction solar cell efficiency at 1000 suns as a function of both series resistance and shading. Shaded contours represent efficiency at 1000X concentration. White line contours represent peak efficiency (at any concentration).

thickness and anti-reflection coating chosen. This allows a more realistic efficiency prediction for the proposed quad- and quin-junction architectures. The full calculation of radiative coupling is given by Eq. (4.6) and illustrated in Figure 4.4.

Integrating Eq. (4.6) numerically yields the internal radiative recombination rate, with the chemical potential assumed to be equal to the applied bias. The junction absorptivity, and hence emission, has contributions proportional to the escape through the top and back of the cell [69], and is defined by cell thickness, absorption coefficient and top surface reflection coefficient. In the context of radiative coupling in a multijunction cell,

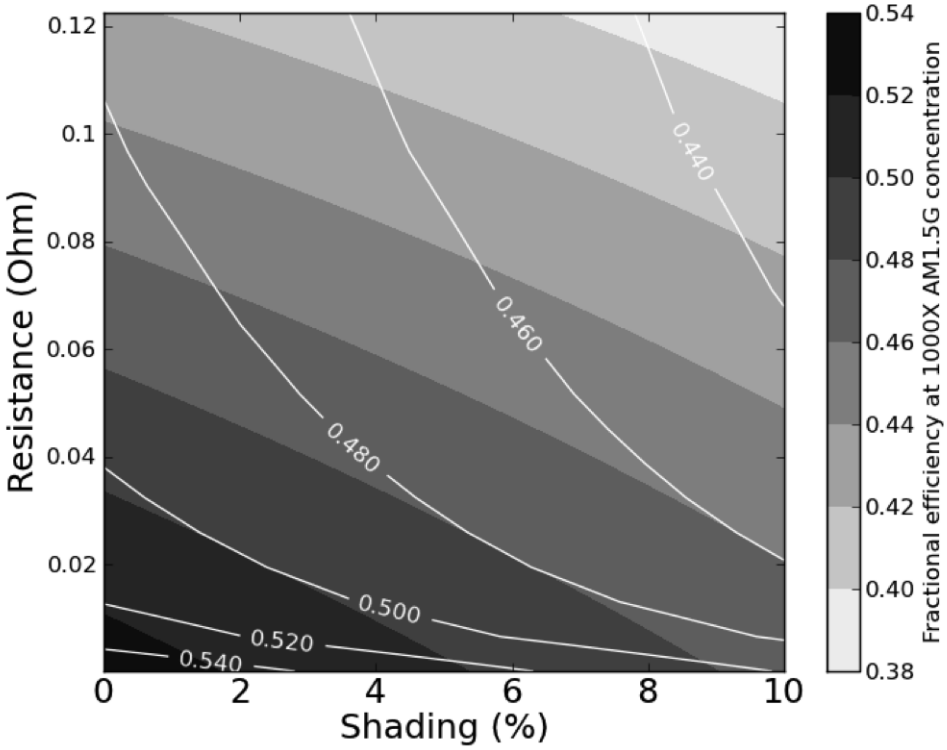


Figure 4.3: Calculation of 1.90/1.42/1.03/0.66 eV quad-junction solar cell efficiency at 1000 suns as a function of both series resistance and shading. Shaded contours are efficiency at 1000X concentration. White line contours represent peak efficiency (at any concentration). Even for similar levels of series resistance, a 4J cell is more efficient than a 3J cell and can reach efficiencies of 50%.

it is assumed that the downward radiative emission from the sub-cell is absorbed in the subsequent sub-cell to produce photocurrent in that sub-cell.

With radiative recombination current determined, non-radiative recombination current densities were calculated from the radiative efficiency method detailed in Section 4.1.2, assuming radiative efficiency of 40%, a figure achieved by lattice-matched junctions in state-of-the-art devices. The solar cell is simulated under 1000X concentration.

The equation below describes the current-voltage characteristic including radiative

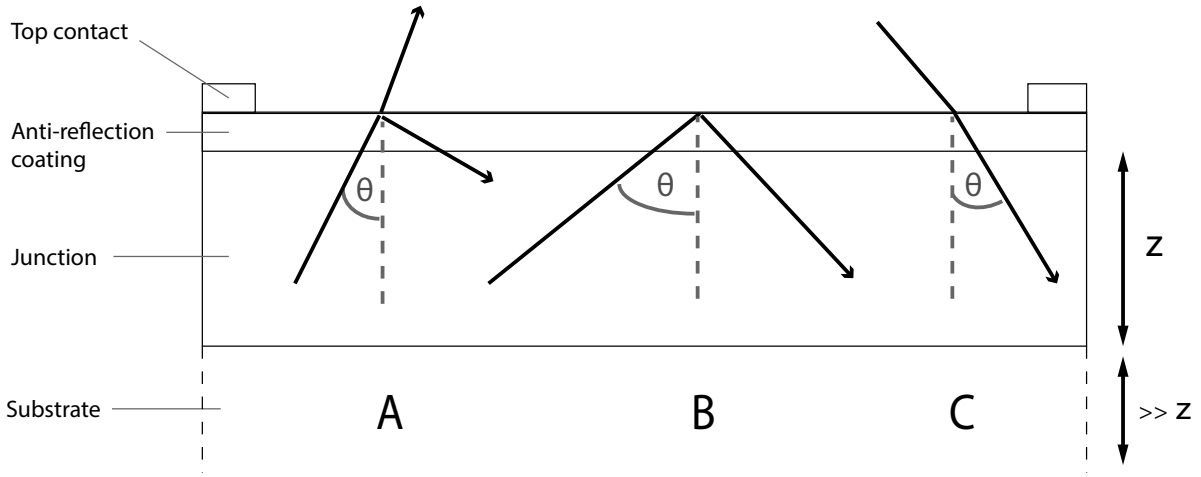


Figure 4.4: Schematic showing the three contributions of Eq. (4.6) to the absorptivity of a solar cell. The first term is represented by A, the second term by B and the third term by C. The top of the solar cell has an air interface and the rear interface is to the substrate. The air-semiconductor interface produces a small escape cone for radiative emission. Negligible refractive index difference is assumed between the solar cell and substrate, or between sub-cells, meaning most photons propagate downward.

coupling:

$$J_x(V) = J_{SC} - J_{01}(e^{q\frac{(V+IR_S)}{k_BT}} - 1) - J_{02}(e^{q\frac{(V+IR_S)}{2k_BT}} - 1) - \frac{V + IR_S}{R_{SH}} + J_{coupled,x} \qquad (4.2)$$

Where x is the junction of interest, $x-1$ is the junction above, J_{01} represents radiative recombination and J_{02} represents non-radiative recombination. $J_{coupled}$ is given by:

$$J_{coupled} = F_c J_{01,x-1}(e^{\frac{qV_{x-1}}{k_BT}} - 1) \qquad (4.3)$$

Where F_c is the fraction of the radiative recombination from the sub-cell above that is transmitted to the cell below dependent on the geometry and optical environment of

that sub-cell. The J_{01} exponential term is the current produced by a photon flux for the operating voltage and magnitude of radiative recombination in cell $x-1$, the cell above the cell of interest x.

This radiative proportion of the recombination current as well as the fraction that is transmitted downward can be estimated by considering the absorptivity (which, in turn, features in the generalised Planck equation for photon emission, Eq. (2.21)) of the sub-cell through the following equation [69]:

$$\int_S a(E,\theta)\cos(\theta)d\Omega \cdot \boldsymbol{dS} = 2\pi \int_{\cos\theta_c}^{1} [1-r(E,\theta)](1-e^{-\alpha z/\cos\theta})\cos\theta d(\cos\theta) \tag{4.4}$$

$$+ 2\pi \int_{\cos\theta_c}^{1} (1-r(E,\theta)e^{-\alpha z/\cos\theta})(1-e^{-\alpha z/\cos\theta}) \times \cos\theta d(\cos\theta) \tag{4.5}$$

$$+ 2\pi \int_{0}^{\cos\theta_c} (1-e^{2\alpha z/\cos\theta})\cos\theta d(\cos\theta) \tag{4.6}$$

Here, a is the absorptivity as a function of photon energy E and angle of incidence θ, Ω is the solid angle, S is the surface area, θ_c is the critical angle at the top interface as determined from Snells law, r is the reflectivity, α is the absorption coefficient of the sub-cell of interest and z is the thickness of the sub-cell.

The first integral term on the right hand side of the above equation describes emission out of the top of the sub-cell, whereas the second and third term describe emission that is directed downward. The equation is a simplified case neglecting edge emission from the device due to the much larger surface area of the top and bottom surface of the cell. Additionally, emission is assumed to be isotropic. In terms of the optical environment, it is assumed that the medium above the cell is air and that there is no change in refractive index below the sub-cell of interest. This allows for the calculation of F_c in Eq. (4.3) by taking the ratio of luminescence emitted 'upward'to 'downward' and it is found that >90% of emission is emitted downward due to the high contrast in refractive index at the top of the cell limiting the escape cone.

To model MJSC solar cell overall efficiency, Eq. (4.6) is used to calculate radiative recombination for each sub-cell, whereas the thickness, reflectance and absorption coefficient of the cell determine the current generation. The top of the solar cell has an air interface and the rear interface is to the substrate. The air-semiconductor interface produces a small escape cone for radiative emission. Negligible refractive index difference is assumed between the solar cell and substrate, meaning most photons propagate downward. Inclusion of an additional term for non-radiative recombination allows for realistic calculation of the IV curve of MJSCs.

4.3.2 Results

To illustrate the potential of radiative coupling, devices with sub-cells of different bandgaps and thicknesses are considered. Triple and quad-junction cells under AM1.5D spectral irradiance have optimal bandgaps of 1.74/1.18/0.69 eV and 1.92/1.42/1.04/0.69 eV, taking into account the ARC, are investigated. Since these cells are technologically difficult to manufacture, they are compared here with sub-optimal cells with bandgaps 1.88/1.41/0.66 eV and 1.88/1.41/1.00/0.66 eV. As sub-cell thickness plays an important role in the magnitude of the performance enhancement [40], thin (current-matched under AM1.5D) and thick sub-optimal bandgap cells were investigated in [12]. A thicker cell will have higher overall efficiency when radiative coupling is accounted for whereas a thinner cell will have higher efficiency when radiative coupling is not accounted for, and correspondingly the power enhancement is greater when using thicker sub-cells. This is shown in Figure 4.5. The 3J optimal cell considered here remains current matched even at large sub-cell thicknesses and so this comparison is not necessary. The 4J optimal cell enhancement shows slight sensitivity to the second junction thickness but not to the extent shown by sub-optimal cells, and so thick sub-cells are assumed for the optimal multi-junction devices.

Spectral irradiance is simulated under various atmospheric conditions using SMARTS 2.9.5 [70]. The expected power enhancement due to the atmospheric parameters of precip-

itable water, air mass and aerosols is calculated. The aerosol optical depth and Angström exponent, a parameter determining aerosol optical thickness that is inversely related to particle size, are considered. The expected power enhancement due to each atmospheric parameter is quantified by drawing the frequency distribution of parameter values at a particular location, using measurements from the Aerosol Robotic Network (AERONET) [71]. In addition, the expected enhancement in energy yield for three potential CPV deployment locations is examined for each MJSC design - Rogers Dry Lake (USA), Sede Boqer (Israel) and Jaipur (India).

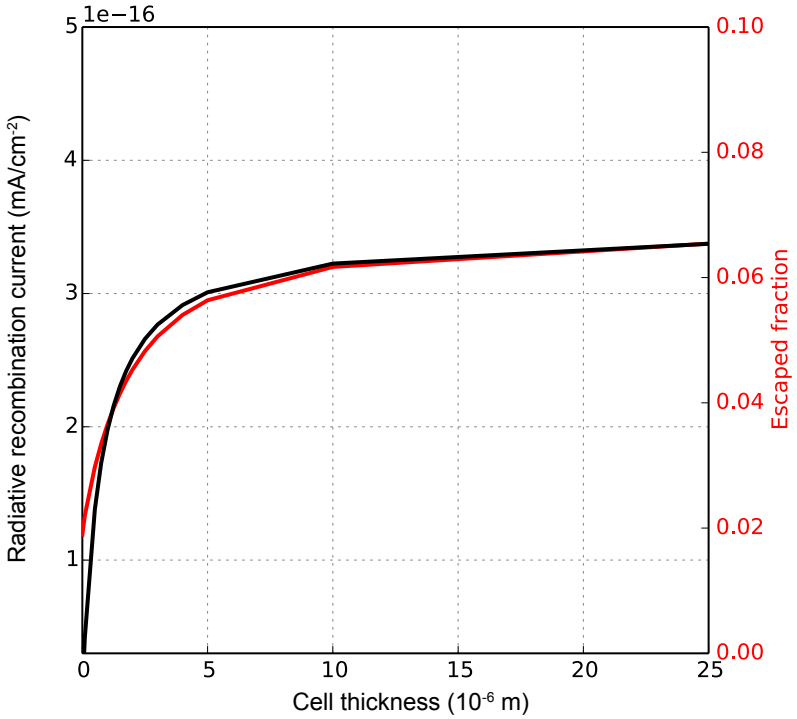


Figure 4.5: Radiative recombination current and escaped fraction from the top of the cell as a function of sub-cell thickness, assuming no non-radiative recombination. It can be seen that thinner cells allow less light to escape from the top surface, encouraging photon recycling. The recombination current itself is also lower.

Power Enhancement To quantify the potential power enhancement available from strong radiative coupling, an F_c value of 0% is compared with the maximum as calculated from the downward emission of the generalised Planck equation. The upper value, $> 90\%$, assumes that the cell is at the radiative limit and in practice will be lower due to non-radiative recombination. The percentage difference in estimated output power for these two values is then calculated from numerically solving the multi-junction current-voltage characteristics.

The enhancement in output power as a function of key atmospheric parameters — aerosol optical depth, air mass and precipitable water — has been calculated for four cell structures: 3J sub-optimal bandgaps 1.88/1.41/0.66 eV, 3J optimal bandgaps 1.74/1.18/0.69 eV, 4J sub-optimal bandgaps 1.88/1.41/1.00/0.66 eV, 4J optimal bandgaps 1.92/1.42/1.04/0.69 eV.

Air mass is defined as the optical path length of sunlight through the Earth's atmosphere. It is a ratio of the path length to the length vertically upwards. Air mass (AM) 1.5 is the standard condition for terrestrial solar cell charaterisation. Precipitable water is a measure of water content of the atmosphere - the depth of water contained in a column of the atmosphere if that water were precipitated. Water absorbs the infrared region of the solar spectrum. The aerosol optical depth is a measure of the extinction or scaterring of sunlight by particles in the atmosphere, the spectral dependence of which is given by the Angström exponent [5].

Unless otherwise stated, all other variables are set at the AM1.5D concentrator standard test condition reference values. Figure 4.6 shows the variation of enhancement with air mass and Figure 4.7 shows the variation of enhancement with precpitable water. The bar graph insets show the short circuit current for each junction in particular regimes, demonstrating that radiative coupling provides the greatest enhancement when higher band gap junctions possess the greatest short circuit current.

To determine realistic enhancement it is necessary to consider how likely it is that

these conditions prevail. Air mass values of less than 1 only occur at very high altitudes and there are relatively few instances of aerosols with low Angström exponent, associated with large particles.

To calculate the enhancement due to radiative coupling from each individual atmospheric parameter, the enhancement values are convolved with the normalised frequency distribution for each atmospheric parameter at each of the three locations identified. Optimal cell designs exhibit lower enhancement from radiative coupling than sub-optimal designs. Of the two optimal cells, the highest calculated value for radiative coupling enhancement is +3.33%, associated with precipitable water at Jaipur using the quad-junction device. The lowest enhancement is expected for aerosols at Jaipur, at 0.41%, with the optimal triple-junction MJSC. Across all devices, radiative coupling is less significant under Jaipur's red-rich irradiance conditions owing to the high Angström exponent of the aerosols present (see Figure 4.8 and Figure 4.9). This results in spectra that attenuate strongly at lower wavelengths, thus reducing the photogeneration in high band gap junctions.

MJSCs designed with optimal band gaps exhibit low enhancement from radiative coupling, typically <2%, since they are already well current matched under peak irradiance conditions. Similar calculations for the conventional thin sub-cell GaInP/GaInAs/Ge triple junction solar cell indicate performance gain of 1%, illustrating why radiative coupling effects have not been significant in presently deployed concentrator systems.

In the case of the sub-optimal 4J device the expected power enhancement is higher and is likely to be measurable under realistic conditions. This arises due to the significant differences in the short current current of each junction, in particular, elevated precipitable water dramatically reduces the photogeneration in the bottom two junctions, amplifying the radiative coupling effect. Across the parameters shown here (and Table 4.2), sub-optimal cell designs show greater enhancement from radiative coupling than optimal cell designs. This is largely due to the greater variation in sub-cell currents for the thick sub-

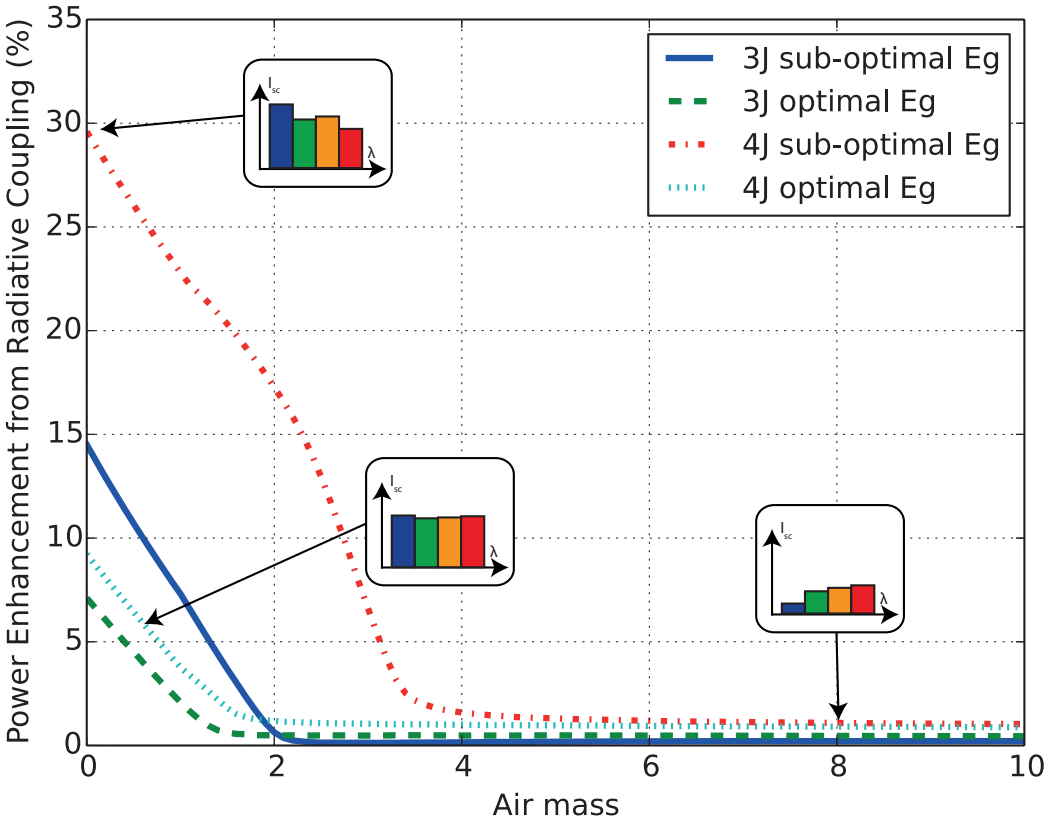


Figure 4.6: Power enhancement from radiative coupling as a function of air mass. Greater enhancement is noted at low air mass values, where shorter wavelengths receive proportionally more irradiance. Cell architectures are: 3J sub-optimal bandgaps 1.88/1.41/0.66 eV, 3J optimal 1.74/1.18/0.69 eV, 4J sub-optimal 1.88/1.41/1.00/0.66 eV, 4J optimal 1.92/1.42/1.04/0.69 eV.

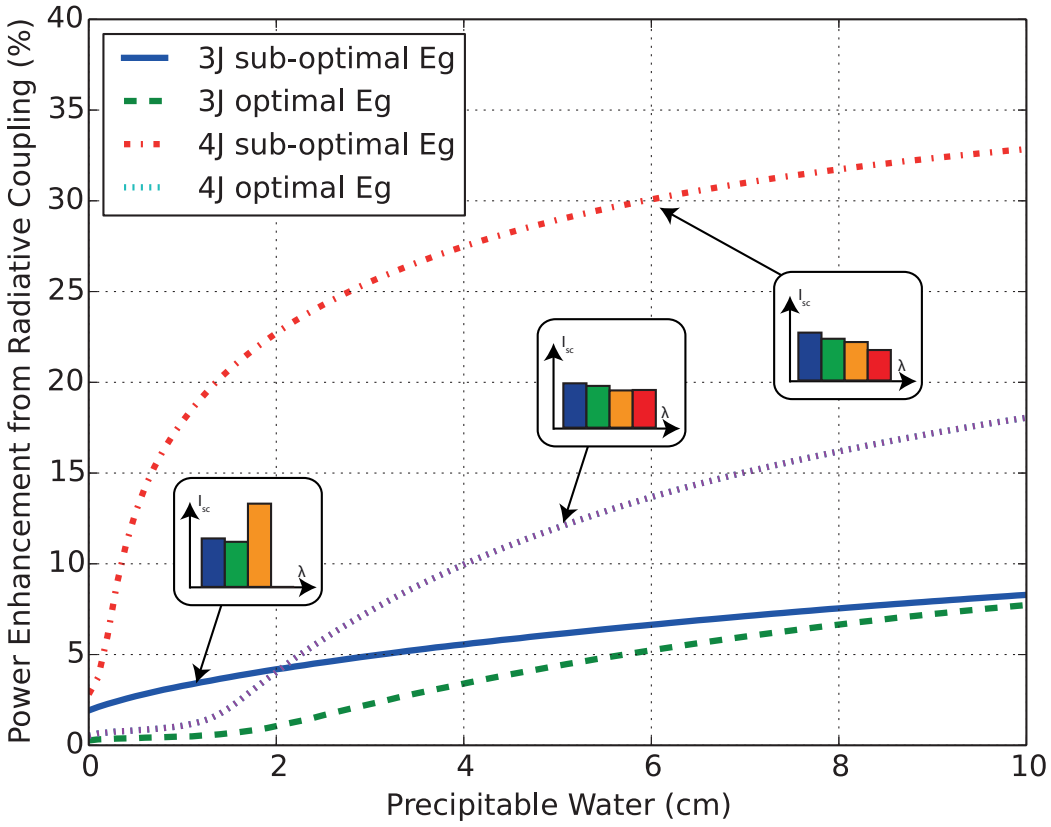


Figure 4.7: Power enhancement from radiative coupling as a function of precipitable water. Cell architectures are: 3J sub-optimal 1.88/1.41/0.66 eV, 3J optimal 1.74/1.18/0.69 eV, 4J sub-optimal 1.88/1.41/1.00/0.66 eV, 4J optimal 1.92/1.42/1.04/0.69 eV.

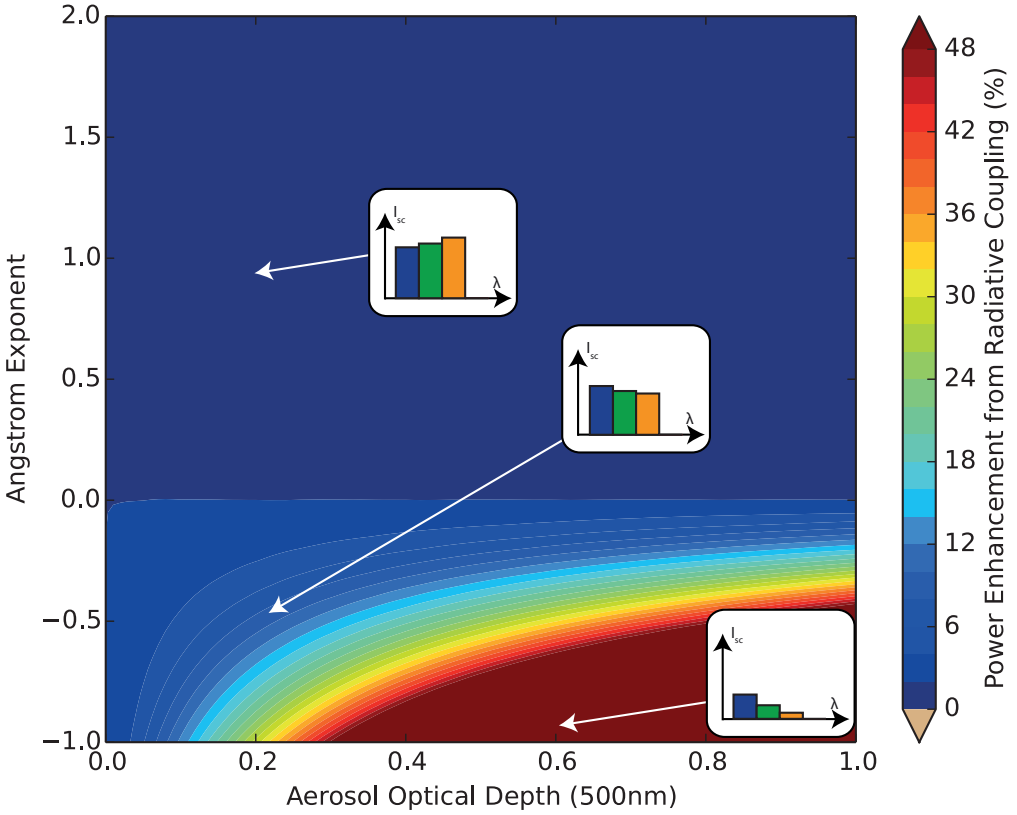


Figure 4.8: Power enhancement from radiative coupling, as a function of AOD and Angström Exponent for an optimized 1.74/1.18/0.69 eV bandgap triple-junction.

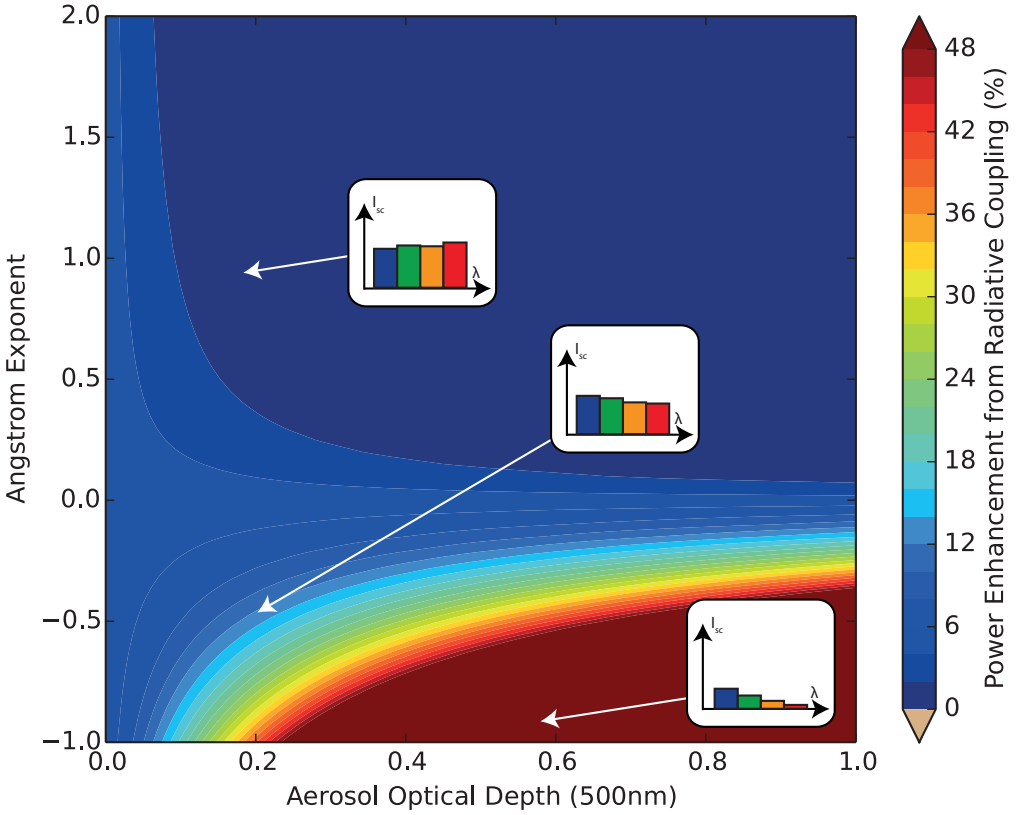


Figure 4.9: Power enhancement from radiative coupling, as a function of AOD and Angström Exponent for an optimised 1.92/1.42/1.04/0.69 eV bandgap quad-junction.

Table 4.2: Power enhancement by parameter in each location (%)

Location	Parameter (PW = precipitable water)	3J optimal	3J sub-optimal	4J optimal	4J sub-optimal
	Air mass	0.78	2.53	1.79	14.52
Rogers Dry Lake 2001	PW	0.52	3.23	1.33	17.07
	Aerosols	0.96	4.34	2.72	21.28
	Air mass	0.73	2.30	1.69	13.95
Sede Boqer 2006	PW	0.62	3.52	1.83	19.05
	Aerosols	0.68	3.27	1.86	17.96
	Air mass	0.67	1.94	1.55	13.03
Jaipur 2010	PW	1.08	3.84	3.33	20.24
	Aerosols	0.52	1.18	0.96	9.07

cell sub-optimal designs, which take advantage of radiative coupling. However if compared to the thinned, and therefore more current-matched, sub-optimal designs discussed in [12], the difference in enhancement between optimal and sub-optimal is of a more comparable level, as may be expected since both designs are better current matched under AM1.5D.

Annual Energy Yield Enhancement As there may be covariance between the relevant atmospheric parameters not captured by considering the parameters separately, time-resolved simulations with spectra from over the course of the year are used to predict enhancement to energy yield. The predicted energy yields for radiatively coupled (F_C maximum) and un-coupled ($F_C = 0\%$) cells are calculated and given in Table 4.3. The yield enhancement in percentage points is displayed graphically in Figure 4.10. For the locations examined, the distribution in air mass is similar due to their latitudes, and so the key differences lie in the how the aerosols and precipitable water affect the current-balance of each design.

The results show that although energy yield enhancement is on the same order of magnitude as the expected power enhancement. The consistently greater enhancement from the 4J sub-optimal structure is to be expected as there is substantial variation in short circuit currents under a wide range of conditions. Interestingly, the 4J sub-optimal

Table 4.3: Annual Energy Yield (kWh)

Location	F_C (coupling fraction)	3J optimal	3J sub-optimal	4J optimal	4J sub-optimal
Rogers Dry Lake 2001	Max	94.97	83.77	100.76	99.16
	0%	94.29	81.22	99.28	86.46
Sede Boqer 2006	Max	73.32	64.72	77.42	76.50
	0%	72.76	62.88	76.40	67.19
Jaipur 2010	Max	54.46	47.73	56.72	57.44
	0%	54.13	47.04	56.10	53.41

structure provides slightly greater yield than the 4J optimal device in Jaipur, and offers yields slightly below the optimal device in the other locations, highlighting the fact that radiative coupling can mitigate some of concerns over the spectral sensitivity of solar cells with four or more junctions.

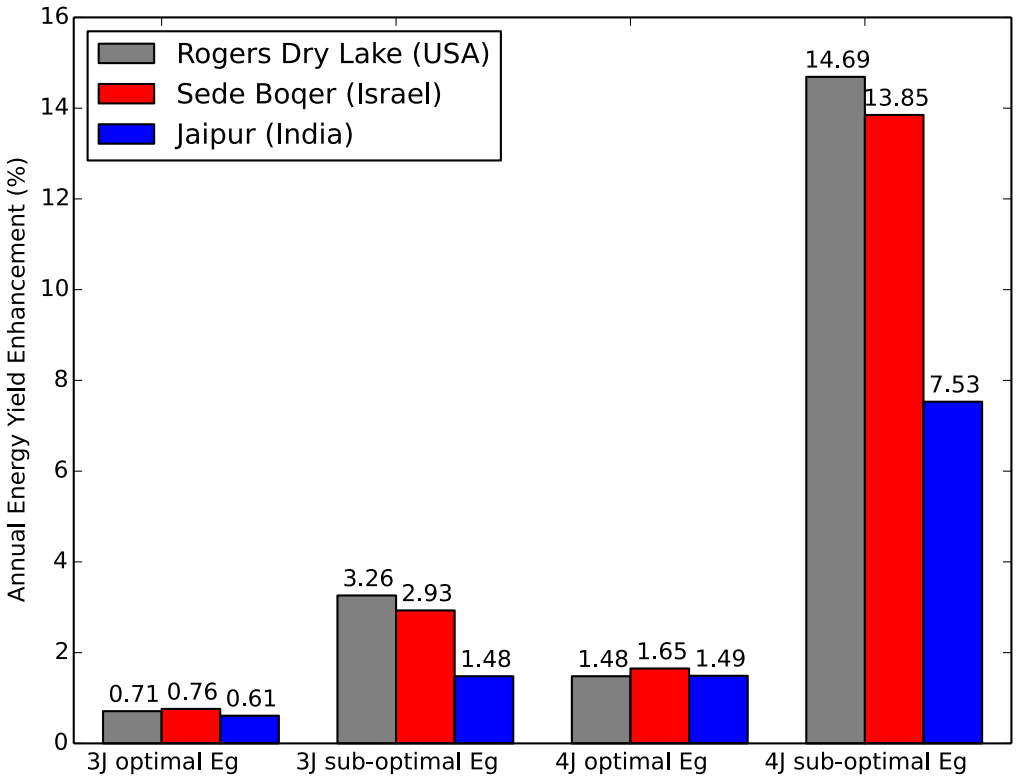


Figure 4.10: Energy yield enhancement from radiative coupling over annual periods for locations and cell designs identified. Cell architectures are: 3J sub-optimal bandgaps (E_g) 1.88/1.41/0.66 eV. 3J optimal 1.74/1.18/0.69 eV, 4J sub-optimal 1.88/1.41/1.00/0.66 eV, 4J optimal 1.92/1.42/1.04/0.69 eV.

4.4 Effect of radiative coupling on optimal bandgap

The method of calculating MJSC IV curves including radiative coupling was also applied to investigate optimal bandgap combinations. Table 4.4 shows the calculated efficiencies for the four architectures considered. All four are capable of reaching 50% at 1000 suns concentration provided losses are addressed and radiative coupling is present. The 1.02 eV sub-cell is assumed to be a dilute nitride material, which has been successfully used in triple-junctions but has yet to been demonstated in a high-performance quad-junction. The 1.15 eV sub-cell could enable two possible quad-junction architectures, shown in Figure 4.11 alongside the extrinsic losses for the device, as well as a quin-junction architecture.

Table 4.4: Potential efficiencies of different MJSC architectures incorporating a dilute nitride sub-cell.

Bandgaps (eV)	Efficiency (%)	Efficiency with max coupling (%)
1.90/1.40/1.02/0.66	48.9	50.4
1.97/1.49/1.15/0.66	51.2	51.8
1.90/1.42/1.15/0.66	49.7	50.7
2.14/1.72/1.40/1.15/0.66	52.6	53.2

For a 1.0 eV dilute nitride-based quad-junction cell, the target parameters are 12.1 mA/cm^2 short-circuit current, 0.62 V open-circuit voltage and 74% fill factor.

The target parameters for the 1.15 eV sub-cell under one sun illumination (filtered by the upper sub-cells) are 11.4 mA/cm^2 short-circuit current, 0.75 V open-circuit voltage and 77% fill factor.

The architecture with higher, Al-containing, bandgaps is more optimal and hence has a higher maximum efficiency. However, high quality 1.97 eV and 1.49 eV sub-cells containing aluminium have yet to be demonstrated in a germanium-based multi-junction

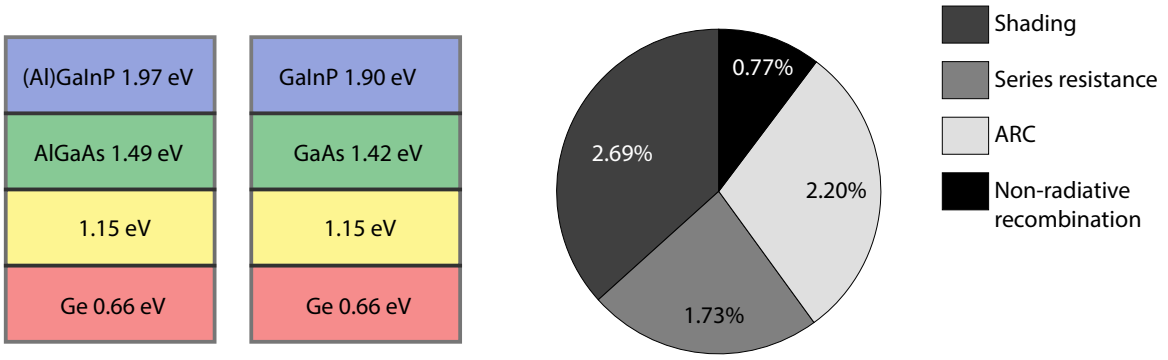


Figure 4.11: Schematic of 1.15 eV quad-junction architectures and breakdown of extrinsic losses (in percentage points). The 1.15 eV sub-cell may be composed of dilute nitride alloy containing less nitrogen than 1 eV material.

cell. Therefore it is of interest to calculate the potential of a 1.9/1.42/1.15/0.66 eV structure. Due to the lower bandgap of sub-cell 2, there is less current available for the 1.15 eV cell. However, it is known that GaAs sub-cells can produce strong radiative coupling [43] and provide extra current to the sub-cell below. A result of calculation is shown in Figure 4.12 using reported values of radiative coupling strength for GaInP/GaAs upper cells [43]. The necessary externally-induced current in the 1.15 eV sub-cell is lower due to this effect and so 50% efficiency can be reached with around 9.5 mA/cm^2/sun.

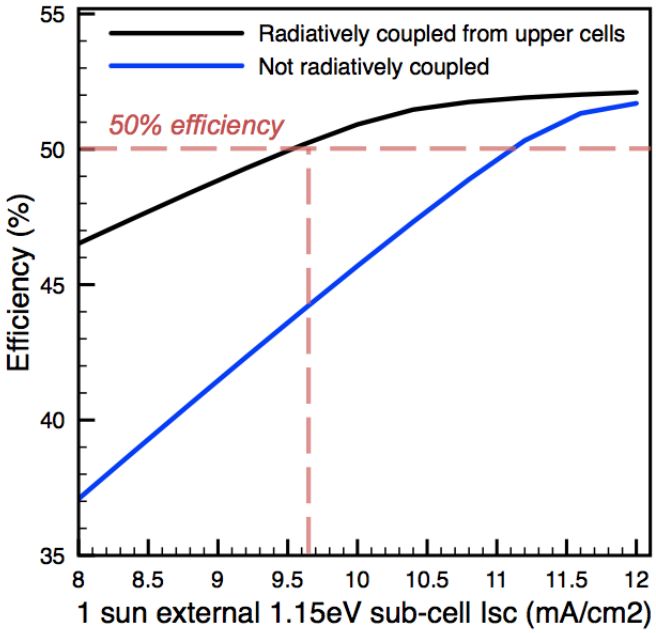


Figure 4.12: Calculation of the externally-induced sub-cell short-circuit current needed in the 1.15 eV sub-cell. If radiative coupling from upper sub-cells is present in a 1.9/1.42/1.15/0.66 eV cell limited by the third junction, with radiative coupling fractions as reported in [43], a higher efficiency MJSC will be produced with lower externally-induced current.

4.5 Conclusions

In this chapter several aspects of multi-junction solar cell design have been examined. The limit to the efficiency of triple-junction cells with current extrinsic losses is found to be around 46%. With similar magnitude losses, quad-junction cells will reach higher efficiency, with very well designed cells capable of reaching 50% efficiency. Sub-cells in the region of 1.15 eV and 1 eV are required for these high efficiency quad-junction structures. Although the 1 eV has been researched for some time, the 1.15 eV has not until now been identified as a priority sub-cell. These sub-cells typically need short-circuit current densities of > 11 mA/cm^2. With the benefit of high material quality, radiative coupling can reduce this value to 9.6 mA/cm^2.

GaAsSbN, with tunable lattice-matched bandgap between 0.9 and 1.4 eV, is a suitable candidate material for all high efficiency MJSC designs considered here.

Enhancement of multijunction solar cell power output and energy yield potentially providable by radiative coupling has been investigated for a number of optimal and sub-optimal device structures at the practical limit. The radiative coupling enhancement is calculated as a function of air mass, precipitable water and aerosol properties, and the expected power enhancement from radiative coupling under each parameter is quantified.

MJSC designs optimal for highest efficiency at AM1.5D can expect limited performance enhancement from radiative coupling under realistic spectral conditions, with energy yields from triple- and quad-junction structures estimated to improve by 0.76% and 1.02% respectively. A sub-optimal quad-junction design, where there is substantial variation in the short circuit current of each junction at reference conditions, can expect greater enhancement, on the order of 14% under favourable blue-rich conditions.

Chapter 5

Absorption properties of GaAsSbN alloys

Dilute nitride materials such as GaAsSbN offer the possibility for large changes in bandgap with relatively small variation of the nitrogen content and can meet the requirement for a 1 eV bandgap lattice-matched to GaAs. GaAsSbN is particularly interesting as Sb affects the valence band and N affects the conduction band independently through separate band anti-crossing interactions. These interactions split their respective bands and have been seen to increase the electron effective mass in dilute nitride alloys. This chapter explores the effects of Sb and N composition on the band structure and develops a model dielectric function to determine the factors that control the absorption coefficient of the material.

1 eV was originally identified as a component sub-cell for several optimal multi-junction designs. However, nitrogen has a detrimental effect on certain aspects of material quality, in particular minority carrier transport [72]. As a result it can be challenging to produce adequate current generation in order to avoid the dilute nitride sub-cell limiting the entire multi-junction stack. Therefore it is important to accurately understand the absorption profile of the material in order to design optimal sub-cells to enable high efficiency multi-junction cells.

The absorption characteristics of GaAsSbN are calculated by first considering the band structure, which is modified independently by N and Sb. Although only one composition is available for direct experimental study, literature data is used to consider the the variation in composition of N and Sb and the factors that control the absorption of the quaternary material are determined. In particular, the competing bandgap reduction effects of N and Sb are assessed. This will be valuable for general device modelling in order to improve the design of GaAsSbN sub-cells, helping to establish appropriate material compositions to achieve a given bandgap.

5.1 Direct measurement of absorption coefficient

Absorption below the band-gap of GaAs has been measured using reflection and transmission measurements on a double-polished sample (N2436). See Table A.3 for full sample structure. The sample structure was a 400 nm layer of undoped GaAsSbN deposited on an undoped GaAs substrate. The absorption coefficient was determined using the method detailed in section 3.2. Due to the absence of doping, free carrier absorption is not expected to be significant in this sample. Figure 5.1 shows a comparison of the GaAsSbN absorption coefficient to other dilute nitride materials found in literature. It was not possible to obtain data for the absorption coefficient of GaAsSbN at energies >1.4 eV using transmission and reflectance due to absorption of the transmission by the GaAs substrate.

5.2 Model dielectric function approach

A relatively simple band anti-crossing (BAC) model has been demonstrated to describe the band properties of highly (electronegativity) mismatched alloys such as dilute nitrides [57, 76]. This model posits that the interaction between e.g. a localised nitrogen level and the extended conduction band states of the host semiconductor effectively splits

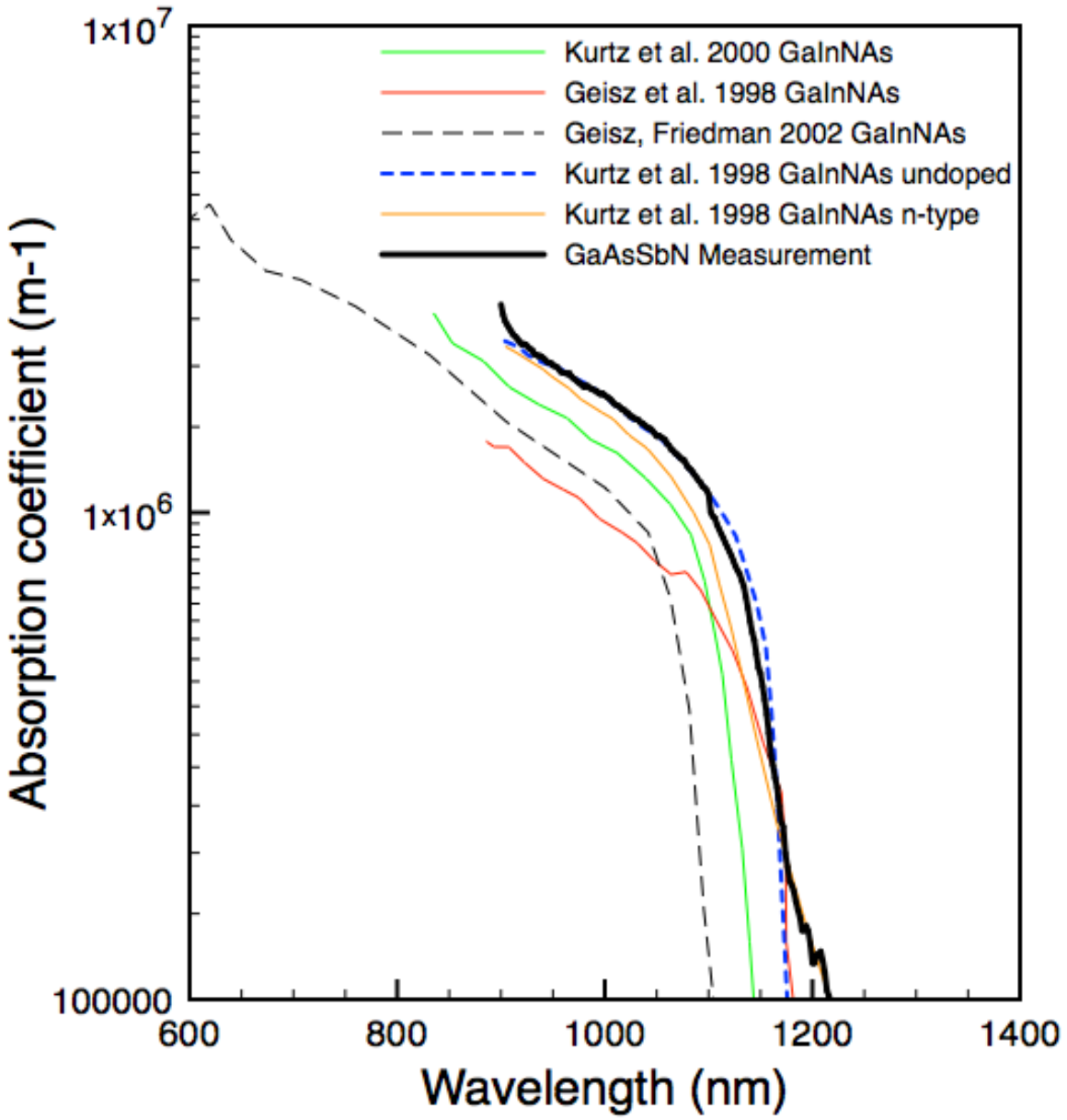


Figure 5.1: Comparison of literature data (referenced in Table 5.1) for dilute nitride material absorption coefficients with absorption coefficient of GaAsSbN measured for this thesis using reflection and transmission. All data was recorded at approximately 293K.

Table 5.1: References for dilute nitride alloy absorption coefficient data reproduced in Figure 5.1

Label in figure	Reference
Kurtz et al. 2000 GaInNAs	[73]
Geisz et al. 1998 GaInNAs	[46]
Geisz, Friedman 2002 GaInNAs	[74]
Kurtz et al. 98 GaInNAs undoped	[75]
Kurtz et al. 98 GaInNAs n-type	[75]

the conduction band into two bands, E_+ and E_-. The model has been particularly successful for determining the position of the E_- band and consequent material bandgap and a modified version accounting for a distribution of nitrogen states has been shown to accurately describe further properties [77]. In the case of GaAsSbN, both Sb and N produce BAC interactions, which affect the valence band and conduction band respectively. It is assumed here that these two interactions are independent. A double BAC model may be employed that combines separately demonstrated conduction BAC and valence BAC models for N and Sb [78]. The determination of transition energies at critical points in the band structure using a technique such as modulated reflectance then allows a parameterisation of the complex dielectric function and corresponding absorption coefficient, as described in Section 2.1.2, as an analytical function of incident photon energy.

The dielectric function of GaAsSbN has been studied using spectroscopic ellipsometry data for fixed Sb compositions of GaAsSbN by Ben Sedrine et al. [79]. However, upon comparison to experiment conducted for this thesis, it was found that the data provided in [79] did not accurately represent the near-bandgap behaviour of the material. The material GaAsN has been treated with a model dielectric function [80] used to fit ellipsometry measurements. The model in [80] does not consider the band anti-crossing effect but presents a parameterisation of observed trends. The calculated dielectric function of

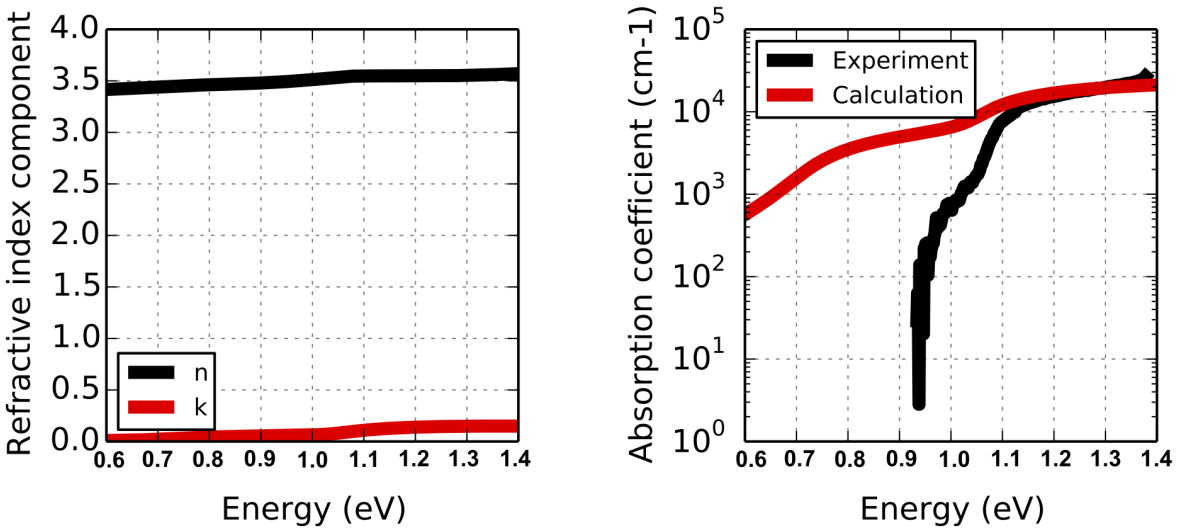


Figure 5.2: Calculated complex refractive index of GaAsN based on the model dielectric function method and parameters determined by ellipsometry of [80]. It can be seen that the absorption coefficient as calculated by [80] for GaAsN has a much broader tail than the measured absorption of GaAsSbN presented in this thesis.

GaAsN from [80] is shown in Figure 5.2 for the energy range of interest for the application of GaAsSbN to multi-junction solar cells. The resultant complex refractive indices, n and k are shown in Figure 5.2. It can be seen that the absorption coefficient as calculated from [80] for GaAsN has a much broader tail than the measured absorption for GaAsSbN. It is therefore important to accurately determine the transitions in the material using a technique such as electroreflectance.

In this chapter electroreflectance is used to determine critical points in the band structure of GaAsSbN. This is combined with use of the double BAC model to give a model dielectric function that can be applied to GaAsSbN. Literature data on the compositional variation of the dielectric function of GaAsN [80] and GaAsSb [27] is used to calculate a compositional variation of the absorption of GaAsSbN.

5.2.1 Electroreflectance measurement and fitting

The electroreflectance of a GaAsSbN homojunction cell was measured as described in Section 3.3. The cell was N2627, a GaAsSbN homojunction cell with a 200 nm thick 1×10^{18} cm^{-3} n-type emitter layer and a 1000 nm thick 1×10^{17} cm^{-3} p-type base layer. The cell had a 50 nm thick $Al_0.7Ga_0.3As$ window layer. See Table A.5 for full sample structure.

A waveform generator was used to apply voltage to the device with square wave variation and a halogen lamp with monochromator provided illumination. The resulting change in reflectance was detected using Si and Ge photodiodes with a lock-in amplifier. Figure 5.3 shows the obtained $\Delta R/R$ spectrum. To record ΔR, the device was held at 0 V DC bias and a square-wave oscillating voltage of ± 0.5 V was applied at a frequency of 723 Hz. Several derivative lineshape features can be seen that correspond to transitions in the material. The lower energy feature is the fundamental bandgap of the material, followed by two higher energy transitions around 1.5 eV and 1.8 eV. Franz-Keldysh oscillations do not appear to be present.

Figure 5.3 also shows the results of fitting Aspnes' third derivative lineshape equation [65] to each feature:

$$\Delta R/R = Re[Ce^{i\theta}(E - E_g + i\Gamma)^{-n}] \tag{5.1}$$

where C and θ are amplitude and phase factors that vary slowly with E, E_g determines the energy location of the structure and Γ the width. n is representative of the critical point type, with $n = 3$ for two dimensional parabolic critical points and $n = \frac{5}{2}$ for three dimensional critical points.

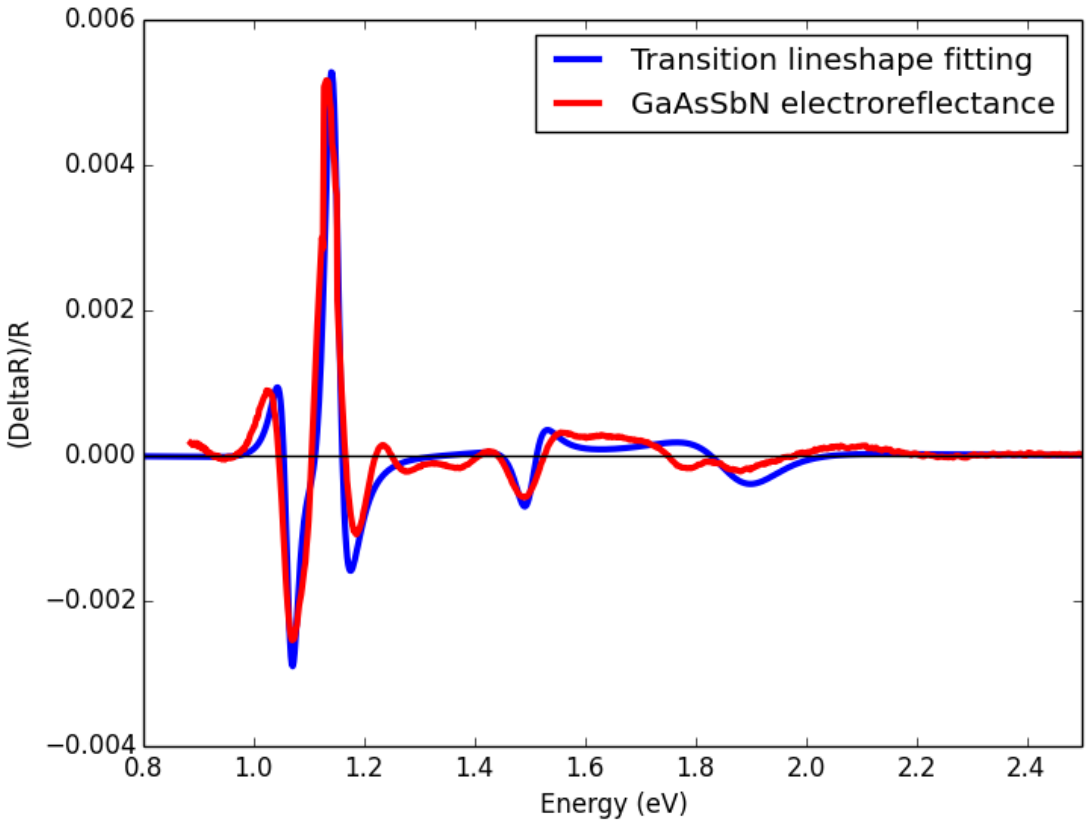


Figure 5.3: Electroreflectance spectrum of 1eV GaAsSbN *np* junction N2627. Several lineshape fits were performed based on Aspnes' formula [65], providing information on the energy location, broadening and amplitude of the transition.

5.2.2 Contributions to dielectric function

A model dielectric function is used to build a consistent model for the measured absorption coefficient using contributions from the transitions measured by the electroreflectance. The model is based on that described in Section 2.1.2.

The contribution from the fundamental direct bandgap transition, labelled E_0 with split-off energy $\Delta 0$, is given by Eq. (2.11) and Eq. (2.12).

In [80], the A, E_0 and Δ_0 parameters as well as a broadening parameter are inferred from fitting ellipsometry data using the above equations, whereas in this thesis they are measured more directly from electroreflectance. To implement the broadening of a transition measured through electroreflectance, the following substitution was used:

$$E = E + i\gamma \tag{5.2}$$

With γ as the broadening parameter.

It was found in the electroreflectance measurement that there were additional transitions with energies between E0 and E_1. These here are treated as having the same nature as E_0 but with different parameters.

The total dielectric function is then given by:

$$\epsilon = \epsilon^{E_0} + \epsilon^{E_0 2} + \epsilon^{E+} + \epsilon^{E_0+\Delta_0} + +\epsilon^{higher} \tag{5.3}$$

Where ϵ^{E_0} is attributed to the transition from the upper valence band to $E-$ conduction band, $\epsilon^{E_0 2}$ is from the strain split lower valence band to the $E-$ conduction band, ϵ^{E+} is the transition from the valence band to the $E+$ conduction band and ϵ^{higher} are the E_1, E_2 higher energy transitions, unchanged from GaAs.

The refractive index is then derived as in Section 2.1.2, with $\epsilon_1 = \mathrm{Re}(\epsilon)$ and $\epsilon_2 = \mathrm{Im}(\epsilon)$.

A number of N compositions were grown by the authors of [80] and the trend investigated. The form of their trend is used here - interpolated either side of the composition of

GaAsSbN studied by electroreflectance in order to extrapolate to other compositions not experimentally studied here. The parameters as a function of Sb content are interpolated using data for GaAsSb reported in the literature [27]. It is therefore assumed that N and Sb BAC interactions affect the material independently. This is justified by the fact that N appears to affect the conduction band and Sb the valence band. Changes in the bandgap due to conventional alloying are accounted for using the virtual crystal approximation but are less significant than the BAC interactions. Furthermore, the BAC interaction of N is more significant than Sb. The interpolation of the relaxed material lattice constant for the quaternary alloy follows Vegard's law:

$$a = (1 - y - x)a_{GaAs} + y * a_{GaN} + x * a_{GaSb} \tag{5.4}$$

where a is the lattice constant of a given material, y is the nitrogen composition and x the antimony composition. The cubic form of GaN is used.

5.3 Results and discussion

The electroreflectance measured from a 1.05 eV GaAsSbN device (N2627) is shown in Figure 5.3. Several features can be seen, the most prominent of which is around the bandgap, correlating to the position of the quantum efficiency edge as well as photoluminescence of the sample. There are also features near 1.5 eV and 1.87 eV that are attributed to transitions from the split-off band to the $E-$ conduction band and from the upper valence band to the $E+$ conduction band respectively.

However, as there is an $Al_{0.7}Ga_{0.3}As$ layer at the surface of the sample with expected bandgap of 2.17 eV, there is some uncertainty in fitting the high-energy features and further investigation of the transition to $E+$ would be desirable. Additionally, the bandgap transition appears to have two closely-spaced features, which is tentatively attributed to strain-induced non-degeneracy of the light hole and heavy hole valence bands. The fit

Table 5.2: Electroreflectance fitting parameters

Transition	E_g (eV)	C	Γ (eV)
E_0	1.064	1.0	0.026
E_{02}	1.145	3.0	0.031
E_+	1.50	0.8	0.040
$E_0 + \Delta 0$	1.87	8.7	0.13

Table 5.3: Lattice constants of GaAs, GaSb, GaN used for interpolation of GaAsSbN properties

Material	Lattice constant ($\times 10^{-10}$ m)
GaAs	5.6533
GaN (cubic)	4.5
GaSb	6.09593

shown in 5.3 is based on Eq. (5.1) applied to each of these transitions. Using this, the parameters displayed in Table 5.2 can be found for the four lineshapes. The lineshapes were treated as three dimensional parabolic critical points with $n = 2.5$.

Note the increase in Δ_0 from to 0.44 eV compared to 0.34 eV for GaAs is due to the BAC effect of Sb in the conduction band. The BAC model also requires parameters for Eq. (2.44). These were found by fitting the bandgap measured in sample N2627 (obtained from quantum efficiency and photoluminesence) with the equations. E_N was assumed to be 1.65 eV, in common with other dilute nitride materials, with $C_N = 2.7$ eV. E_{Sb} was -1.0 eV with $C_{Sb} = 1.05$ eV. Table 5.3 shows the parameters used for quaternary alloy interpolation of lattice constant. Offsets of 0.2, 0.5 and 0.09 eV were assumed for the interaction between GaAs and GaSb CB, VB and SO bands respectively.

The experimentally measured absorption coefficient for GaAsSbN (from sample N2436) is shown in Figure 5.4 alongside a comparison to GaAs. It can be seen that the absorption edge has been broadened in the GaAsSbN sample. Also plotted is the absorption

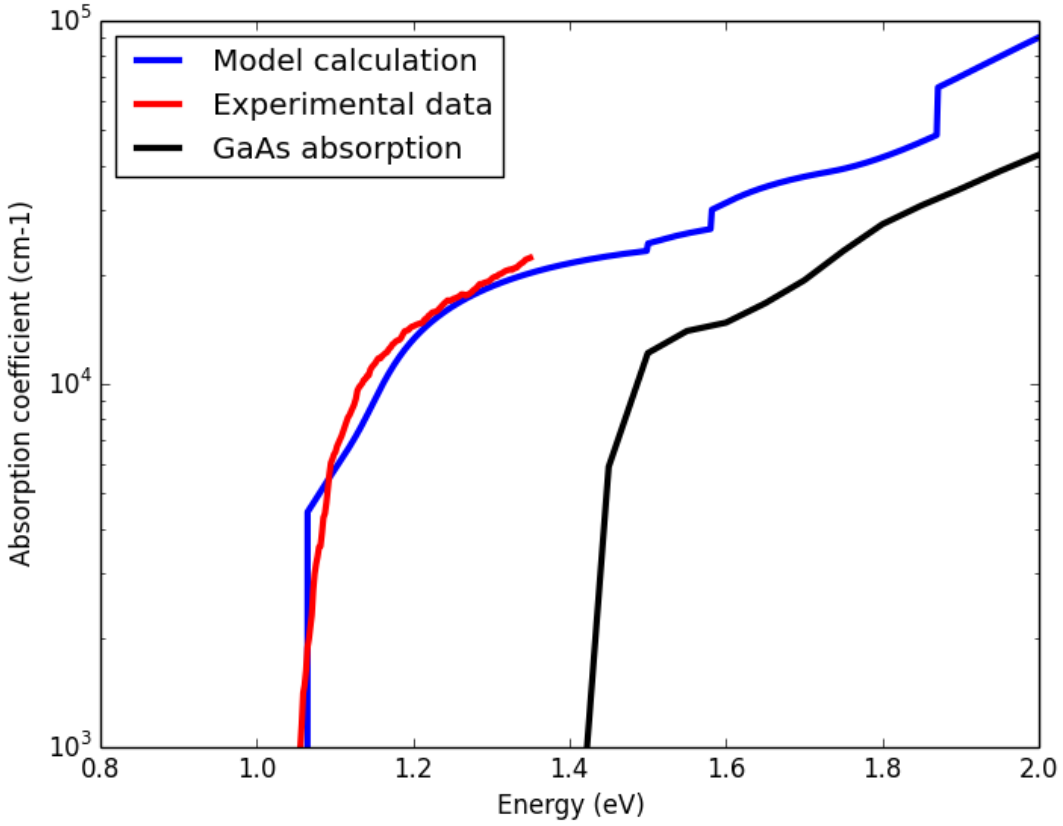


Figure 5.4: Comparison of experimentally determined absorption coefficient with that calculated by model dielectric function based on the measurement of electroreflectance of GaAsSbN. Temperature is 293K.

coefficient result of the model dielectric function using the parameters obtained from electroreflectance. The parameters for this were deduced from the electroreflectance fitting of sample N2627. The difference in broadening at the edge of the calculated and measured absorption coefficient may be due to a difference in nitrogen incoroporation between the device that electroreflectance was measured from and the epilayer that the absorption coefficient was measured from. Examining the photoluminescence of the two samples (Figure 5.5) gives some evidence of this. N2436 shows a broad low energy (high wavelength) tail indicating that there are more lower energy states than for the device sample, which has a sharper photoluminescence. There is also a small difference in peak emission energy between samples. N2436 has peak emission at 1154 nm (1.07 eV) whereas N2627 has peak emission at 1144 nm (1.08 eV).

The compositional dependence of GaAsSbN properties on N and Sb content was then investigated by combining this calculation of the absorption coefficient with the double BAC model [78] and linear parameter interpolation from literature for GaAsN and GaAsSb. The effects of N and Sb composition were treated independently due to the fact that the effect of the respective elements on conduction band and valence band is mostly independent.

The calculation of E_0 bandgap energy is shown as a function of GaAsSbN composition in Figure 5.6. Both 1 eV and 1.15 eV bandgaps can be achieved with low quantities of N and Sb. It can be seen that increasing N composition has a stronger bandgap reduction effect than Sb. The black lines, showing the fraction of lattice mis-match with GaAs, show that it is possible to access a wide range of bandgaps lattice-matched to GaAs by appropriately varying Sb and N composition.

In order to be a useful component in a MJSC, GaAsSbN alloy sub-cells must generate sufficient current when filtered by the absorption of the sub-cells above, particularly GaAs. Figure 5.7 shows an estimated short-circuit current density at wavelengths longer than the GaAs bandgap (870 nm) as a function of alloy composition. This was calculated using

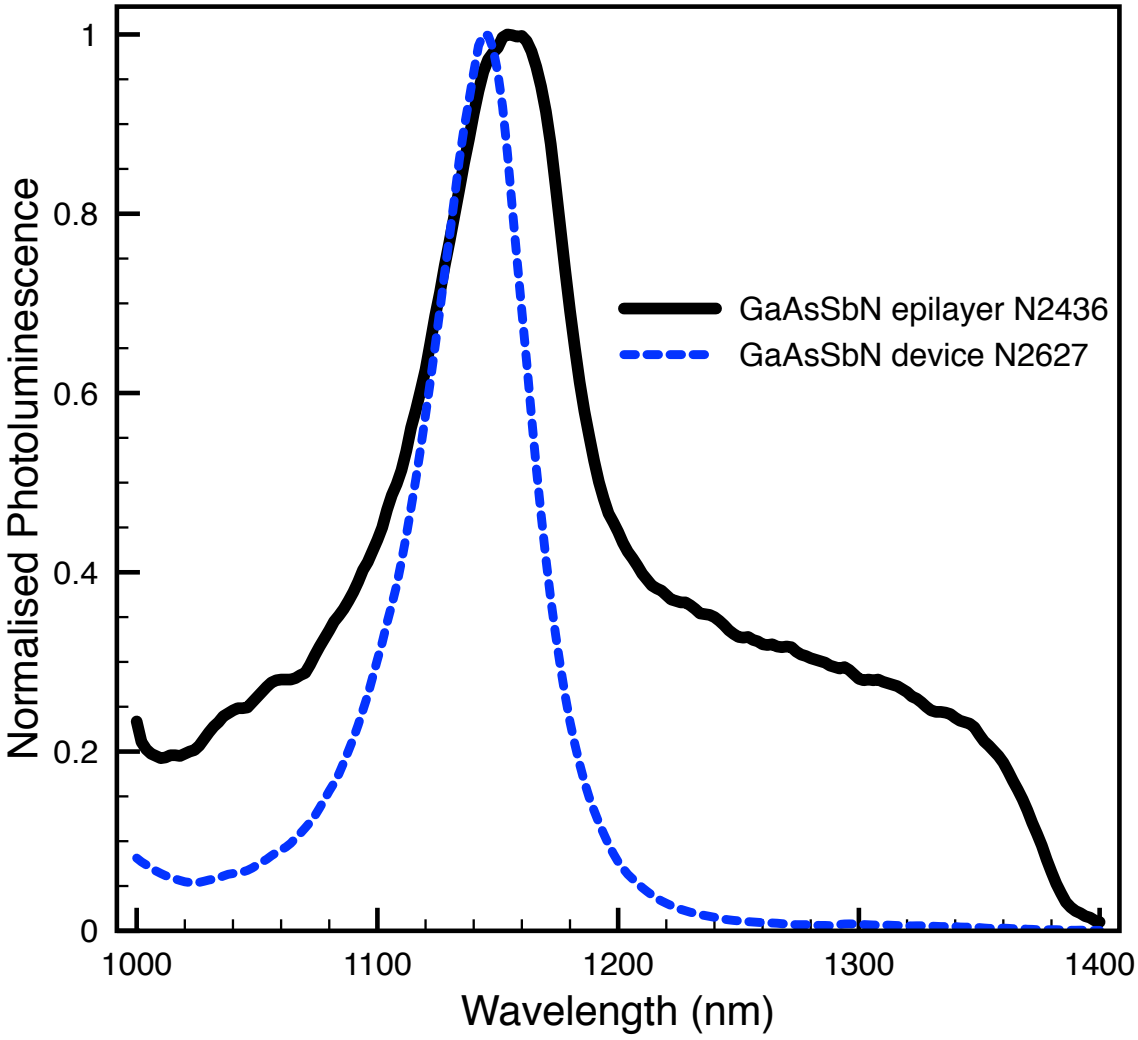


Figure 5.5: Photoluminescence of the two samples discussed in this chapter measured at 293K. Sample N2436 shows broader emission, particularly at low energies. This sample was used to measure the absorption coefficient of GaAsSbN. The device sample N2627 was used to measure electroreflectance. Photoluminescence was measured under the same conditions with 900 nm Ti:Saph laser excitation and GaInAsP-based PMT detector.

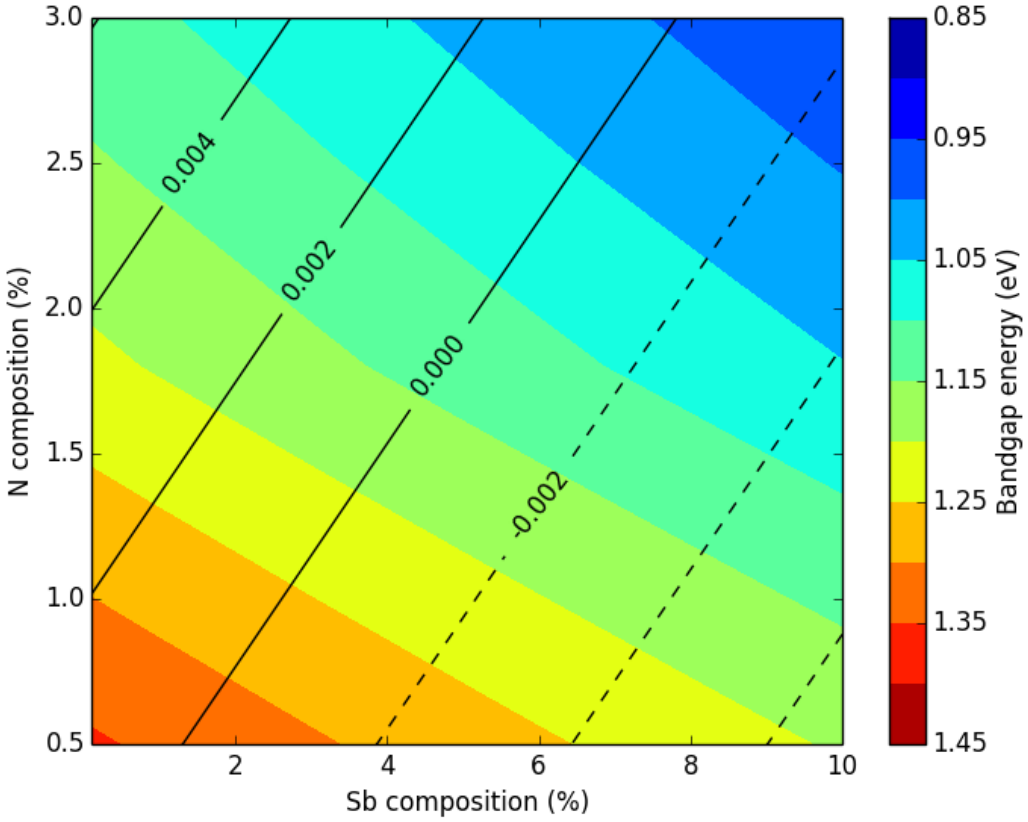


Figure 5.6: Bandgap energy of GaAsSbN as function of N and Sb composition. The solid black lines show the fraction of lattice-mismatch to GaAs.

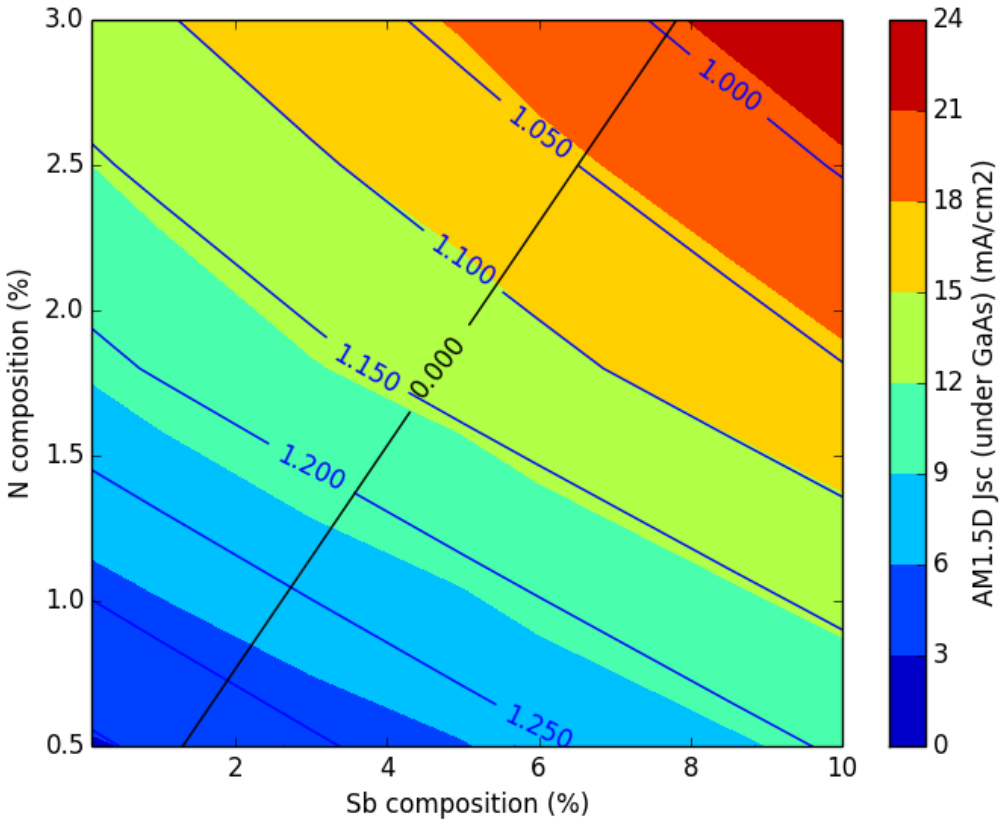


Figure 5.7: Short-circuit current density (J_{SC}) calculated from the model absorption coefficient as a function of Sb and N composition, taking into account the N-induced broadening and N and Sb-induced amplitude variation of transitions with composition.

Eq. (2.1) assuming that every photon absorbed generates an electron hole pair that flows through the external circuit.

High amounts of current are possible under the AM1.5D spectrum, assuming 3 μm sub-cell thickness, short-circuit currents of around 12-15 mA/cm^2 are of interest for quad-junction or triple-junction structures respectively. This is based on the full absorption calculation, taking the transition energies from the double BAC model and including the compositionally dependent variation in broadening and amplitude of the critical points from literature. The bandgap energy is plotted with blue solid lines. It can be seen that there is a slight difference in the trend of bandgap with composition and absorption with composition. This is because increasing N content can broaden and weaken the near-bandgap absorption moreso than increasing Sb content.

This shows that GaAsSbN has the potential to be a useful tunable absorber in high efficiency lattice-matched multi-junction solar cells.

5.4 Conclusions

GaAsSbN is a promising material for lattice-matched sub-cells with bandgaps below GaAs in multi-junction solar cells. In particular, it can be grown lattice-matched to GaAs with a range of bandgaps between 1.4 eV and 0.9 eV. Accurate knowledge and control of the absorption coefficient, independently influenced by band anti-crossing interactions in valence and conduction band through Sb and N composition, will enable optimisation of device design. Further study of varying compositions would allow this to be described more accurately. With sub-cells designed to maximise absorption and collection in the space charge region, this will assist with improvement of device results.

Chapter 6

Carrier dynamics of GaAsSbN

This chapter presents photoluminescence (PL) and time-resolved photoluminescence (TRPL) measurements taken using a streak camera for a range of double-heterostructure samples. The TRPL measurements were taken using a near-infrared 20 ps resolution streak camera, described in Section 3.4.2. Layers of different thickness and doping are investigated. A difference in behaviour with dopant polarity is noted, with p-type material exhibiting longer minority carrier lifetimes. Thickness of the GaAsSbN layer is varied in order to separate interface recombination from bulk recombination. The minority carrier lifetime of GaAsSbN at different doping levels and dopant type is investigated. The temperature dependence of the luminescence of p-type layers and n-type layers is also investigaed. Properties observed with changes in temperature are similar to those that have been attributed to localised exciton recombination in GaInNAs [62]. Results including effective lifetime values are compared to literature reports for GaAsSbN and GaInNAs(Sb). Implications for device design and performance are discussed.

Table 6.1: Double heterostructure sample set for time-resolved photoluminescence of GaAsSbN. Full details are in Appendix A.

Sample	GaAsSbN thickness (nm)	GaAsSbN doping (cm^{-3})	Barrier material	Effective lifetime at 300K (ns)	Peak emission wavelength (nm)
N2765	100	*p*-type 1e17	GaAs	0.42	1140
N2761	200	*p*-type 1e17	GaAs	0.43	1125
N2766	500	*p*-type 1e17	GaAs	0.45	1133
N2767	100	*p*-type 1e17	$Al_{0.7}Ga_{0.3}As$	0.23	1150
N2762	200	*p*-type 1e18	GaAs	0.25	1157
N2763	200	*n*-type 1e17	GaAs	0.25	1160
N2764	200	*n*-type 1e18	GaAs	0.20	1144
N2760	200	Unintentional	GaAs	0.40	1158

6.1 Sample design

A set of DH samples was grown by molecular beam epitaxy (MBE), in conjunction with a radio frequency plasma-assisted nitrogen source and valved cracker antimony source. The structures are shown in Table 6.1 and a schematic is shown Figure 6.1. Full layer structures are given in Appendix A. The thickness and doping of the GaAsSbN layer was varied. GaAs was used as barrier material in most cases.

Sample N2767 used $Al_{0.3}Ga_{0.7}As$ barriers in order to compare the difference between GaAsSbN/GaAs interfaces and GaAsSbN/AlGaAs interfaces. Dopant levels were chosen to correspond to potential emitter and base layers in device designs. Barrier layers were unintentionally doped. Thickness was varied in samples N2765, N2761 and N2766 in order to separate effective lifetime into interface recombination and bulk recombination as described in [81]. Eq. (6.1) may be used to calculate the contribution of each to effective lifetime [81].

$$\frac{1}{\tau_{effective}} = \frac{1}{\tau_{bulk}} + 2\frac{s}{d} \tag{6.1}$$

where $\tau_{effective}$ is the measured lifetime, τ_{bulk} the bulk lifetime, s the surface recombination velocity and d the thickness of the sample.

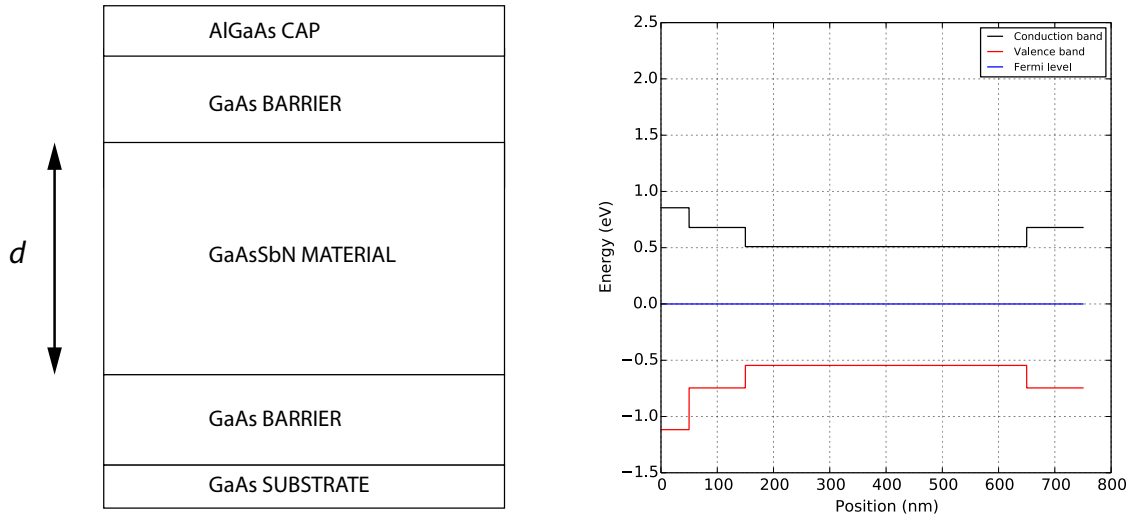


Figure 6.1: (Left) Schematic of double heterostructures grown for TRPL study. The thickness, d and doping of the GaAsSbN layer is varied. The cap is made from $Al_{0.3}Ga_{0.7}As$, which was used as a barrier material in one sample. (Right) Band diagram of structure with 500 nm thick GaAsSbN layer and GaAs barriers showing how carriers are confined to GaAsSbN layer.

6.2 Photoluminescence method

A mode-locked Ti:sapphire laser tuned to 900 nm with pulse width of 140 fs was used to directly excite the GaAsSbN below the barrier bandgap. Laser repetition rate of either 1 MHz or 4 MHz (via a pulse picker) and incident average power of either 100 W or 900 W was used for various measurements, creating a low level of minority-carrier injection. The laser spot was 50 μm diameter. A near-infrared streak camera with 20 ps temporal resolution was used to detect both time-integrated and time-resolved photoluminescence.

Each sample was measured at room temperature, with the temperature dependence of N2761 and N2763 examined in more detail.

6.3 Results and discussion

Decay profiles of either single exponential or more complex stretched/multi-exponential were observed for different samples at different temperatures. Streak camera images for each sample can be found in Appendix B. At room temperature (293K) the longest 1/e effective lifetime at peak wavelength 1140 nm (1.09 eV) is 0.45 ns, for sample N2766. An overview of room temperature results in the form of effective lifetime at the peak wavelength is shown in Table 6.1. Lifetimes of 200 to 400 ps are measured. A recent report comparing lifetimes in GaInNAs and 1 eV GaAsSbN [82] found values of 900 ps and below 100 ps respectively.

At room temperature the dominant recombination mechanism appears to be non-radiative, producing sub-nanosecond lifetimes. A generalized form of calculation for the radiative coefficient B [83] in combination with the relation $\tau_{rad} = 1/(BN)$, where N is majority carrier doping concentration, provides radiative lifetimes of nanosecond order that change with orders of magnitude with doping concentration. Neither of these properties are observed here, although the calculation for B used above does assume GaAs-like semiconductor. It is not unexpected that dilute nitride material should be limited by non-radiative SRH recombination however, due to the occurrence of defects.

6.3.1 Interface and bulk recombination

A plot using Eq. (6.1) to separate interface from bulk recombination in the samples with varying width (N2765, N2761, N2766) can be seen in Figure 6.2. Several values of interface recombination are plotted for comparison. It can be seen that the error due to the 20 ps resolution introduces some uncertainty into the value of the interface recombination.

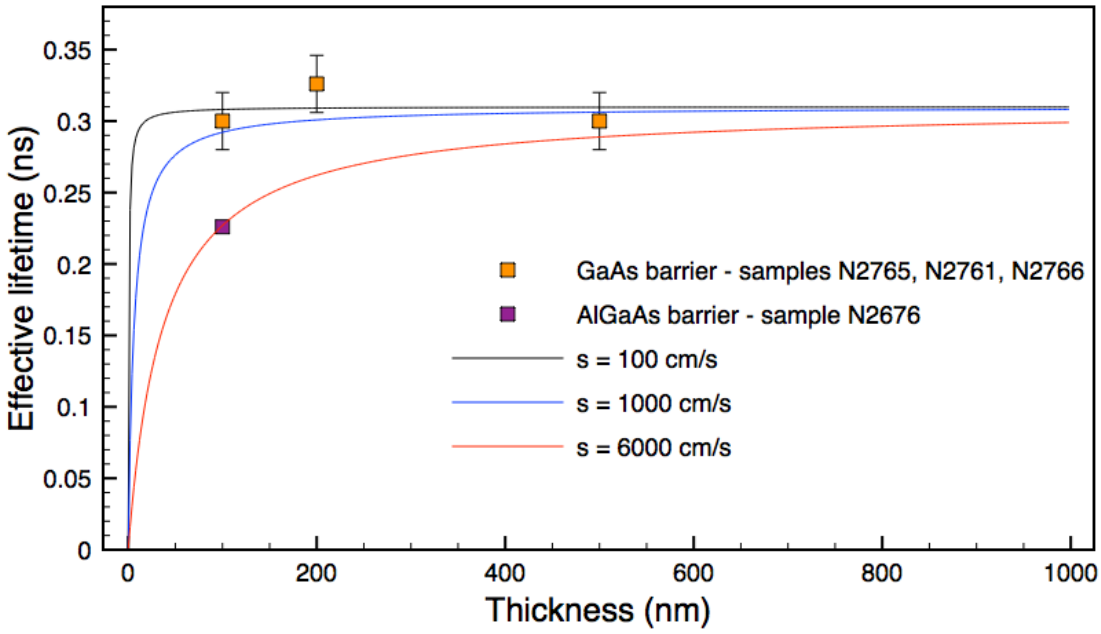


Figure 6.2: Effective lifetime variation with layer thickness. Using Eq. (6.1), bulk lifetime is around 0.31 ps for the GaAs barrier samples N2765, N2761, N2766. Eq. (6.1) is plotted for several values of interface recombination for this bulk lifetime. Assuming the same bulk lifetime for sample N2767, with AlGaAs barriers, indicates that the interface recombination is higher at this interface.

However the data seem to indicate that interface recombination is low with GaAs barriers. The sample with AlGaAs barriers has lower measured lifetime for nominally the same bulk material compared with the sample with GaAs barriers, suggesting higher interface recombination is present. Comparison of the decay profile of these two samples is shown in Figure 6.3.

6.3.2 Variation with dopant properties

In Table 6.1 and Figure 6.4 it can be seen that there is a trend with doping, with n-type Si-doping reducing the room temperature lifetime more than p-type Be-doping. For a

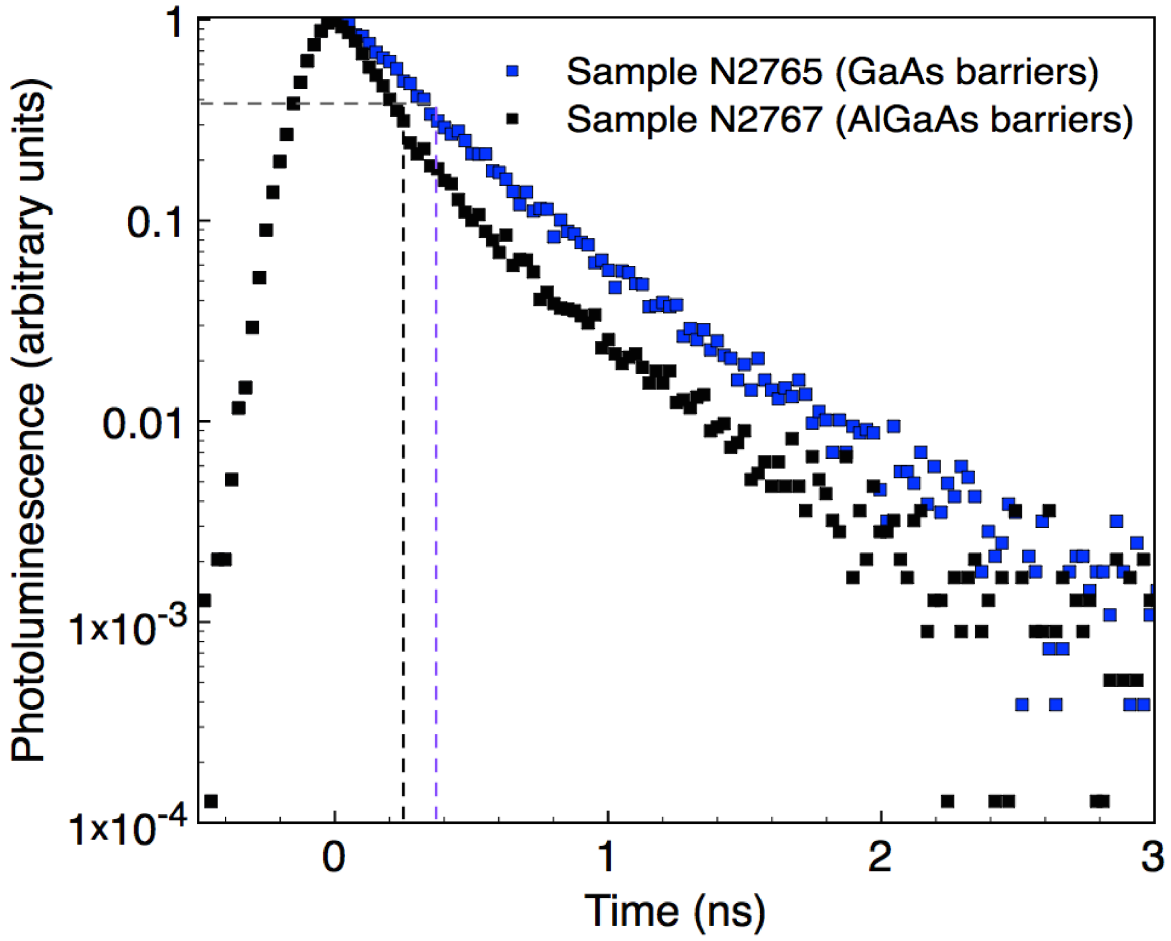


Figure 6.3: Decay profile for emission at the peak emission wavelength of samples with different barrier material but otherwise identical structure. Measurements were taken at 293K. For both samples, the GaAsSbN material was excited directly with no absorption by the barrier. The dotted lines indicate the time by which the emission has fallen to 1/e of its original value. It can be seen that the AlGaAs barrier sample has reduced effective lifetime, indicating a higher interface recombination velocity.

radiative band-to-band recombination process the minority carrier lifetime is inversely proportional to majority carrier concentration, and this is not observed from Figure 6.4, suggesting that the dominant recombination mechanism at room temperature is non-radiative (Shockley-Read-Hall) recombination.

At low temperature of 3K, the effects of dopant polarity are reversed, with n-type material exhibiting far longer lifetimes. This is shown in Figure 6.5.

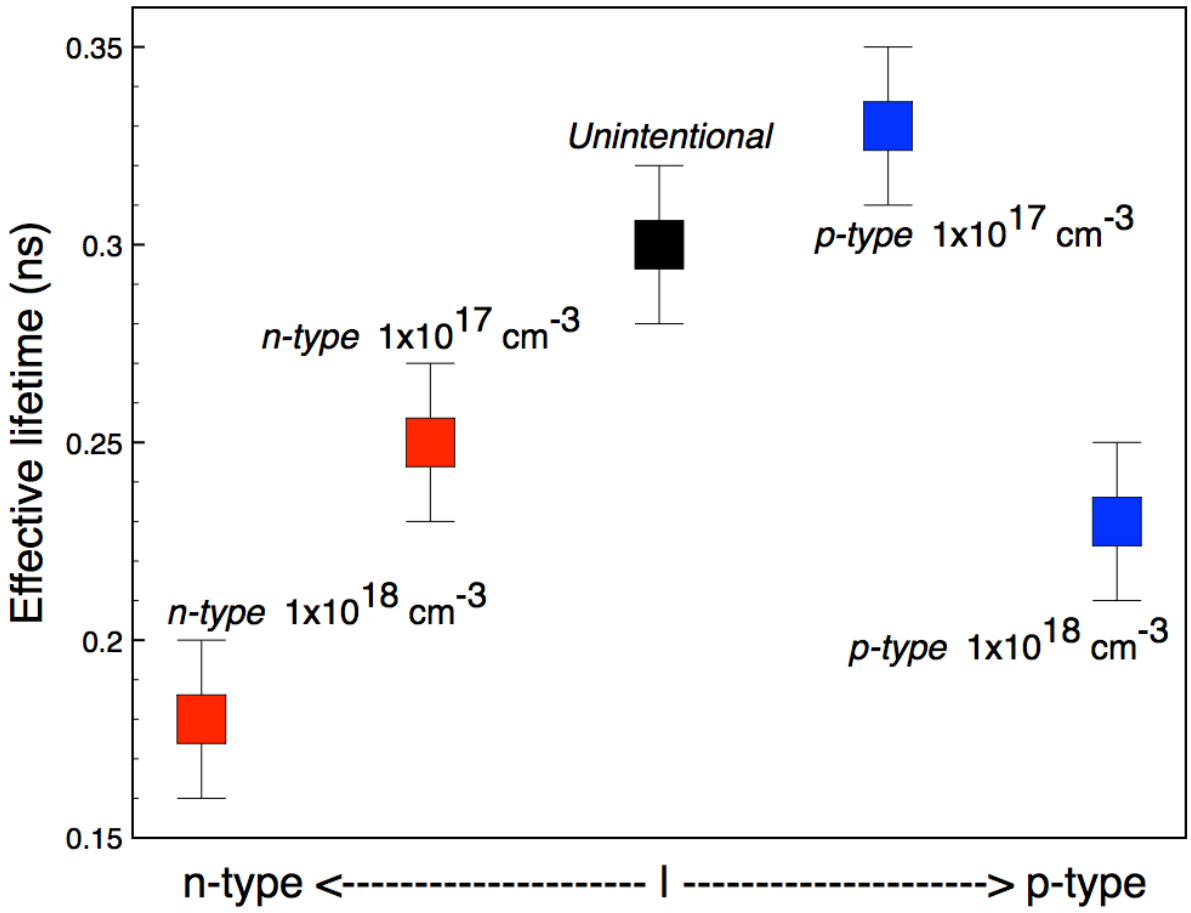


Figure 6.4: Variation of effective lifetime with doping at room temperature. n-type Si doping appears to be more detrimental than p-type Be. The unintentional doping is expected to be p-type of around $8 \times 10^{15} cm^{-3}$.

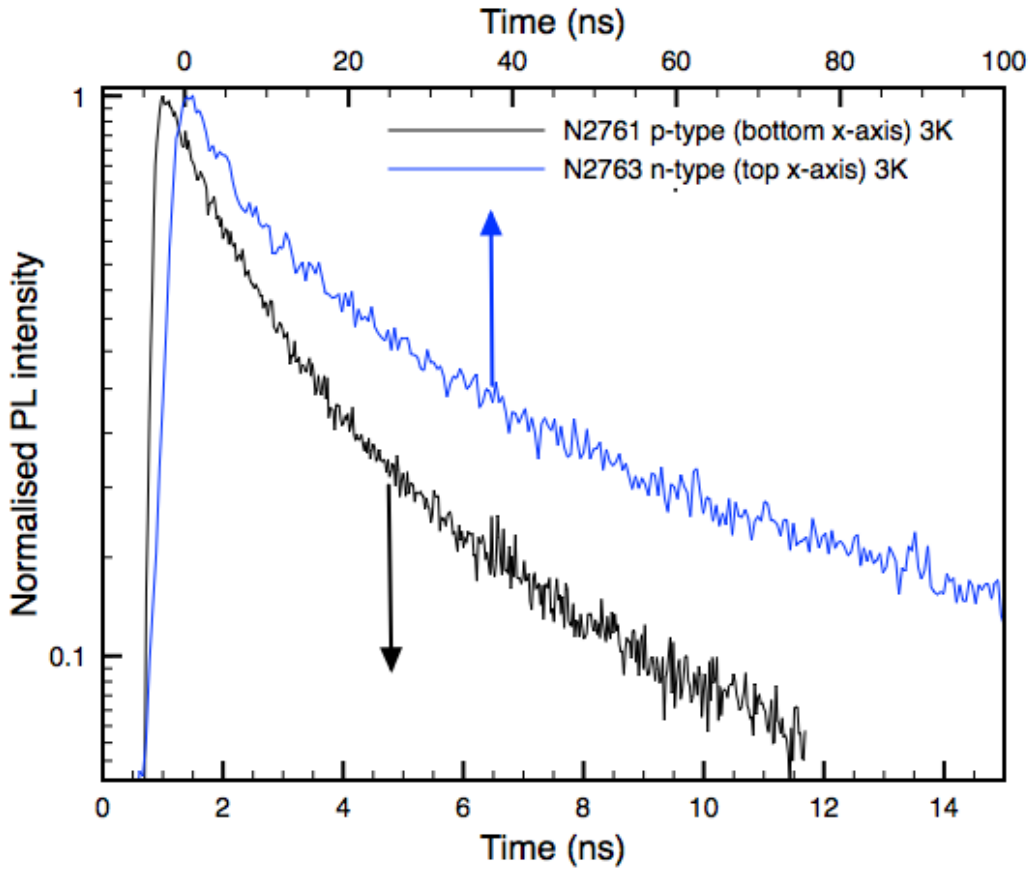


Figure 6.5: Emission profile at the peak emission wavelength for opposite polarity doped samples at 3K. n-type Si doping appears to have far longer lifetime than p-type Be.

6.3.3 Carrier localisation effects

Emission intensity and peak wavelength varied between samples, with the peak emission energy typically a few hundred meV above 1 eV. This variation in energy is attributed to fluctuations in nitrogen content between samples. A dependence on excitation power for effective lifetime was also found, with lifetime decreasing slightly with increasing power.

With changing temperature, the PL peak wavelength position exhibited an 's-shape' that has been observed in other dilute nitride alloys and has been attributed to carrier localisation [62]. This is shown in Figure 6.6. It is interesting to note that as well as different lifetimes at room temperature, the n-type samples and p-type samples exhibit contrasting temperature dependence in the low temperature region. At low temperature, the situation is reversed, with n-type samples having far longer lifetimes than p-type. At low temperature, Si-doped n-type GaAsSbN shows far longer lifetime than the other samples in this study. Doping also changes the shape of the time-integrated PL, with Si-doped GaAsSbN having broader emission, particularly at low temperature.

Localisation induced by compositional fluctuation can also lead to a dispersion of carrier lifetime with emission energy, particularly at low temperatures. This is shown in Figure 6.7. It can be seen that the lifetime is enhanced at lower energies and shorter at higher energies, characteristic of recombination through localised states.

The degree of localisation may also be estimated from the difference in peak energies in the low temperature, non-Varshni regime. In Figure 6.6 this is below 75 K. Additionally, it can be seen that the n-type sample N2763 exhibits greater carrier localisation than p-type N2761. This result is very similar to the one reported by Tsai et al. [62] for GaInAsN, suggesting that the properties of GaAsSbN are similar.

A difference in photoluminescence and time-resolved photoluminescence depending on dopant polarity is therefore seen in terms of room temperature effective lifetimes, low temperature effective lifetimes, PL shape and behavior with temperature. It is therefore

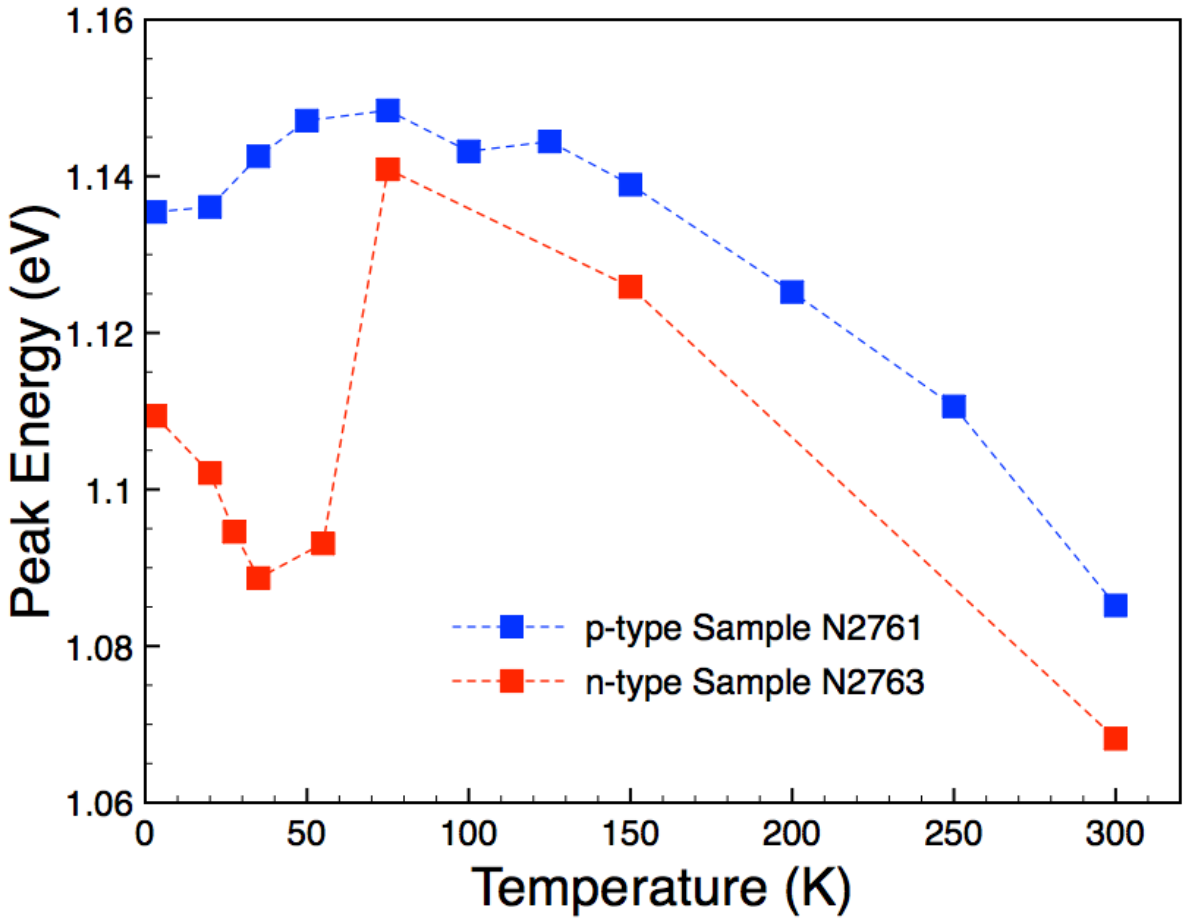


Figure 6.6: Shift in photoluminescence peak energy position with temperature. The behavior at low temperature is governed by localized exciton recombination and is more prominent for n-type material than p-type material.

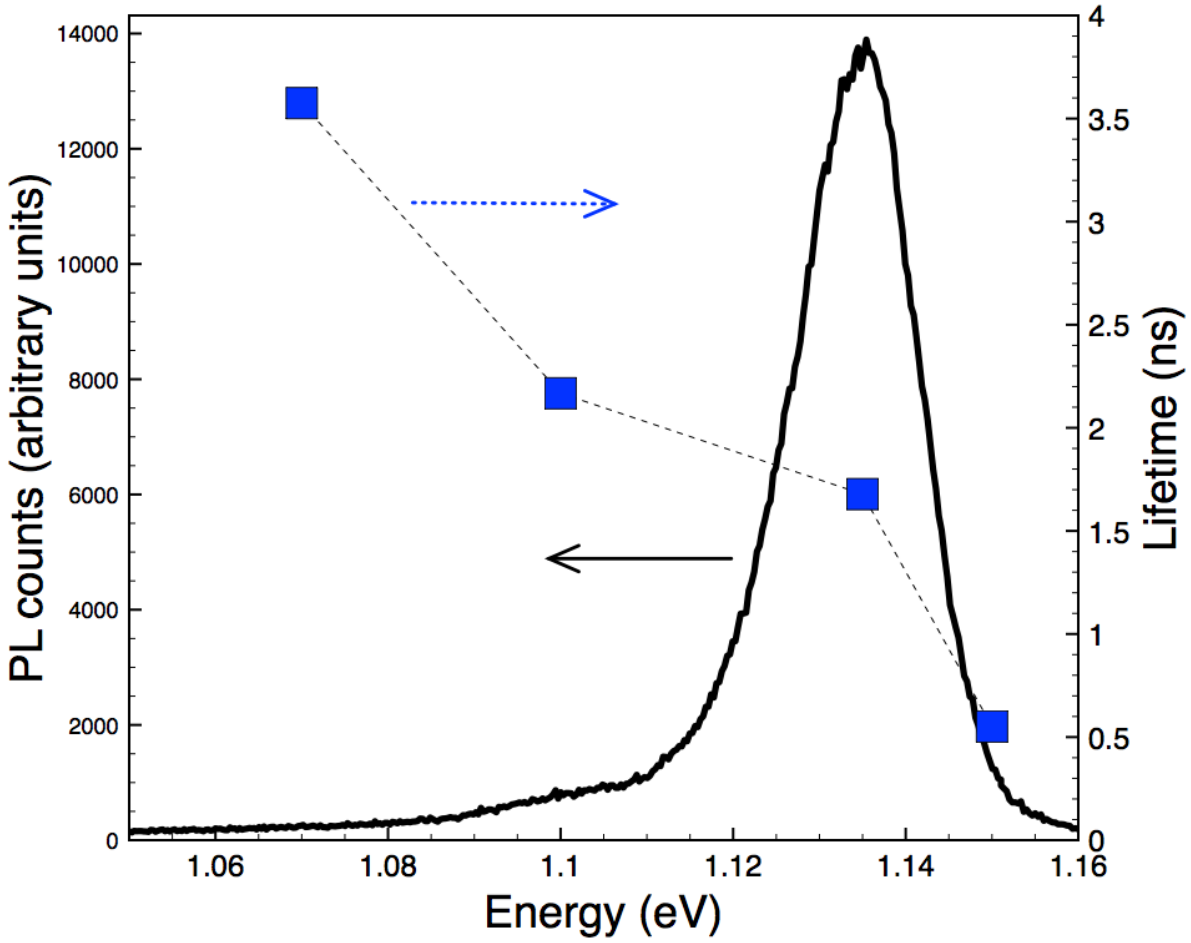


Figure 6.7: Dispersion of recombination lifetime with emission photon energy for sample N2761, measured at low temperature. It can be seen that the lifetime is enhanced at lower energies and shorter at higher energies, characteristic of recombination through localised states.

expected that there will be a difference in electron transport, and hence GaAsSbN device performance, depending on how much of the minority carrier transport occurs in n-type layers or p-type layers.

6.4 Conclusions

The steady-state and time-resolved photoluminescence of near 1 eV GaAsSbN has been discussed. It is found that there is low interface recombination at the GaAs/GaAsSbN interface. Bulk lifetimes of between 0.2 and 0.45 ns are measured, somewhat typical for dilute nitride materials. It was found that lifetime is affected by the use of dopants, being reduced by Si and slightly enhanced by Be. Several differences in the behavior of GaAsSbN are noted when using either n-type or p-type doping. In particular, the extent of carrier localization appears to be reduced by p-type doping. At room temperature the lifetimes are affected differently, with moderate p-type doping increasing lifetime and moderate n-type doping decreasing it. The effects of dopant polarity are also noted in device results.

Chapter 7

GaAsSbN 1 eV sub-cell characterisation

In this chapter results are presented for a GaAsSbN solar cell lattice-matched to GaAs with a design typical of other sub-cells in a conventional multi-junction stack. Optical and electrical characteristics of GaAsSbN devices are reported and a one-dimensional model of measured internal quantum efficiency is used to estimate minority electron diffusion lengths of around 500 nm. Improved device designs utilising a GaAs emitter layer are then demonstrated. Minority carrier diffusion lengths and junction properties are inferred from internal quantum efficiency and capacitance measurements respectively.

7.1 Basic sample designs

Devices were grown as described in Section 3.1. Full layer structures are found in Appendix A. The devices were fabricated using standard lithography and wet etch processing, with anti-reflection coating applied. Two device types were investigated with structures shown in Figure 7.1 and Figure 7.2:

- *np* with highly-doped GaAsSbN homojunction (N2627),

- *nip* with GaAs used as the emitter layer and un-doped GaAsSbN for the base layer (referred to as heterojunction sample later in the text) (N2623).

Nominal values for layer thickness and doping concentration are found in Table 7.1. Each device type had layers of the same thickness. The AlGaAs window layer is of composition $Al_{0.7}Ga_{0.3}As$. Not shown is a GaAs contact layer at the top of the device. This was etched to expose the active area between the metal contact fingers. The *np* device is the more conventional sub-cell structure in a MJSC, with current produced through minority carrier diffusion from a thick base layer to the narrow space-charge region. The heterojunction device may be expected to have lower voltage due to its lower doping and wider depletion width, but if minority carrier diffusion lengths are short, more current may be collected through using this design.

7.2 Proposed designs for improved short-circuit current

Due to the short minority carrier diffusion lengths present in dilute nitride materials, it is challenging to achieve sufficient current collection using a standard MJSC sub-cell design. Firstly, in the absence of sufficient diffusion collection, a wider depletion region is required for drift-aided collection of minority carriers. This is usually achieved through lowering the background doping level as much as possible. However, the electric field upon which such a device relies can be adjusted by using non-uniform material, doping or composition of emitter and base layers. This can be effectively achieved by altering the emitter design in strongly absorpting materials where most photons are absorbed towards the front of the device.

After investigating the two basic homojunction and heterojunction designs, several additonal cell designs were modeled and fabricated to investigate the effects of emitter design on short-circuit current of GaAsSbN sub-cells. They are shown in Table 7.2.

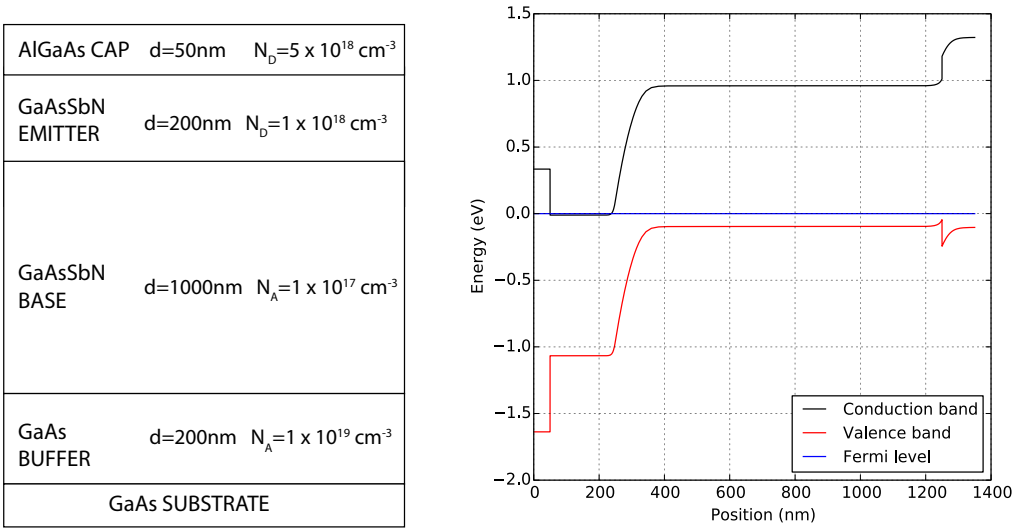


Figure 7.1: Schematic of the homojunction device design investigated in this study. (Left) Layer structure, with *np* configuration. (Right) Corresponding band structure. N_d/N_a is the donor/acceptor concentration, d is the layer thickness. The AlGaAs composition was 70% Al, 30% Ga.

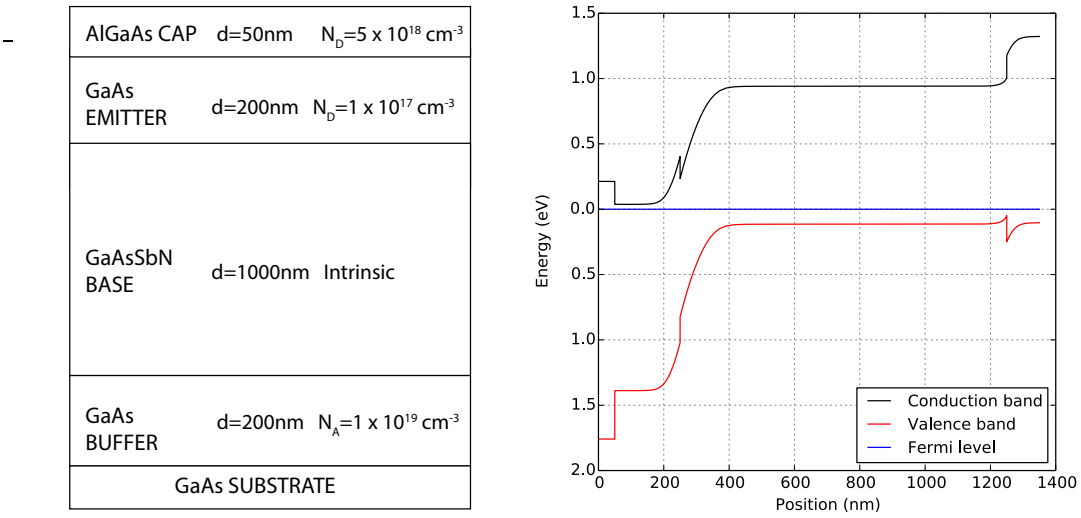


Figure 7.2: Schematic of the heterojunction device designs investigated in this study. (Left) Layer structure, with *np* configuration. (Right) Corresponding band structure. N_d/N_a is the donor/acceptor concentration, d is the layer thickness. The AlGaAs composition was 70% Al, 30% Ga.

Table 7.1: GaAsSbN device basic sample designs. All samples have 1000 nm GaAsSbN base. Full layer structures are found in Appendix A.

Label	Sample number	Emitter material & thickness (nm)	Emitter doping (cm^{-3})	Base doping cm^{-3}
Homojunction	N2627	GaAsSbN 200 nm	1×10^{18}	1×10^{18}
Heterojunction	N2623	GaAs 200 nm	1×10^{17}	Unintentional

Table 7.2: GaAsSbN device advanced sample designs. Emitter layers are listed from top to bottom. All samples have a base layer of 1000 nm thickness GaAsSbN. Full layer structures are found in Appendix A.

Sample number	Emitter material & thickness (nm)	Emitter doping (cm^{-3})	Base doping (cm^{-3})
N2772	GaAs 200 nm	1×10^{17}	Unintentional
N2773	GaAs 200 nm	1×10^{17}	1×10^{16}
N2774	GaAs 200 nm	1×10^{17}	1×10^{17}
N2776	GaAs 200 nm	1×10^{18} for 50 nm then 1×10^{17}	Unintentional
N2777	GaAs 100 nm then GaAsSbN 100 nm	1×10^{17}	1×10^{17}

An additional heterojunction cell identical in layer structure to N2623 was included as a control sample (N2772). The doping of the base was varied in samples N2773 and N2774 in order to investigate the effect on EQE and voltage of the sub-cell compared to unintentional doping. ARC was not applied to these cells. Full layer structures are found in Appendix A.

7.3 Experimental

Capacitance-voltage (CV) behaviour was measured at a frequency of 1 MHz, found to be sufficient to minimise the contribution of diffusion capacitance.

7.4 Results and discussion

7.4.1 Basic cell designs

DIV measurements are shown in Figure 7.3. Fitting the results to the ideal diode equation, it can be seen that the resistances in the devices differ, with lower shunt resistance for the homojunction device (R_{sh} = 3290/34400 Ω for homojunction/heterojunction). At high voltages the heterojunction structure shows greater series resistance (R_s = 0.02/0.18 Ω for homojunction/heterojunction). However, in the intermediate voltage range the devices show similar ideality factor of 1.43/1.5 for homojunction/heterojunction with 3.1/10.2 × 10^{-5} mA/cm^2 I_0 value. This ideality factor is indicative of trap-based recombination, similar to what has been observed in GaInNAs devices [84].

The LIV data for the two devices are shown in Figure 7.4. For the homojunction device, the short-circuit current density J_{SC} is 13.3 mA/cm^2, the open-circuit voltage V_{OC} is 0.48 V and the fill factor is 68.2%. The heterojunction device has increased J_{SC} of 24.3 mA/cm^2, V_{OC} of 0.47 V and the fill factor of 67.4%.

The V_{OC} of the devices is greater than that which would be provided by a germanium sub-cell (typically <0.25 V). EQE data, including three bias points for each sample, are shown in Figure 7.5. It can be seen from the EQE plots that the absorption edge of the samples differs slightly, which is attributed to fluctuating N composition between growths. However, this variation is < 0.01 eV. Taking the point at which the EQE drops below 1% as the bandgap gives 1.05 eV as the bandgap for both devices. However, both EQE measurements show a tail that decreases exponentially from this point towards 1 eV. The offset between open-circuit voltage and bandgap, considered proportional to the amount of non-radiative recombination in a device [85], is $E_g/q - V_{OC}$ = 0.57 and 0.58 V. This is comparable to the offset from cells of other dilute nitride materials [47]. The short-circuit current density necessary to match other sub-cell currents in a conventional triple-junction

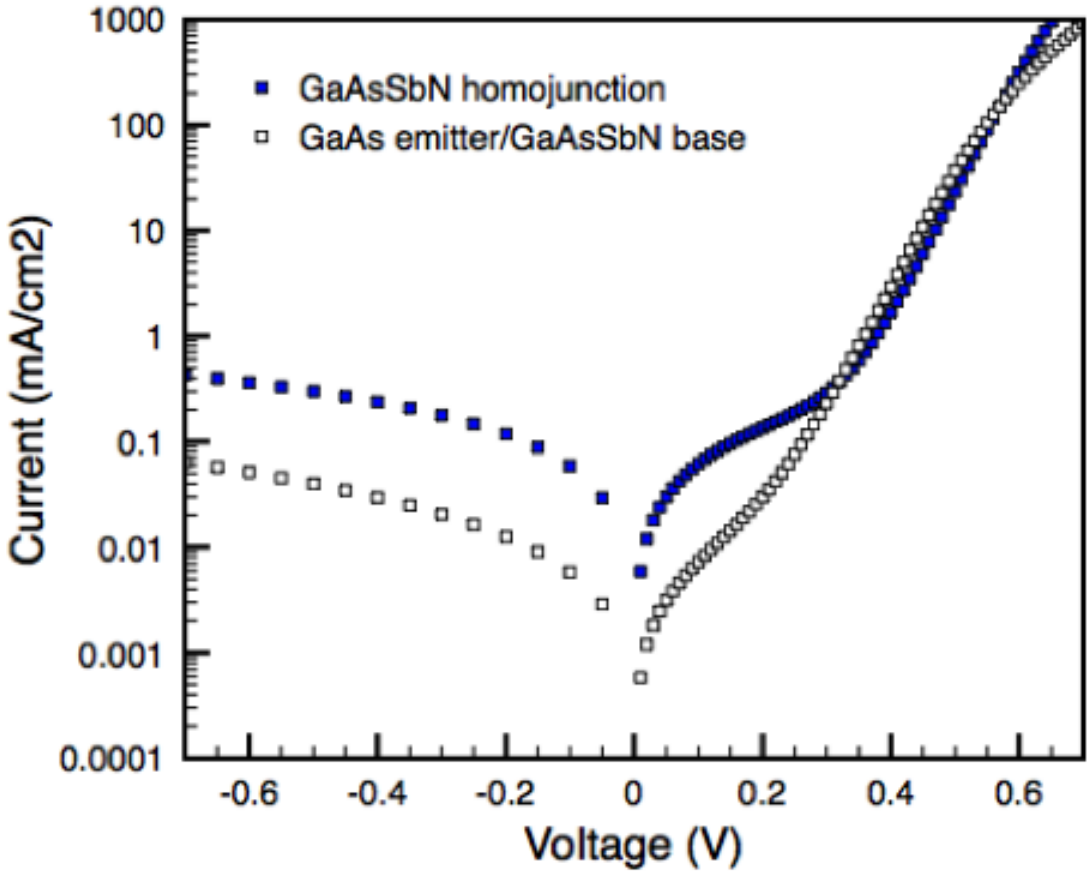


Figure 7.3: Current-voltage measurements in the dark for the two device designs. Blue filled squares represent the homojunction device N2627 with higher doping and open squares represent the heterojunction device N2623 with unintentionally doped GaAsSbN. The devices show similar ideality factor of 1.43/1.5 for homojunction/heterojunction. Both shunt resistance and series resistance are lower for the homojunction device.

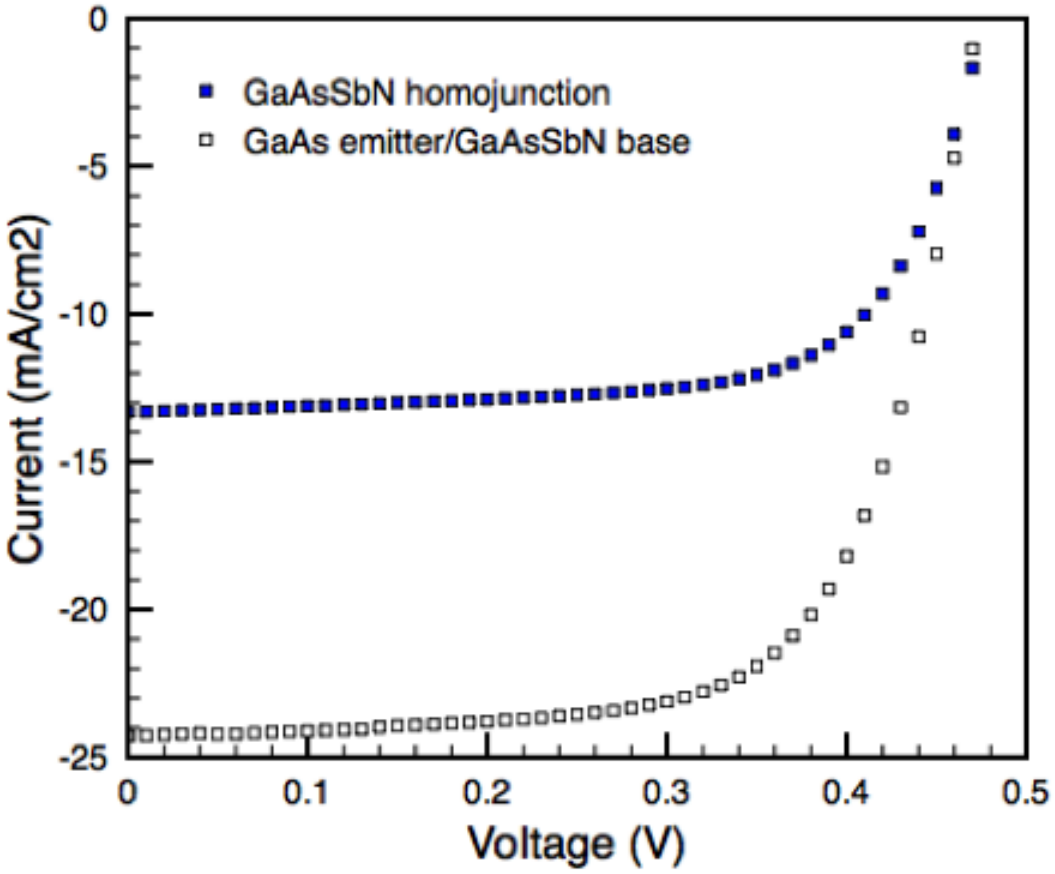


Figure 7.4: Current-voltage characteristic of the two devices under AM1.5G illumination. Blue filled squares represent the homojunction device N2627 with higher doping and open squares represent the heterojunction device with unintentionally doped GaAsSbN. It can be seen that the heterojunction device N2623 produces greater current. Short-circuit currents are 24.3 and 13.3 mA/cm^2. Open-circuit voltage/fill factor is 0.48V/68.2% and 0.47V/67.4% for homojunction and heterojunction respectively.

structure is 14 mA/cm^2, or 11 mA/cm^2 for a quad-junction. While these GaAsSbN cells approach that when under full illumination, to be useful in a triple-junction solar cell they must produce 14 mA/cm^2 when placed under the absorption profile of the top two cells, which will include a thick layer of GaAs. To calculate this, the EQE is multiplied by the AM1.5G spectrum and integrated from 870 nm to the bandgap. This gives the result of 4.5 and 6.8 mA/cm^2 for homojunction and heterojunction respectively. Thinning the middle cell would allow better current matching in a multi-junction structure. It is also worth pointing out that the antireflection coating used here is not particularly well matched to the absorption range of this material and assuming no reflection of incident photons, the $>$ 870 nm short-circuit currents are 1.38 times higher. In Figure 7.5 it can be seen that the quantum efficiency of the cell varies with applied bias in mid-range wavelengths. This corresponds to a changing of the depletion width of the device with bias - reverse bias increases the depletion width and carrier collection and forward decreases both attributes. The change in EQE with bias is less prominent at shorter and longer wavelengths as the carrier collection is limited by interface recombination at the front and back of the device. It can also be seen that the heterojunction device outperforms the homojunction device across all wavelengths, hence producing higher short-circuit current. One reason for this is likely to be that the carrier collection is somewhat dependent upon generation in the depletion region and the lower doped heterostructure sample has a wider depleted region. However, the transparency of the GaAs emitter to wavelengths longer than 870 nm also mitigates some of the poor performance observed in the homojunction cell.

Capacitance-voltage measurements were taken to investigate the junction properties of the devices. It was found that the homojunction device had a built-in voltage of 0.67V whereas that with the GaAs emitter had lower voltage of 0.61V. The increase is attributed to higher doping in the GaAsSbN homojunction sample. Figure 7.6 and Figure 7.7 show the C-V measurements for the two devices. The depletion width can be determined using:

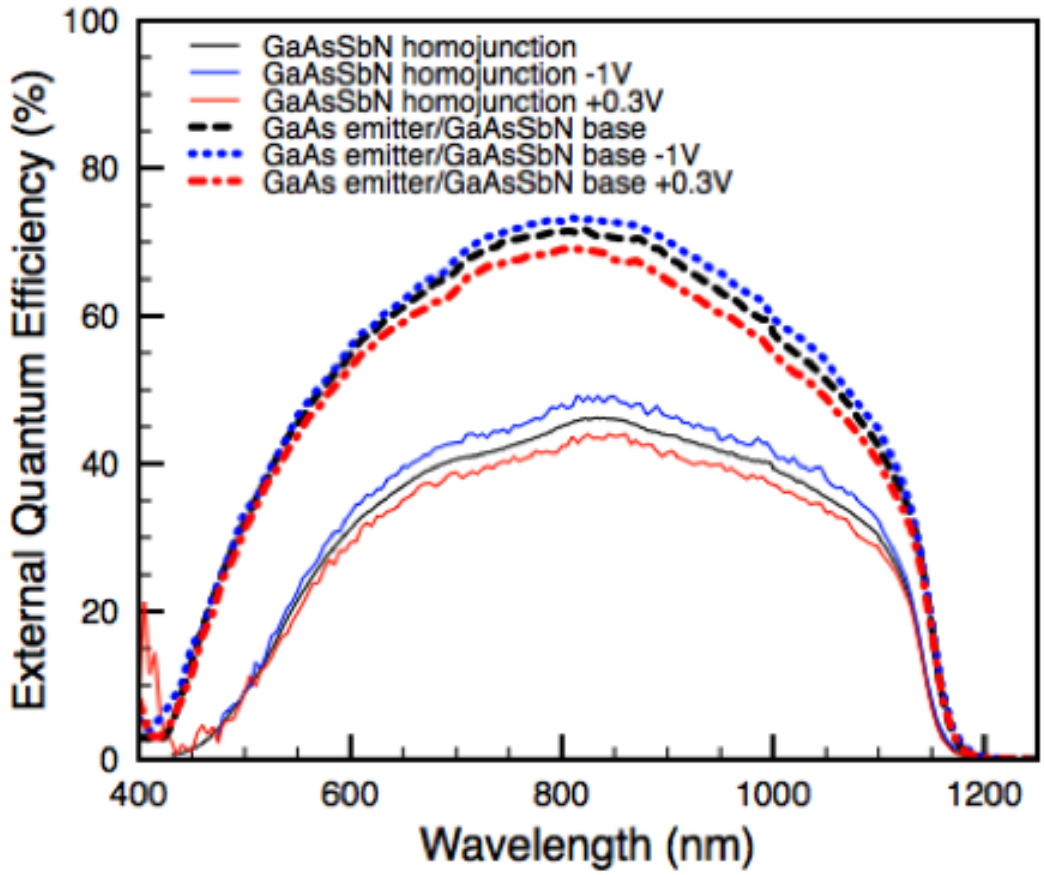


Figure 7.5: EQE of the two device designs reported. The heterojunction N2623 (dashed lines) device has a greatly enhanced compared to the homojunction N2627 (solid lines). Three bias points are displayed for each device, with the response at -1 V, 0 V and +0.3 V recorded. Enhancement or reduction of the EQE is seen with reverse and positive bias respectively. This is due to the changing width of the depleted region in the device. Response at longer wavelengths is lower partly due to use of non-optimal anti-reflection coating for this device.

$$W = \frac{\epsilon_r \epsilon_0 A}{C} \tag{7.1}$$

where ϵ_r is the relative permittivity of the material (assumed same as GaAs here), ϵ_0 is the permittivity of the vacuum and A is the area of the device. For the homojunction device the depletion width was found to be 97 nm. This is comparable to the depletion width calculation (using Eq. (2.30)) of 103 nm made by using the nominal doping value. The heterojunction device had depletion width of 345 nm due to its lower doping. The doping of the base layers was found to be 9.2×10^{16} cm^{-3} for homojunction and 8×10^{15} cm^{-3} for the heterojunction. As the base layer of the heterojunction was unintentionally doped, this is caused by background doping levels from impurities and defects.

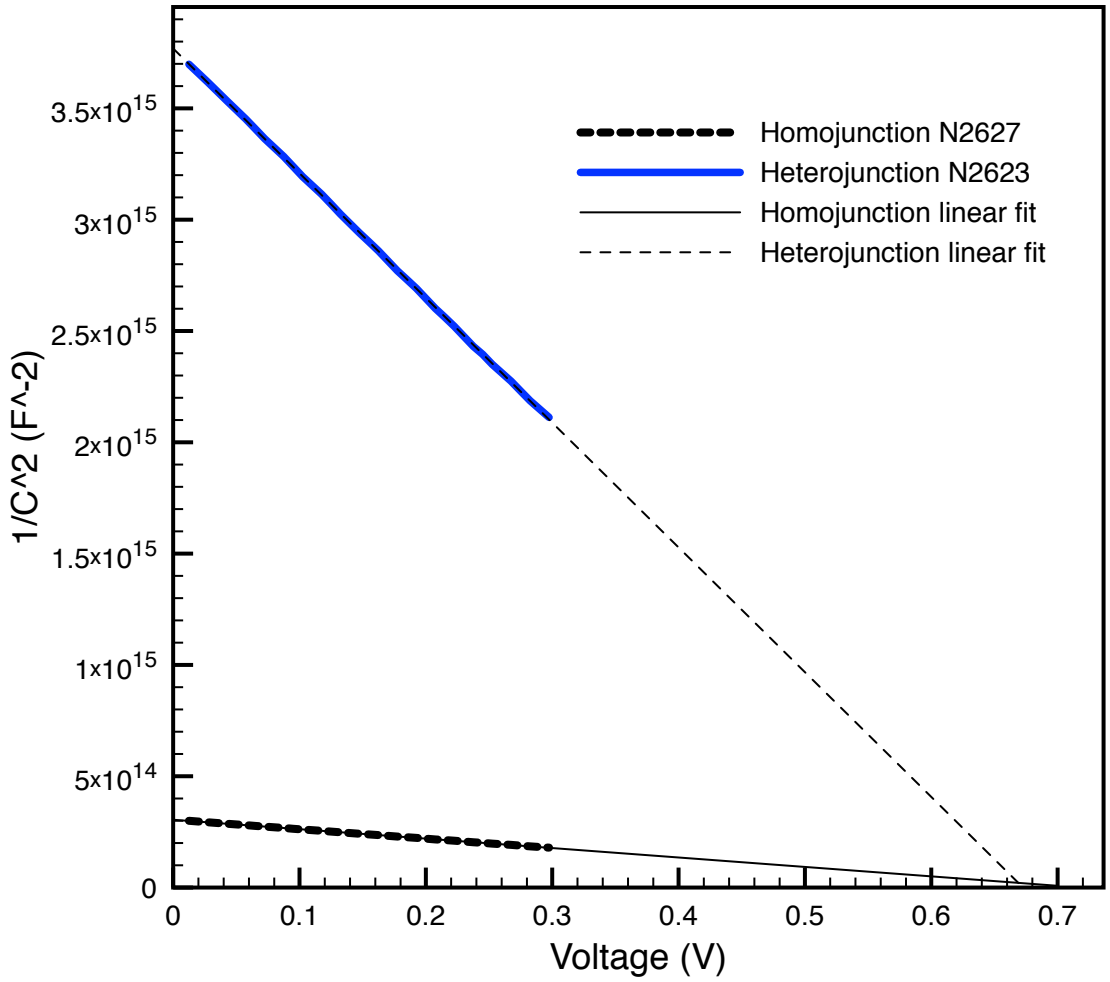


Figure 7.6: Capacitance-voltage data of the two devices. The linear fit is an extrapolation of the data in order to determine the built-in voltage from Eq. (3.4). It was found to be 0.61 V for the homojunction device and 0.67 V for the heterojunction device.

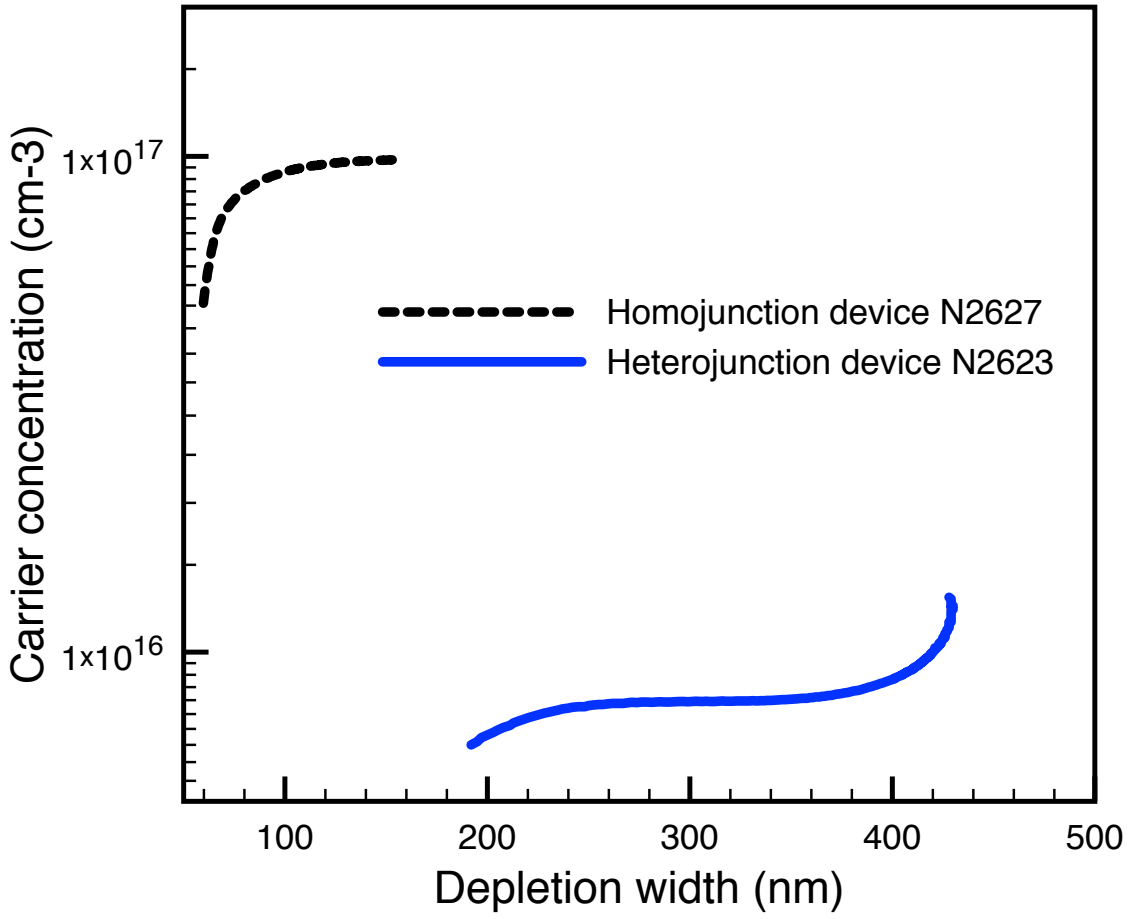


Figure 7.7: Carrier density as a function of junction depletion width as determined from the C-V measurement. It can be seen that the homojunction has achieved the nominal base doping. The heterojunction cell, unintentionally doped in the base, has a p-type background doping of around 8×10^{15} cm^{-3}, which can be considered as the ionised acceptor concentration of the nominally undoped GaAsSbN material.

7.4.2 Effect of dopant polarity on quantum efficiency

Two solar cells with 200 nm thick emitter and 1000 nm thick base layers were fabricated. For each cell every parameter was kept the same except the dopant polarity was switched, producing *pn* (N2264) and *np* (N2265) junctions samples with *p*-emitter and *n*-base or *n*-emitter and *p*-base, respectively. Full layer structures are found in Appendix A. Figure 7.8 shows the external quantum efficiency of these samples, along with the heterojunction sample N2623. It can be seen that the carrier collection is strongly affected by change in dopant polarity, with the wavelength axis acting as a measure of depth in the device. This results corresponds to the change in carrier lifetime with dopant polarity reported in the previous chapter. This difference between electron and hole transport in MBE-grown GaInNAs, particularly with use of Si as a dopant, has been noted by Kurtz et al. [48].

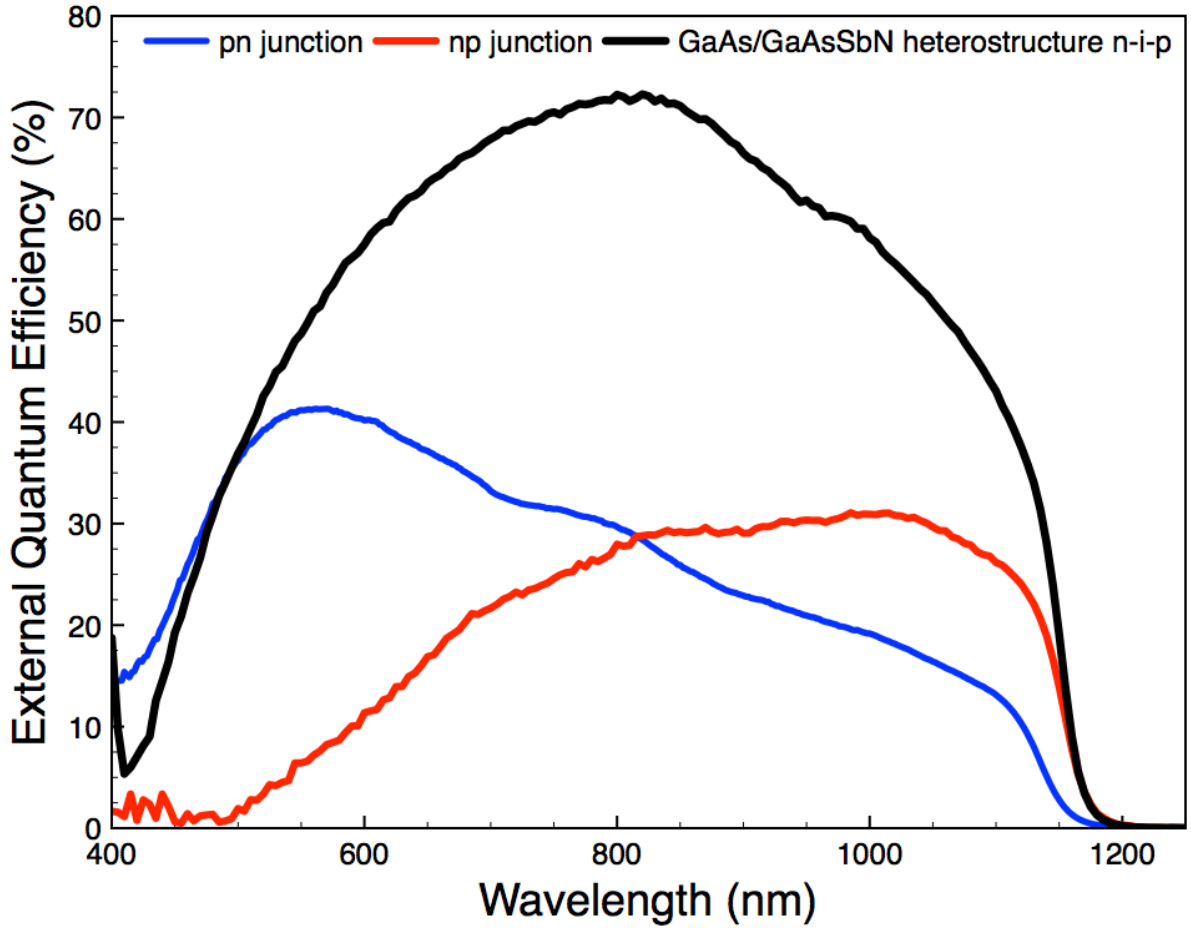


Figure 7.8: External quantum efficiency measurements for 3 solar cells. Comparing otherwise identical *np* and *pn* junctions (N2264 and N2265 respectively) shows the disparity in carrier transport between *n*-type doping and *p*-type doping. The higher performance of the N2623 heterojunction structure with GaAs *n*, *p* layers and GaAsSbN *i*-layer is also shown.

7.4.3 Modeling

By solving the drift-diffusion equations for minority carrier currents in a *pn* junction analytically [38] using the depletion approximation (see Section 2.3), the internal quantum efficiency (IQE) of the homojunction sample was calculated.

The device is modeled as a two-layer emitter/base structure, with an electrically inactive 50 nm AlGaAs optical filter. The absorption coefficient was measured in Chapter 5 using reflection and transmission measurements close to the band-edge and combined with n & k data obtained from spectroscopic ellipsometry at higher photon energies. The IQE model provides calculations of the relative contributions from the quasi-neutral emitter, quasi-neutral base and depletion regions. Perfect collection of carriers generated in the depletion region is assumed.

To fit the measurement, the diffusion length and surface recombination is varied systematically, changing the contributions from emitter and base. Additional contributions may occur due to the active material having lower energy band-gap than the substrate - wavelengths below the band-gap of GaAs may be transmitted through the substrate and reflected from the back contact. However, substrate free carrier absorption will absorb approximately 30% of the light per pass. The device is first modeled without this effect and then modeled assuming perfect reflection of unabsorbed long wavelength photons but including the free carrier absorption loss. The actual sample substrate is not polished on the reverse side so it is unlikely that perfect reflection actually occurs. Combining the possible effect of reflection with uncertainty on the relative contribution of emitter and base produces a range of acceptable fit values.

The result of the IQE fitting is shown in Figure 7.9. It can be seen that with this highly doped, narrow depletion region sample, most of the photocurrent is collected from the base of the material. The results show that an electron diffusion length of 575±175 nm is present in the base layer of the material (comparable to a calculated depletion width of 97 nm). This value is relatively high for dilute nitride material. A notable result is the fact that the contribution from the emitter is very low, with 30±10 nm hole diffusion length and high AlGaAs/GaAsSbN interface recombination velocity of 2×10^3 cm/s. The diffusion lengths also fit the IQE of the heterojunction cell, with the increase in IQE being attributable to the wider depletion region from the lower doping.

This interface recombination velocity is comparable to that determined in Chapter 6. This disparity between hole and electron diffusion lengths has also been reported for MBE-grown GaInNAs, with Kurtz et al. reporting [48] 30 nm and 500 nm for hole and electron diffusion lengths respectively. The poor emitter response has a severe effect on the quantum efficiency of the cell, with the front of the cell seeing strong absorption yet losing the generated carriers through ineffective carrier collection. The heterojunction sample, with a GaAs emitter, mitigates these losses even at wavelengths below the GaAs bandgap by moving the depth of carrier generation closer to the junction of the device. A thinner emitter layer for the homojunction design or an improved window layer may also improve the response in this way.

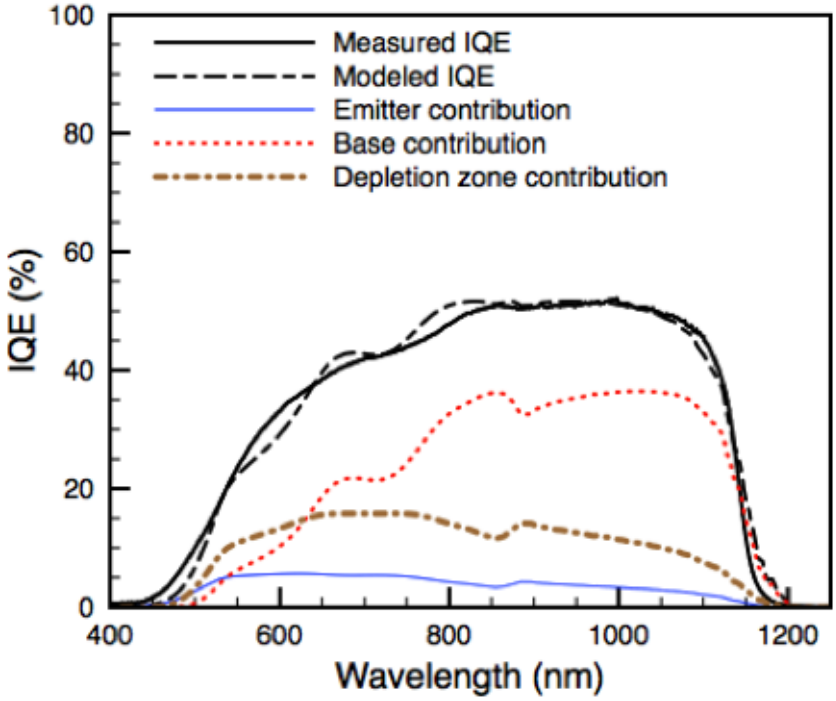


Figure 7.9: A comparison between measured IQE (solid lines) and a one-dimensional model (dashed lines) taking into account minority carrier diffusion and interface recombination. Perfect collection of carriers generated in the depletion region is assumed. The quasi-neutral parts of the emitter and base layers contribute according to their minority carrier diffusion and surface recombination. The values used in the above figure were front surface recombination velocity of 2×10^3 cm/s, emitter hole diffusion length of 30 nm, base electron diffusion length of 520 nm and negligible back surface recombination. In this particular calculation, full reflection of unabsorbed light from the back contact is assumed, setting a lower limit to the electron diffusion length.

7.4.4 Improved designs

7.4.5 Model

A conventional GaInP/(In)GaAs/Ge triple-junction cell has AM1.5G short-circuit current of at least 14 mA/cm^2. Highly efficient quad-junction cells should have short-circuit

currents > 11 mA/cm^2. The GaAsSbN sub-cells above, if they are to be integrated into a multi-junction solar cell, are lacking in short-circuit current and, to a lesser extent, voltage. However, it is also the case that the GaAs emitter design has improved the short-circuit current while retaining voltage. This is partly because of its higher bandgap than GaAsSbN ensuring longer wavelength photons are absorbed closer to the junction. Several designs were fabricated to try to take advantage of this. Note that ARC was not applied to these cells and so I_{SC} and EQE are not directly comparable with the two basic designs.

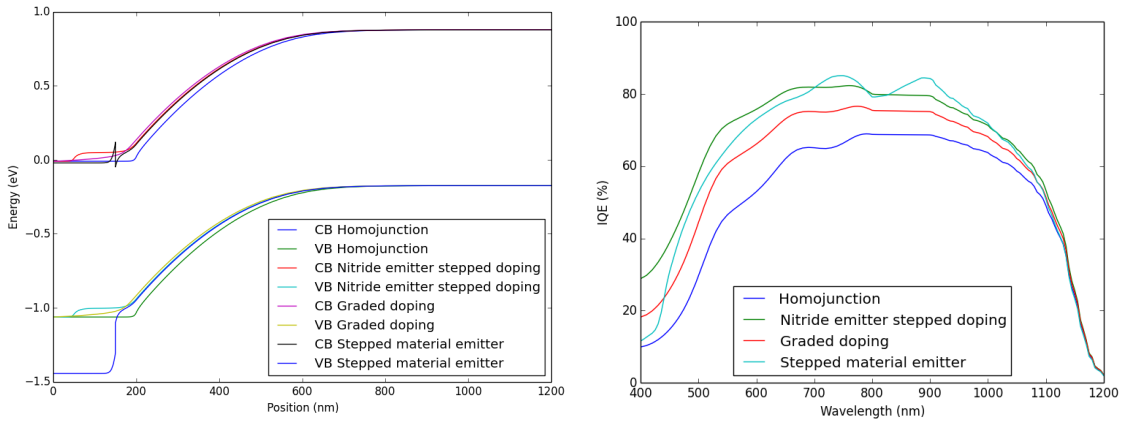


Figure 7.10: Comparison of different emitter design devices. (Left) shows the calculated band profile at short-circuit for each design. It can be seen that changing the design of the emitter changes the slope of the bands near the front of the device. This is reflected in different EQE response (right). Through this mechanism, the response of GaAsSbN at different wavelengths can be altered, increasing short-cicuit current in desirable regions for a MJSC.

Figure 7.10 shows the results of drift-diffusion modeling of different emitter designs. The band offset between GaAs/GaAsSbN was estimated using the band offset of GaAs/GaAsSb [86] for 8.5% Sb content, with the remaining offset assumed to be in the conduction band

due to N. The homojunction sample is that of N2627. 'Graded doping' is a similar design to N2776 but with a more gradual doping change from 1×10^{18} cm^{-3} to 1×10^{16} cm^{-3} rather than a step change. The nitride emitter stepped doping sample has the stepped doping profile of N2776 but with emitter of GaAsSbN rather than GaAs. This design was not fabricated but may be expected to increase the emitter contribution considering the results found for variation of minority carrier diffusion length and lifetime with doping in Section 7.4.3 and Section 6.3.2. The 'stepped material emitter' sample is similar to N2777. Integrating the calculated IQE with the AM1.5G spectrum to get short-circuit current at wavelengths > 870 nm, the following values were found:

Table 7.3: Improved device design simulated J_{SC} at > 870 nm

Label	J_{SC} (mA/cm^2)
Homojunction	7.46
Nitride emitter stepped doping	8.36
Graded doping	7.99
Stepped material emitter	8.44

It can be seen that the emitter design can affect the response at wavelengths greater than 870 nm by as much as 1 mA/cm^2.

7.4.6 Experiment

The results for the designs described in Section 6.3.2 are shown below. Figure 7.11 shows the DIV for the 5 designs whereas Table 7.4 shows the LIV parameters. It can be seen that the DIV varies between devices indicating that the recombination of the cells is being changed by the emitter design. From the LIV parameters and the EQE shown in Figure 7.12 it can be seen that there is variation between the designs. The effect of variation of doping with N2772, N2773 and N2774 can be clearly seen and corresponds with the observed trend of minority carrier lifetime with doping of Chapter 6. N2773, which

is lightly p-doped, shows increased J_{SC} and long-wavelength EQE, indicating increased recombination length. Increasing the doping further in PV3 reduces these parameters. This is comparable to the lifetime results found in Chapter 6 Figure 6.4. N2777 shows enhanced EQE in the desirable wavelength for multi-junction applications. However, the overall integrated J_{SC} at wavelengths >870 nm does not vary between samples as it does in the simulation shown in Figure 7.10.

Table 7.4: GaAsSbN improved device designs LIV results under AM1.5G unfiltered spectrum

Description	Sample number	J_{SC} (mA/cm^2)	V_{OC} (V)	FF (%)
Heterojunction	N2772	14.5	0.44	59.5
Lightly doped base heterojunction	N2773	15.9	0.43	71.0
Increased doping base heterojunction	N2774	13.3	0.32	67.1
Stepped doping emitter	N2776	15.0	0.45	71.0
Stepped material emitter	N2777	16.0	0.46	66.1

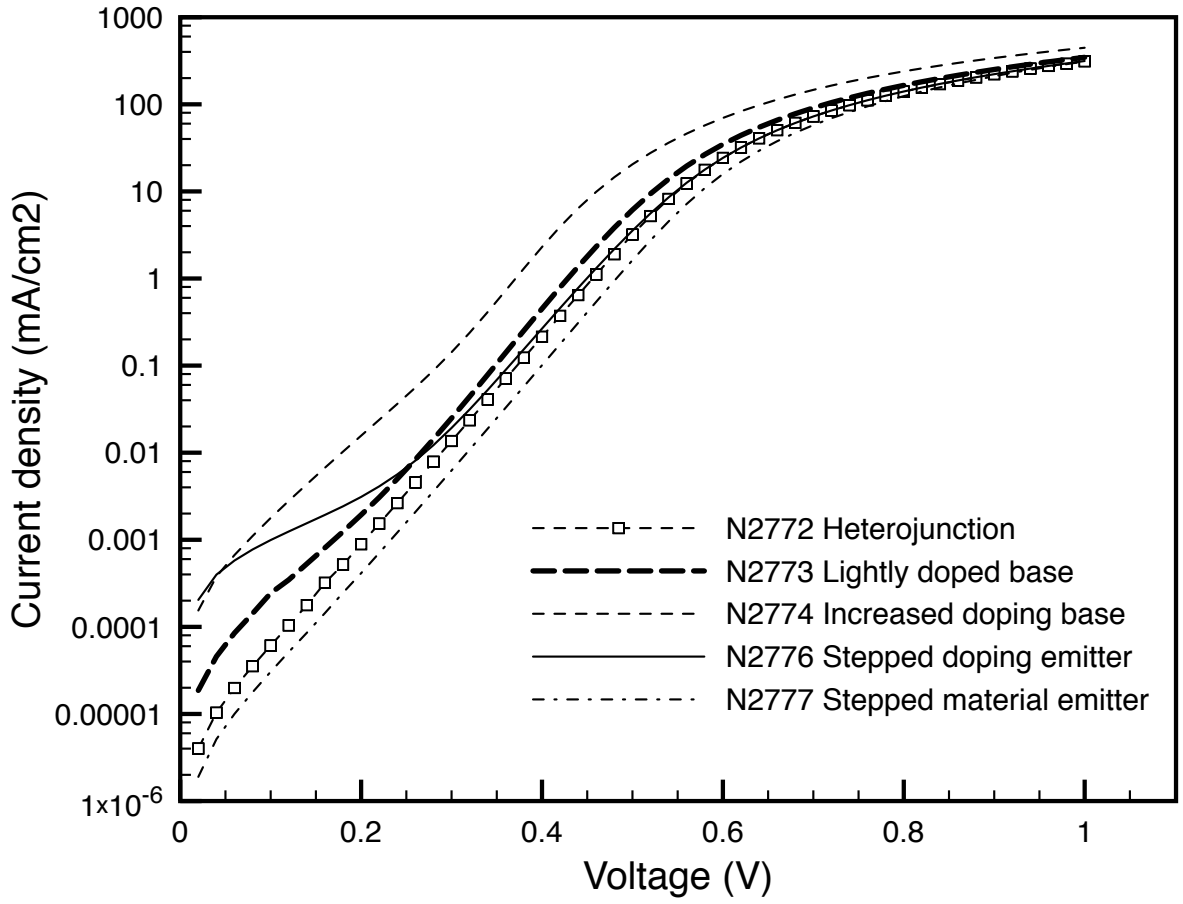


Figure 7.11: DIV of different emitter designs. N2767 displays lower dark current and correspondingly higher open-circuit voltage.

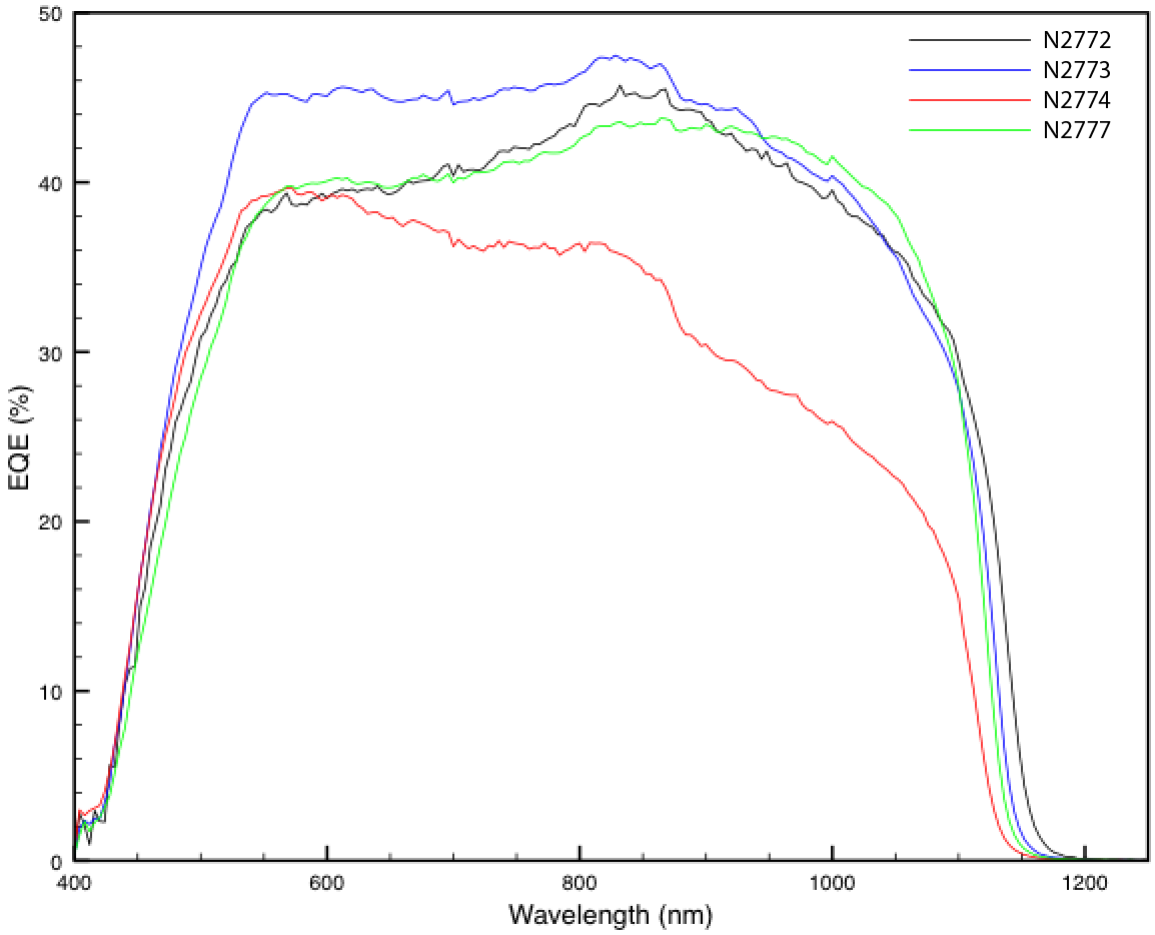


Figure 7.12: EQE of the improved emitter device designs. No device had ARC applied. The difference in doping with N2772, N2773 and N2774 can be clearly seen. N2777 shows enhanced EQE in the desirable wavelength for multi-junction applications. However, integrated current values were the same.

7.4.7 Limits to GaAsSbN sub-cell performance

Having determined the properties of 1 eV sub-cells, including macroscopic properties of J_{SC} and V_{OC}, and microscopic properties of background doping concentration and minortiy carrier diffusion length, it is possible to establish limits to the performance of GaAsSbN solar cells by modeling cell designs. It is also possible to predict the necessary improvements required for this material to be feasible for use in MJSCs. Three aspects are considered in this section:

- possible improvements to the current sub-cell,
- modeling the integration of the current sub-cell into a MJSC,
- modeling the effect of sub-cell improvements on MJSC efficiency.

The current homojunction sub-cell is limited by minority carrier recombination in the bulk and front surface. If improved sufficiently, to $\gg$ 1 μm, it would create a maximum possible short-circuit current of 10.2 mA/cm^2 below the bandgap of GaAs, becoming limited by the thickness. An optically thick 1.05 eV cell that collects all generated photons and has perfect ARC would be able to produce 12.4 mA/cm^2 below the bandgap of GaAs. If integrated into a standard 1.9/1.4/0.66 eV solar cell as a fourth junction to make a 1.9/1.4/1.05/0.66 eV cell, operating at 1000X concentration with realistic extrinsic losses, the current sub-cell would give an efficiency of 34.6% . Additional optimisation of sub-cell thicknesses by thinning the cells above could give 38.9% efficiency at 1000 suns. It is therefore clear that improvement of the current GaAsSbN sub-cell is necessary as well as considering the overall MJSC design to enhance the current of this sub-cell. The *nip* sub-cell with higher photocurrent will likely be essential. Lowering the bandgap of the sub-cell or accounting for radiative coupling effects as in Chapter 4 will also allow the GaAsSbN sub-cell to produce more current, at the expense of open-circuit voltage in the first case.

Taking the optimal thickness case, the quad-junction efficiency can be mapped as a function of both GaAsSbN base diffusion length and background doping (each doping giving a particular depletion width). This allows for GaAsSbN sub-cell targets to be identified. Figure 7.13 shows attainable short-circuit current for the *nip* GaAsSbN sub-cell as a function of both background doping and base electron diffusion length.

Due to the series-connected nature of the sub-cells, it is found that the GaAsSbN sub-cell voltage has a comparatively minor effect on the overall MJSC efficiency due to the cell being a lower sub-cell and contributing a small part of the overall voltage. Comparatively, achieving the sub-cell J_{SC} to current-match the whole device is a higher priority, as due to the current matching constraint, efficiency quickly reduces with a reduction in GaAsSbN sub-cell current. This indicates an *nip* sub-cell with lowered voltage and higher current would be preferable to a higher voltage, lower current *np* sub-cell.

Figure 7.14 shows the predicted 4J efficiency as a function of background doping and minority carrier diffusion length. It can be seen that although high efficiencies can be reached, additional current is required through improvement either of diffusion length or background doping. Radiative coupling, ARC design and lowering the band gap of GaAsSbN may also increase the short-circuit current of this sub-cell, lowering the requirements of diffusion length and background doping.

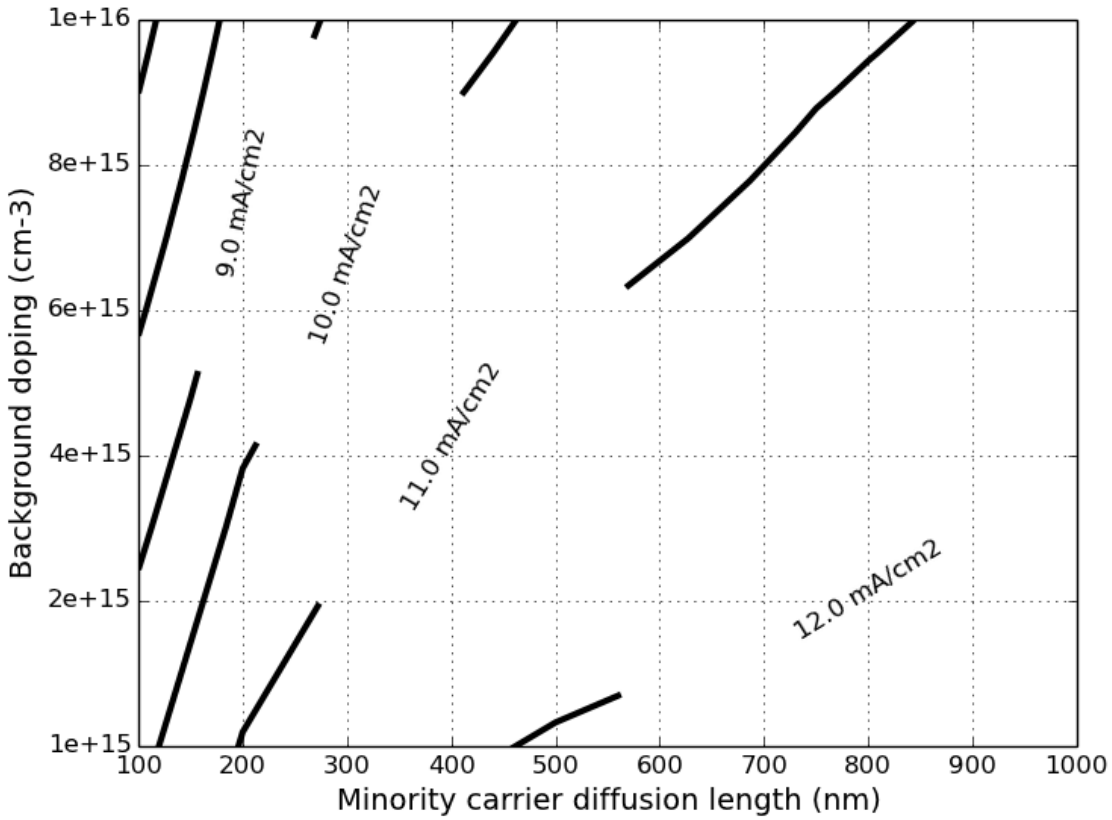


Figure 7.13: Overall MJSC short-circuit current as a function of the minority carrier diffusion length and background doping of the *nip* GaAsSbN sub-cell. Current diffusion length is estimated to be 500 nm with 8×10^{15} cm^{-3} background doping.

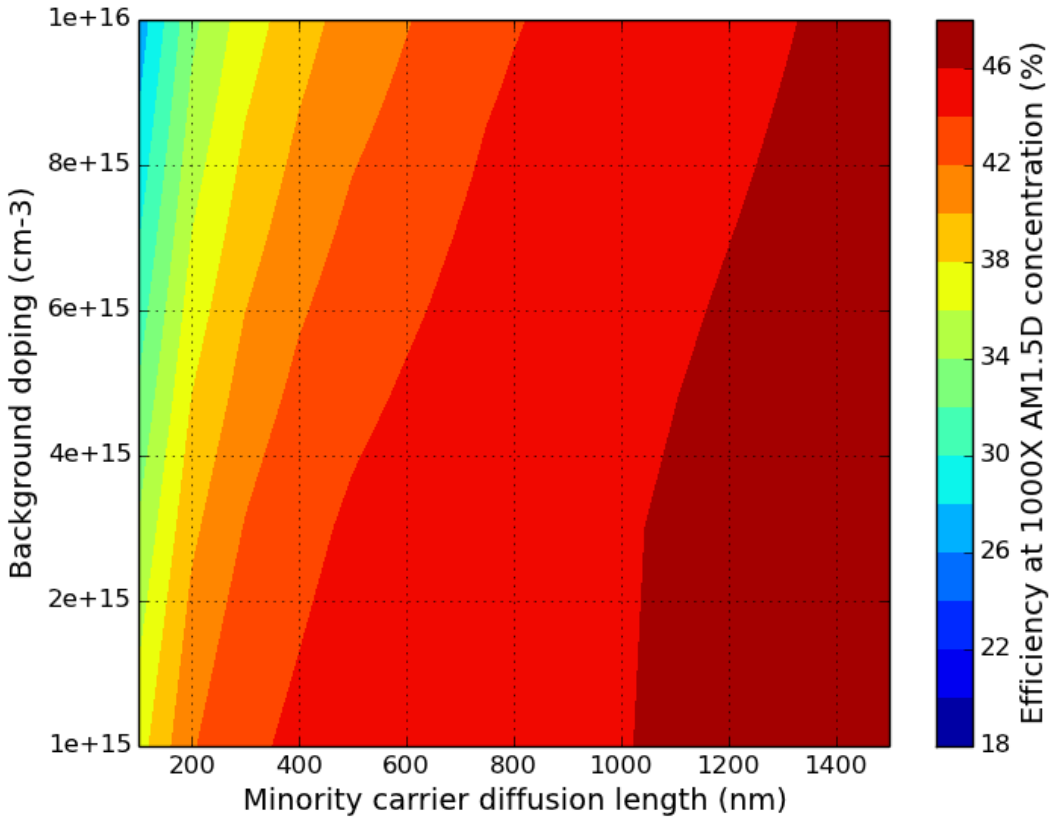


Figure 7.14: Overall MJSC efficiency as a function of the minority carrier diffusion length and background doping of the *nip* GaAsSbN sub-cell. Current diffusion length is estimated to be 500 nm with 8×10^{15} cm^{-3} background doping.

7.5 Conclusions

1 eV bandgap GaAsSbN photovoltaic devices were demonstrated - a standard homojunction device and heterojunction devices with GaAs emitter. Open-circuit voltages of 0.48 and 0.47 V were measured and are a suitable value for the intended application as a sub-cell in multi-junction solar cells. Evidence for minority electron diffusion lengths of 575 $\pm$ 175 μm has been shown through fitting a quantum efficiency model to measurement of a homojunction design. In comparison hole diffusion was an order of magnitude lower. A conventional homojunction sub-cell design produces 4.5 mA/cm^2 at wavelengths longer than 870 nm - insufficient current generation to match conventional multi-junction solar cells. This is partly due to poor emitter performance and front interface recombination. Using GaAs as the emitter material along with lower doping concentrations gave improved short-circuit current of 6.8 mA/cm^2 (for wavelengths >870 nm) while retaining similar open-circuit voltage and fill factor. Improvements in minority carrier diffusion and wider depletion region are likely to be required to meet the target of 14 mA/cm^2 for use in a triple-junction solar cell and 12 mA/cm^2 in a quad-junction solar cell. It was shown that the short-circuit current can be increased for particular wavelengths different by careful design of the device layers, such as graded doping or material composition. Target sub-cell parameters were identified that would allow GaAsSbN to contribute to a high efficiency, lattice-matched quad-junction cell.

Chapter 8

Summary and further work

In order to achieve a highly efficient solar cell, the present industry standard of GaInP/GaAs/Ge will be augmented with a 1 eV material. The dilute nitride material GaAsSbN can provide absorption thresholds of 1.4 eV to 0.9 eV while remaining lattice-matched to Ge.

Radiative coupling calculations suggest that a 1.15 eV sub-cell could replace the 1 eV sub-cell and still achieve high efficiencies in a CPV MJSC. This has not been previously identified in optimal bandgap calculations but is a result of the inclusion of radiative coupling in the optimisation of the cell. The 1.15 eV bandgap could be achieved with less N content than a 1 eV cell which may prove advantageous for minority carrier transport in a dilute nitride alloy. The realistic limiting efficiency of triple-junction structures by considering their extrinsic losses is found to be $< 50\%$. It is found that even with similar losses, a quad-junction MJSC can reach 50% efficiency. The spectral sensitivity of MJSCs with radiative coupling was also investigated and it was found that radiative coupling helps to mitigate spectral sensitivity in MJSCs with non-optimal (but technologically feasible) bandgaps.

The absorption properties of GaAsSbN were measured and modeled. Electroreflectance is used to determine transitions within the material. The result shows that the absorption coefficient of the material can be reproduced using a model dielectric function combined

with parameters extracted from electroreflectance. As far as the author is aware, this is the first time such a model has been developed for GaAsSbN.

The carrier dynamics of GaAsSbN were studied by photoluminescence and time-resolved photoluminescence. The results of temperature dependent photoluminescence show that GaAsSbN exhibits carrier localisation effects, visible in deviation from the Varshni behaviour of bandgap change with temperature. The measured TRPL decays were fitted using a free-carrier recombination model to extract the recombination coefficients. This analysis shows that the material is dominated by non-radiative recombination. Recombination between GaAs/GaAsSbN interfaces was negligible but high surface recombination is present at AlGaAs/GaAsSbN interfaces. A bulk lifetime of 0.4 ns was obtained. This lifetime varied with the doping of the material, with n-type material exhibiting reduced lifetime and p-type material exhibiting enhanced lifetime compared to the intrinsic material.

GaAsSbN solar cell design is discussed and modeled and verified through experimental measurements. The IQE is modeled using analytical versions of the drift-diffusion equations along with experimental inputs. Minority carrier diffusion for electrons is found to be 500 nm whereas for holes it is 30 nm. Both of these limit the response of the devices. Interface recombination limits the response at the short wavelengths. The findings are consistent with the carrier dynamics findings. Improvement in certain wavelength ranges, including that below the GaAs bandgap, is possible through control of the emitter design.

Overall, GaAsSbN is a promising material for MJSCs but due to insufficient current generation will not yet realise a high efficiency solar cell in the way that the comparable material GaInAsSbN has. GaInAsSbN has been successfully implemented in solar cells due to the discovery of a narrow window of growth parameters and careful consideration of the overall MJSC design. Understanding the advantages and limitations to GaAsSbN will inform future development of the alloy.

To further improve GaAsSbN sub-cells for MJSCs, further information on the absorp-

tion coefficient would be useful. More detailed knowledge of the effect of nitrogen on the bandgap and recombination would be desirable: the nature of the induced disorder and study of the localisation using magneto-photoluminescence could be beneficial. Investigation of electronic defect types using temperature dependent DIV or capacitance techniques could lead to improvement in material quality. In general, compositional dependence of the alloy properties would enable improved design of an overall MJSC structure by allowing the possibility to optimise the trade-off between nitrogen-induced bandgap reduction and nitrogen-induced minority carrier recombination. Combined with tailored design of the overall MJSC, this may allow GaAsSbN to produce a useful sub-cell for high efficiency concentrator photovoltaic devices.

References

[1] William Shockley and Hans J Queisser. Detailed Balance Limit of Efficiency of p-n Junction Solar Cells. *Journal of Applied Physics*, 32(3):510, 1961.

[2] D J Farrell and N J Ekins-Daukes. Routes to High-efficiency Photovoltaic Conversion of Solar Energy. *Solar Energy, Modern Energy Review, Vol:3*, February 2011.

[3] Martin A. Green, Keith Emery, Yoshihiro Hishikawa, Wilhelm Warta, and Ewan D. Dunlop. Solar cell efficiency tables (version 45). *Progress in Photovoltaics: Research and Applications*, 23(1):1–9, 2015.

[4] Louise C Hirst and Nicholas J Ekins-Daukes. Fundamental losses in solar cells. *Progress in Photovoltaics: Research and Applications*, 19(3):286–293, August 2010.

[5] Ngai Lam Alvin Chan, Helen E Brindley, and Nicholas John Ekins-Daukes. Impact of individual atmospheric parameters on CPV system power, energy yield and cost of energy. *Progress in Photovoltaics: Research and Applications*, pages n/a–n/a, May 2013.

[6] Martin A. Green, Keith Emery, Yoshihiro Hishikawa, Wilhelm Warta, and Ewan D. Dunlop. Solar cell efficiency tables (version 42). *Progress in Photovoltaics: Research and Applications*, 21(5):827–837, 2013.

[7] A De Vos. Detailed balance limit of the efficiency of tandem solar cells. *Journal of Physics D: Applied Physics*, 13:839–846, 1980.

[8] AzurSpace GmbH. 3c44 concentrator triple junction solar cell data sheet, 2016. [Online; accessed 14-September-2016].

[9] Spectrolab Inc. C3p5 39.5 point focus solar cells data sheet, 2016. [Online; accessed 14-September-2016].

[10] Antonio Luque. Will we exceed 50% efficiency in photovoltaics? *Journal of Applied Physics*, 110(3):031301, 2011.

[11] Richard M Swanson. The promise of concentrators. *Progress in Photovoltaics: Research and Applications*, 8(1):93–111, 2000.

[12] Ngai Lam Alvin Chan, Tomos Thomas, Markus Führer, and Nicholas J Ekins-Daukes. Practical limits of multijunction solar cell performance enhancement from radiative coupling considering realistic spectral conditions. *IEEE Journal of Photovoltaics*, 4(5):1306–1313, 2014.

[13] J F Geisz, M A Steiner, I García, S R Kurtz, and D J Friedman. Enhanced external radiative efficiency for 20.8single-junction GaInP solar cells. *Applied Physics Letters*, 103(4):041118, 2013.

[14] T Wilson, T Thomas, M Führer, and NJ Ekins-Daukes. Addressing reflectivity losses in multi-junction solar cells to achieve 50% power conversion efficiency. *Materials Research Innovations*, 19(7):503–507, 2015.

[15] Daniel J Aiken. High performance anti-reflection coatings for broadband multi-junction solar cells. *Solar Energy Materials and Solar Cells*, 64(4):393–404, 2000.

[16] Marc Steiner, Simon P Philipps, Martin Hermle, Andreas W Bett, and Frank Dimroth. Validated front contact grid simulation for GaAs solar cells under concentrated sunlight. *Progress in Photovoltaics: Research and Applications*, 19(1):73–83, December 2010.

[17] Galiana and Algora. Comparison of 1D and 3D analysis of the front contact influence on GaAs concentrator solar cell performance. *Solar Energy Materials and Solar Cells*, 90(16):16–16, October 2006.

[18] I Vurgaftman, J R Meyer, and L R Ram-Mohan. Band parameters for III–V compound semiconductors and their alloys. *Journal of Applied Physics*, 89(11):5815, 2001.

[19] Vijit Sabnis, Homan Yuen, and Mike Wiemer. High-efficiency multijunction solar cells employing dilute nitrides. In *8th International Conference On Concentrating Photovoltaic Systems: CPV-8*, pages 14–19. AIP, 2012.

[20] T Thomas, A Mellor, NP Hylton, D Alonso, A Braun, NJ Ekins-Daukes, JPR David, SJ Sweeney, et al. Requirements for a gaasbi 1 ev sub-cell in a gaas-based multijunction solar cell. *Semiconductor Science and Technology*, 30(9):094010, 2015.

[21] R. Roucka, A. Clark, T. Wilson, T. Thomas, M. Fhrer, N. Ekins-Daukes, A. Johnson, R. Hoffman, and D. Begarney. Demonstrating dilute-tin alloy sigesn for use in multijunction photovoltaics: Single- and multijunction solar cells with a 1.0-ev sigesn junction. *IEEE Journal of Photovoltaics*, 6(4):1025–1030, July 2016.

[22] W Guter, R Kern, W Köstler, T Kubera, R Löckenhoff, M Meusel, M Shirnow, and G Strobl. III-V Multijunction Solar Cells—New Lattice-Matched Products And Development Of Upright Metamorphic 3J Cells. *AIP Conference Proceedings*, 1407:5, 2011.

[23] T. Takamoto, T. Agui, A. Yoshida, K. Nakaido, H. Juso, K. Sasaki, K. Nakamora, H. Yamaguchi, T. Kodama, H. Washio, M. Imaizumi, and M. Takahashi. World's highest efficiency triple-junction solar cells fabricated by inverted layers transfer process. In *Photovoltaic Specialists Conference (PVSC), 2010 35th IEEE*, pages 000412–000417, June 2010.

[24] Ryan M France, John F Geisz, Iván García, Myles A Steiner, William E McMahon, Daniel J Friedman, Tom E Moriarty, Carl Osterwald, J Scott Ward, Anna Duda, et al. Quadruple-junction inverted metamorphic concentrator devices. *IEEE Journal of Photovoltaics*, 5(1):432–437, 2015.

[25] Frank Dimroth, Matthias Grave, Paul Beutel, Ulrich Fiedeler, Christian Karcher, Thomas N D Tibbits, Eduard Oliva, Gerald Siefer, Michael Schachtner, Alexander Wekkeli, Andreas W Bett, Rainer Krause, Matteo Piccin, Nicolas Blanc, Charlotte Drazek, Eric Guiot, Bruno Ghyselen, Thierry Salvetat, Aurélie Tauzin, Thomas Signamarcheix, Anja Dobrich, Thomas Hannappel, and Klaus Schwarzburg. Wafer bonded four-junction GaInP/GaAs//GaInAsP/GaInAs concentrator solar cells with 44.7 *Progress in Photovoltaics: Research and Applications*, 22(3):277–282, January 2014.

[26] J S Blakemore. Semiconducting and other major properties of gallium arsenide. *Journal of Applied Physics*, 53(10):R123, 1982.

[27] Sadao Adachi. Model dielectric constants of gap, gaas, gasb, inp, inas, and insb. *Physical review B*, 35(14):7454, 1987.

[28] M C DeLong, D J Mowbray, R A Hogg, M S Skolnick, M Hopkinson, J P R David, P C Taylor, Sarah R Kurtz, and J M Olson. Photoluminescence, photoluminescence excitation, and resonant Raman spectroscopy of disordered and ordered Ga0.52In0.48P. *Journal of Applied Physics*, 73(10):5163, 1993.

[29] Uwe Rau. Reciprocity relation between photovoltaic quantum efficiency and electroluminescent emission of solar cells. *Physical Review B*, 76(8):085303, August 2007.

[30] Manuel Cardona and Y Yu Peter. *Fundamentals of semiconductors*. Springer, 2005.

[31] Sadao Adachi. Optical dispersion relations for GaP, GaAs, GaSb, InP, InAs, InSb, AlxGa1xAs, and In1xGaxAsyP1y. *Journal of Applied Physics*, 66(12):6030, 1989.

[32] Sopra SA. Optical database. [Online; accessed 14-September-2016].

[33] P Wurfel. The chemical potential of radiation. *Journal of Physics C: Solid State Physics*, 15(1):3967–3985, June 1982.

[34] W Shockley and W T Read. Statistics of the Recombinations of Holes and Electrons. *Physical Review*, 87(5):835–842, September 1952.

[35] R N Hall. Electron-Hole Recombination in Germanium. *Physical Review*, 87(2):387–387, July 1952.

[36] David Ferry. *Semiconductor transport*. CRC Press, 2000.

[37] Diego Alonso-Álvarez, Markus Führer, Tomos Thomas, and Ned Ekins-Daukes. Elements of modelling and design of multi-quantum well solar cells. In *2014 IEEE 40th Photovoltaic Specialist Conference (PVSC)*, pages 2865–2870. IEEE, 2014.

[38] J Nelson. *The Physics of Solar Cells*, volume 1. World Scientific, January 2003.

[39] C H Henry. Limiting efficiencies of ideal single and multiple energy gap terrestrial solar cells. *Journal of Applied Physics*, 51(8):4494, 1980.

[40] Daniel J Friedman, John F Geisz, and Myles A Steiner. Effect of luminescent coupling on the optimal design of multijunction solar cells. *IEEE Journal of Photovoltaics*, 4(3):986–990, 2014.

[41] Carsten Baur, Martin Hermle, Frank Dimroth, and Andreas W Bett. Effects of optical coupling in III-V multilayer systems. *Applied Physics Letters*, 90(19):192109, 2007.

[42] V D Rumyantsev, N I Kozhuchov, D A Malevskiy, P V Pokrovskiy, Andreas W Bett, Robert D McConnell, Gabriel Sala, and Frank Dimroth. Transfer Of Power

By Photons In HCPV Triple-Junction Cells. In *6th International Conference on Concentrating Photovoltaic Systems: CPV-6*, pages 20–23. AIP, 2010.

[43] Myles A Steiner and John F Geisz. Non-linear luminescent coupling in series-connected multijunction solar cells. *Applied Physics Letters*, 100(25):251106, 2012.

[44] Antonio Marti and Gerardo L Araújo. Limiting efficiencies for photovoltaic energy conversion in multigap systems. *Solar Energy Materials and Solar Cells*, 43(2):203–222, 1996.

[45] A S Brown and M A Green. Radiative coupling as a means to reduce spectral mismatch in monolithic tandem solar cell stacks theoretical considerations. *Conference Record of the Twenty-Ninth IEEE Photovoltaic Specialists Conference, 2002*, pages 868–871, May 2002.

[46] J F Geisz, D J Friedman, J M Olson, S R Kurtz, and B M Keyes. Photocurrent of 1 eV GaInNAs lattice-matched to GaAs. *Journal of Crystal Growth*, 195(1):401–408, January 1998.

[47] David B Jackrel, Seth R Bank, Homan B Yuen, Mark A Wistey, James S Harris, Aaron J Ptak, Steven W Johnston, Daniel J Friedman, and Sarah R Kurtz. Dilute nitride GaInNAs and GaInNAsSb solar cells by molecular beam epitaxy. *Journal of Applied Physics*, 101(11):114916, 2007.

[48] Steven R Kurtz, J F Klem, A A Allerman, R M Sieg, C H Seager, and E D Jones. Minority carrier diffusion and defects in InGaAsN grown by molecular beam epitaxy. *Applied Physics Letters*, 80(8):1379, 2002.

[49] AJ Ptak, Sarah Kurtz, SW Johnston, DJ Friedman, JF Geisz, JM Olson, WE McMahon, AE Kibbler, C Kramer, M Young, et al. Defects in gainnas: what weve learned so far. In *National Centre for Photovoltaics and Solar Program Review Meeting: March 24–26 2003; Denver*, 2003.

[50] A J Ptak, D J Friedman, Sarah Kurtz, and R C Reedy. Low-acceptor-concentration GaInNAs grown by molecular-beam epitaxy for high-current p-i-n solar cell applications. *Journal of Applied Physics*, 98(9):094501, 2005.

[51] G Ungaro, G Le Roux, R Teissier, and J C Harmand. GaAsSbN: a new low-bandgap material for GaAs substrates. *Electronics Letters*, 35(15):1246–1248, 1999.

[52] J C Harmand, G Ungaro, L Largeau, and G Le Roux. Comparison of nitrogen incorporation in molecular-beam epitaxy of GaAsN, GaInAsN, and GaAsSbN. *Applied Physics Letters*, 77(16):2482, 2000.

[53] Siew Li Tan, Shiyong Zhang, Wai Mun Soong, Yu Ling Goh, Lionel JJ Tan, Jo Shien Ng, John PR David, Igor P Marko, Alfred R Adams, Stephen J Sweeney, et al. Gainnassb/gaas photodiodes for long-wavelength applications. *IEEE Electron Device Letters*, 32(7):919–921, 2011.

[54] K H Tan, S Wicaksono, W K Loke, D Li, S F Yoon, E A Fitzgerald, S A Ringel, and J S Harris, Jr. Molecular beam epitaxy grown GaNAsSb 1eV photovoltaic cell. *Journal of Crystal Growth*, 335(1):66–69, November 2011.

[55] K H Tan, W K Loke, S Wicaksono, D Li, Y R Leong, S F Yoon, P Sharma, T Milakovich, M T Bulsara, and E A Fitzgerald. Study of a 1eV GaNAsSb photovoltaic cell grown on a silicon substrate. *Applied Physics Letters*, 104(10):103906, March 2014.

[56] Michael Wiemer, Vijit Sabnis, and Homan Yuen. ¡title¿43.5In Kaitlyn VanSant and Raed A Sherif, editors, *SPIE Solar Energy + Technology*, pages 810804–810804–5. SPIE, August 2011.

[57] J Wu, W Shan, and W Walukiewicz. Band anticrossing in highly mismatched III–V semiconductor alloys. *Semiconductor Science and Technology*, 17(8):860, 2002.

[58] K Alberi, J Wu, W Walukiewicz, K Yu, O Dubon, S Watkins, C Wang, X Liu, Y J Cho, and J Furdyna. Valence-band anticrossing in mismatched III-V semiconductor alloys. *Physical Review B*, 75(4):045203, January 2007.

[59] A Lindsay, S Tomić, and E P O'Reilly. Derivation of a 10-band k p model for dilute nitride semiconductors. *Solid-State Electronics*, 47(3):443–446, March 2003.

[60] S. Kivelson and C. D. Gelatt. Photoluminescence in a disordered insulator: The trapped-exciton model. *Phys. Rev. B*, 26:4646–4673, Oct 1982.

[61] Teiji Yamamoto, Makoto Kasu, Susumu Noda, and Akio Sasaki. Photoluminescent properties and optical absorption of alas/gaas disordered superlattices. *Journal of applied physics*, 68(10):5318–5323, 1990.

[62] Y Tsai, B Barman, T Scrace, G Lindberg, M Fukuda, V R Whiteside, J C Keay, M B Johnson, I R Sellers, M Al Khalfioui, M Leroux, B A Weinstein, and A Petrou. Probing the nature of carrier localization in GaInNAs epilayers by optical methods. *Applied Physics Letters*, 103(1):012104, 2013.

[63] Soon Fatt Yoon, Kian Hua Tan, Wan Khai Loke, Satrio Wicaksono, and Tien Khee Ng. Method for fabricating ganassb semiconductor, June 19 2012. US Patent 8,202,788.

[64] John M Essick and Richard T Mather. Characterization of a bulk semiconductor's band gap via a near-absorption edge optical transmission experiment. *American Journal of Physics*, 61(7):646–649, July 1993.

[65] D E Aspnes. Third-derivative modulation spectroscopy with low-field electroreflectance. *Surface Science*, 37:418–442, June 1973.

[66] N L A Chan, N J Ekins-Daukes, J G J Adams, M P Lumb, M Gonzalez, P P Jenkins, I Vurgaftman, J R Meyer, and R J Walters. Optimal Bandgap Combinations - Does Material Quality Matter? *IEEE Journal of Photovoltaics*, 2(2):202–208, 2012.

[67] Kensuke Nishioka, Tatsuya Takamoto, Takaaki Agui, Minoru Kaneiwa, Yukiharu Uraoka, and Takashi Fuyuki. Evaluation of InGaP/InGaAs/Ge triple-junction solar cell and optimization of solar cell's structure focusing on series resistance for high-efficiency concentrator photovoltaic systems. *Solar Energy Materials and Solar Cells*, 90(9):1308–1321, May 2006.

[68] A Yoshida, T Agui, N Katsuya, K Murasawa, H Juso, K Sasaki, and T Takamoto. Development of ingap/gaas/ingaas inverted triple junction solar cells for concentrator application. In *21st International Photovoltaic Science and Engineering Conference (PVSEC-21)*, 2011.

[69] Jenny Nelson, Jenny Barnes, Nicholas Ekins-Daukes, Benjamin Kluftinger, Ernest Tsui, Keith Barnham, C Tom Foxon, Tin Cheng, and John S Roberts. Observation of suppressed radiative recombination in single quantum well p-i-n photodiodes. *Journal of Applied Physics*, 82(12):6240, 1997.

[70] Christian A Gueymard. Parameterized transmittance model for direct beam and circumsolar spectral irradiance. *Solar Energy*, 71(5):325–346, 2001.

[71] Brent N Holben, TF Eck, I Slutsker, D Tanre, JP Buis, A Setzer, E Vermote, John A Reagan, YJ Kaufman, T Nakajima, et al. Aeronet-a federated instrument network and data archive for aerosol characterization. *Remote sensing of environment*, 66(1):1–16, 1998.

[72] S Fahy and E P O'Reilly. Intrinsic limits on electron mobility in dilute nitride semiconductors. *Applied Physics Letters*, 83(18):3731, 2003.

[73] Sarah Kurtz, JF Geisz, DJ Friedman, JM Olson, A Duda, NH Karam, RR King, JH Ermer, and DE Joslin. Modeling of electron diffusion length in gainasn solar cells. In *Photovoltaic Specialists Conference, 2000. Conference Record of the Twenty-Eighth IEEE*, pages 1210–1213. IEEE, 2000.

[74] J F Geisz and D J Friedman. III–N–V semiconductors for solar photovoltaic applications. *Semiconductor Science and Technology*, 17(8):1–10, 2002.

[75] Steven R Kurtz, A A Allerman, E D Jones, J M Gee, J J Banas, and B E Hammons. InGaAsN solar cells with 1.0 eV band gap, lattice matched to GaAs. *Applied Physics Letters*, 74(5):729, 1999.

[76] W Shan, W Walukiewicz, J W III Ager, E E Haller, J F Geisz, D J Friedman, J M Olson, and S R Kurtz. Band Anticrossing in GaInNAs Alloys. *Physical Review Letters*, 82(6):1221–1224, February 1999.

[77] E P O Reilly, A Lindsay, and S Fahy. Theory of the electronic structure of dilute nitride alloys: beyond the band-anti-crossing model. *Journal of Physics: Condensed Matter*, 16(31):S3257–S3276, July 2004.

[78] Kuang-I Lin, Kuo-Lung Lin, Bo-Wei Wang, Hao-Hsiung Lin, and Jenn-Shyong Hwang. Double-Band Anticrossing in GaAsSbN Induced by Nitrogen and Antimony Incorporation. *Applied Physics Express*, 6(12):121202, December 2013.

[79] N Ben Sedrine, C Bouhafs, J C Harmand, R Chtourou, and V Darakchieva. Effect of nitrogen on the $GaAs_{0.9-x}N_xSb_{0.1}$ dielectric function from the near-infrared to the ultraviolet. *Applied Physics Letters*, 97(20):201903, 2010.

[80] G Leibiger, V Gottschalch, B Rheinländer, J Šik, and M Schubert. Model dielectric function spectra of GaAsN for far-infrared and near-infrared to ultraviolet wavelengths. *Journal of Applied Physics*, 89(9):4927, 2001.

[81] R.K. Ahrenkiel. Measurement of minority-carrier lifetime by time-resolved photoluminescence. *Solid-State Electronics*, 35(3):239 – 250, 1992.

[82] Alexander Gubanov, Ville Polojärvi, Arto Aho, Antti Tukiainen, Nikolai V Tkachenko, and Mircea Guina. Dynamics of time-resolved photoluminescence in GaInNAs and GaNAsSb solar cells. *Nanoscale Research Letters*, 9(1):80–80, January 2014.

[83] DZ Garbuzov. Reradiation effects, lifetimes and probabilities of band-to-band transitions in direct a3b5 compounds of gaas type. *Journal of Luminescence*, 27(1):109–112, 1982.

[84] D J Friedman, J F Geisz, W K Metzger, and S W Johnston. Trap-dominated minority-carrier recombination in GaInNAs pn junctions. *Applied Physics Letters*, 83(4):698, July 2003.

[85] R R King, D Bhusari, A Boca, D Larrabee, X Q Liu, W Hong, C M Fetzer, D C Law, and N H Karam. Band gapvoltage offset and energy production in nextgeneration multijunction solar cells. *Progress in Photovoltaics: Research and Applications*, 19(7):797–812, 2011.

[86] T S Wang, J T Tsai, K I Lin, J S Hwang, H H Lin, and L C Chou. Characterization of band gap in GaAsSb/GaAs heterojunction and band alignment in GaAsSb/GaAs multiple quantum wells. *Materials Science and Engineering: B*, 147(2-3):131–135, February 2008.

Appendix A

Sample layer structures

Layer structures are provided for each sample from top to bottom. Samples are sorted by growth code in ascending order.

Table A.1: Layer structure of N2264. Device. No antireflection coating.

Layer name	Nominal material	Thickness (nm)	Doping (cm^{-3})
Contact layer (etched under grid)	GaAs	300	p-type 1×10^{19}
Cap	$Al_{0.7}Ga_{0.3}As$	50	p-type 1×10^{19}
Emitter	GaAsSbN	200	p-type 2×10^{17}
Base	GaAsSbN	900	n-type 5×10^{16}
Buffer	GaAs		n-type 5×10^{18}
Substrate	GaAs		

Table A.2: Layer structure of N2265. Device. No antireflection coating.

Layer name	Nominal material	Thickness (nm)	Doping (cm^{-3})
Contact layer (etched under grid)	GaAs	300	n-type 5×10^{18}
Cap	$Al_{0.7}Ga_{0.3}As$	50	n-type 5×10^{18}
Emitter	GaAsSbN	200	n-type 2×10^{17}
Base	GaAsSbN	900	p-type 5×10^{16}
Buffer	GaAs		p-type 1×10^{19}
Substrate	GaAs		

Table A.3: Layer structure of N2436. Epilayer on polished substrate. No antireflection coating.

Layer name	Nominal material	Thickness (nm)	Doping (cm^{-3})
Epilayer	GaAsSbN	400	Unintentional
Substrate	GaAs		

Table A.4: Layer structure of N2623. Device with antireflection coating.

Layer name	Nominal material	Thickness (nm)	Doping (cm^{-3})
Contact layer (etched under grid)	GaAs	300	n-type 5×10^{18}
Cap	$Al_{0.7}Ga_{0.3}As$	50	n-type 5×10^{18}
Emitter	GaAs	200	n-type 1×10^{17}
Base	GaAsSbN	1000	Unintentional
Buffer	GaAs		p-type 1×10^{19}
Substrate	GaAs		

Table A.5: Layer structure of N2627. Device with antireflection coating.

Layer name	Nominal material	Thickness (nm)	Doping (cm^{-3})
Contact layer (etched under grid)	GaAs	300	n-type 5×10^{18}
Cap	$Al_{0.7}Ga_{0.3}As$	50	n-type 5×10^{18}
Emitter	GaAsSbN	200	n-type 1×10^{18}
Base	GaAsSbN	1000	p-type 1×10^{17}
Buffer	GaAs		p-type 1×10^{19}
Substrate	GaAs		

Table A.6: Layer structure of N2760. Double heterostructure, no antireflection coating.

Layer name	Nominal material	Thickness (nm)	Doping (cm^{-3})
Cap	GaAs	100	Unintentional
Cap	$Al_{0.7}Ga_{0.3}As$	50	Unintentional
Barrier	GaAs	50	Unintentional
Active layer	GaAsSbN	200	Unintentional
Barrier	GaAs	50	Unintentional
Substrate	GaAs		

Table A.7: Layer structure of N2761. Double heterostructure, no antireflection coating.

Layer name	Nominal material	Thickness (nm)	Doping (cm^{-3})
Cap	GaAs	100	Unintentional
Cap	$Al_{0.7}Ga_{0.3}As$	50	Unintentional
Barrier	GaAs	50	Unintentional
Active layer	GaAsSbN	200	p-type 1×10^{17}
Barrier	GaAs	50	Unintentional
Substrate	GaAs		

Table A.8: Layer structure of N2762. Double heterostructure, no antireflection coating.

Layer name	Nominal material	Thickness (nm)	Doping (cm^{-3})
Cap	GaAs	100	Unintentional
Cap	$Al_{0.7}Ga_{0.3}As$	50	Unintentional
Barrier	GaAs	50	Unintentional
Active layer	GaAsSbN	200	p-type 1×10^{18}
Barrier	GaAs	50	Unintentional
Substrate	GaAs		

Table A.9: Layer structure of N2763. Double heterostructure, no antireflection coating.

Layer name	Nominal material	Thickness (nm)	Doping (cm^{-3})
Cap	GaAs	100	Unintentional
Cap	$Al_{0.7}Ga_{0.3}As$	50	Unintentional
Barrier	GaAs	50	Unintentional
Active layer	GaAsSbN	200	n-type 1×10^{17}
Barrier	GaAs	50	Unintentional
Substrate	GaAs		

Table A.10: Layer structure of N2764. Double heterostructure, no antireflection coating.

Layer name	Nominal material	Thickness (nm)	Doping (cm^{-3})
Cap	GaAs	100	Unintentional
Cap	$Al_{0.7}Ga_{0.3}As$	50	Unintentional
Barrier	GaAs	50	Unintentional
Active layer	GaAsSbN	200	n-type 1×10^{18}
Barrier	GaAs	50	Unintentional
Substrate	GaAs		

Table A.11: Layer structure of N2765. Double heterostructure, no antireflection coating.

Layer name	Nominal material	Thickness (nm)	Doping (cm^{-3})
Cap	GaAs	100	Unintentional
Cap	$Al_{0.7}Ga_{0.3}As$	50	Unintentional
Barrier	GaAs	50	Unintentional
Active layer	GaAsSbN	100	p-type 1×10^{17}
Barrier	GaAs	50	Unintentional
Substrate	GaAs		

Table A.12: Layer structure of N2766. Double heterostructure, no antireflection coating.

Layer name	Nominal material	Thickness (nm)	Doping (cm^{-3})
Cap	GaAs	100	Unintentional
Cap	$Al_{0.7}Ga_{0.3}As$	50	Unintentional
Barrier	GaAs	50	Unintentional
Active layer	GaAsSbN	500	p-type 1×10^{17}
Barrier	GaAs	50	Unintentional
Substrate	GaAs		

Table A.13: Layer structure of N2767. Double heterostructure, no antireflection coating.

Layer name	Nominal material	Thickness (nm)	Doping (cm^{-3})
Cap	GaAs	100	Unintentional
Barrier	$Al_{0.7}Ga_{0.3}As$	50	Unintentional
Active layer	GaAsSbN	100	p-type 1×10^{17}
Barrier	$Al_{0.7}Ga_{0.3}As$	50	Unintentional
Substrate	GaAs		

Table A.14: Layer structure of N2772. Device. No antireflection coating.

Layer name	Nominal material	Thickness (nm)	Doping (cm^{-3})
Contact layer (etched under grid)	GaAs	300	n-type 5×10^{18}
Cap	$Al_{0.7}Ga_{0.3}As$	50	n-type 5×10^{18}
Emitter	GaAs	200	n-type 1×10^{17}
Base	GaAsSbN	1000	Unintentional
Buffer	GaAs		p-type 1×10^{19}
Substrate	GaAs		

Table A.15: Layer structure of N2773. Device. No antireflection coating.

Layer name	Nominal material	Thickness (nm)	Doping (cm^{-3})
Contact layer (etched under grid)	GaAs	300	n-type 5×10^{18}
Cap	$Al_{0.7}Ga_{0.3}As$	50	n-type 5×10^{18}
Emitter	GaAs	200	n-type 1×10^{17}
Base	GaAsSbN	1000	p-type 1×10^{16}
Buffer	GaAs		p-type 1×10^{19}
Substrate	GaAs		

Table A.16: Layer structure of N2774. Device. No antireflection coating.

Layer name	Nominal material	Thickness (nm)	Doping (cm^{-3})
Contact layer (etched under grid)	GaAs	300	n-type 5×10^{18}
Cap	$Al_{0.7}Ga_{0.3}As$	50	n-type 5×10^{18}
Emitter	GaAs	200	n-type 1×10^{17}
Base	GaAsSbN	1000	p-type 1×10^{17}
Buffer	GaAs		p-type 1×10^{19}
Substrate	GaAs		

Table A.17: Layer structure of N2776. Device. No antireflection coating.

Layer name	Nominal material	Thickness (nm)	Doping (cm^{-3})
Contact layer (etched under grid)	GaAs	300	n-type 5×10^{18}
Cap	$Al_{0.7}Ga_{0.3}As$	50	n-type 5×10^{18}
Emitter	GaAs	50	n-type 1×10^{18}
Emitter	GaAs	150	n-type 1×10^{17}
Base	GaAsSbN	1000	Unintentional
Buffer	GaAs		p-type 1×10^{19}
Substrate	GaAs		

Table A.18: Layer structure of N2777. Device. No antireflection coating.

Layer name	Nominal material	Thickness (nm)	Doping (cm^{-3})
Contact layer (etched under grid)	GaAs	300	n-type 5×10^{18}
Cap	$Al_{0.7}Ga_{0.3}As$	50	n-type 5×10^{18}
Emitter	GaAs	100	n-type 1×10^{17}
Emitter	GaAsSbN	100	n-type 1×10^{17}
Base	GaAsSbN	1000	Unintentional
Buffer	GaAs		p-type 1×10^{19}
Substrate	GaAs		

Appendix B

Streak camera images

Measurements obtained at University of Kobe. Method described in Section 3.4.2.

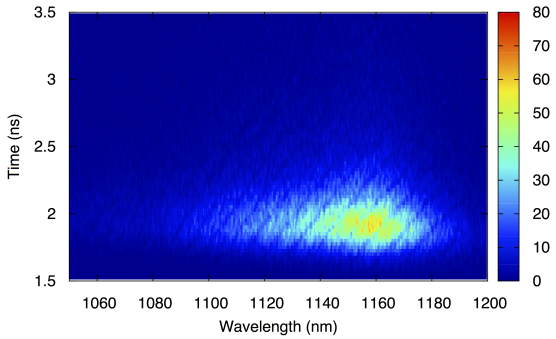


Figure B.1: Streak camera image of sample N2670 at room temperature (300 K), 900 nm incident excitation, 100μW incident power.

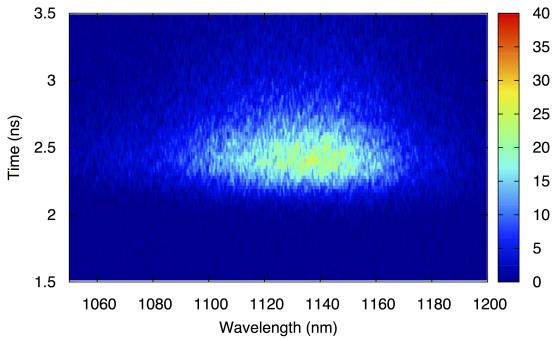


Figure B.2: Streak camera image of sample N2671 at room temperature (300 K), 900 nm incident excitation, 100μW incident power.

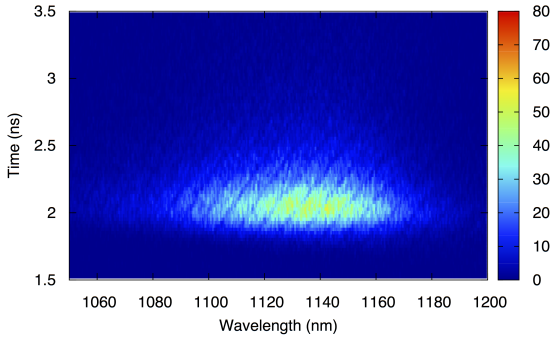


Figure B.3: Streak camera image of sample N2671 at room temperature (300 K), 900 nm incident excitation, 100μW incident power.

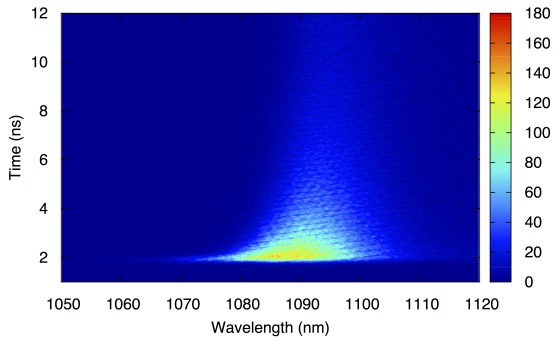


Figure B.4: Streak camera image of sample N2671 at 3 K, 900 nm incident excitation, 100μW incident power.

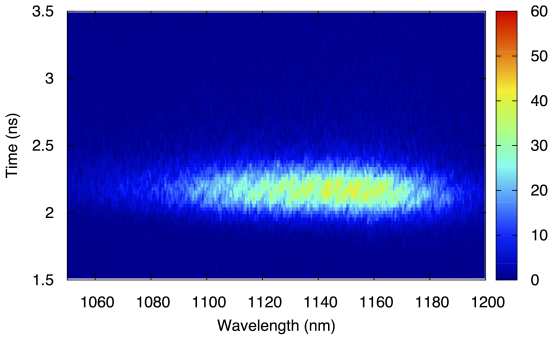


Figure B.5: Streak camera image of sample N2672 at room temperature (300 K), 900 nm incident excitation, 100μW incident power.

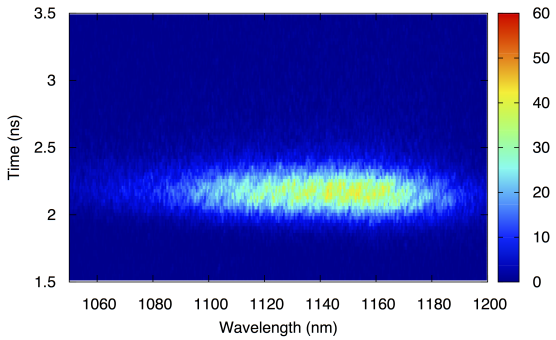


Figure B.6: Streak camera image of sample N2672 at room temperature (300 K), 900 nm incident excitation, 900μW incident power.

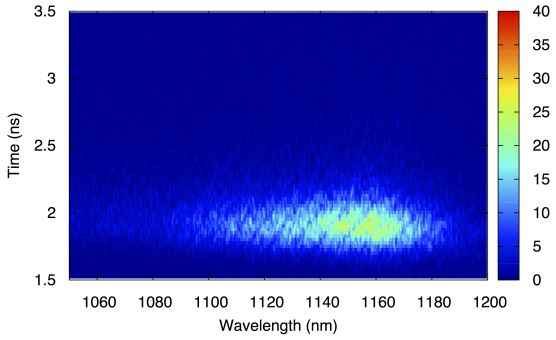


Figure B.7: Streak camera image of sample N2673 at room temperature (300 K), 900 nm incident excitation, 900μW incident power.

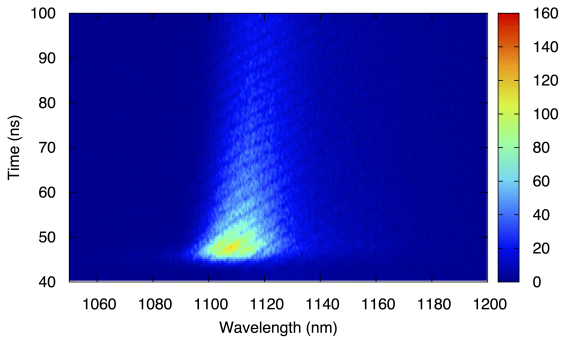


Figure B.8: Streak camera image of sample N2673 at 3 K, 900 nm incident excitation, 100μW incident power.

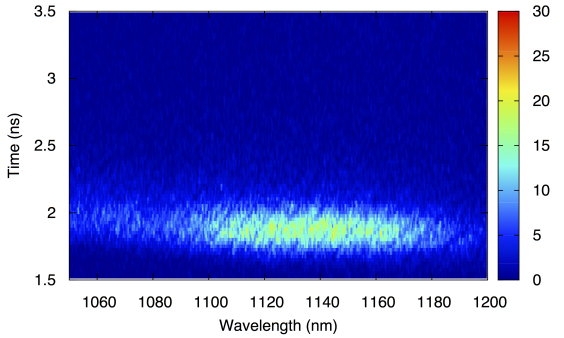


Figure B.9: Streak camera image of sample N2674 at room temperature (300 K), 900 nm incident excitation, 900μW incident power.

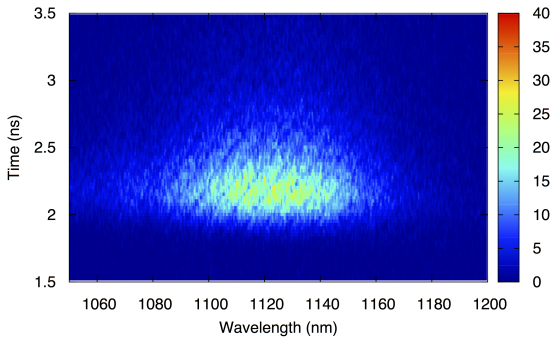


Figure B.10: Streak camera image of sample N2675 at room temperature (300 K), 900 nm incident excitation, 100μW incident power.

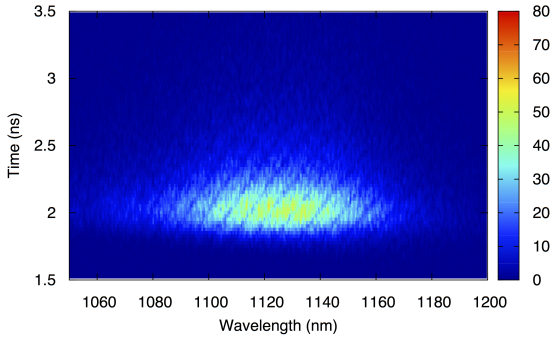


Figure B.11: Streak camera image of sample N2675 at room temperature (300 K), 900 nm incident excitation, 900μW incident power.

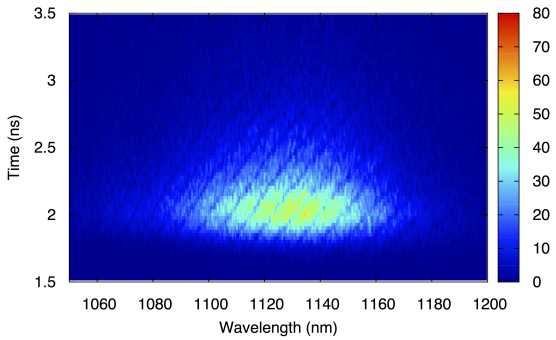


Figure B.12: Streak camera image of sample N2676 at room temperature (300 K), 900 nm incident excitation, 100μW incident power.

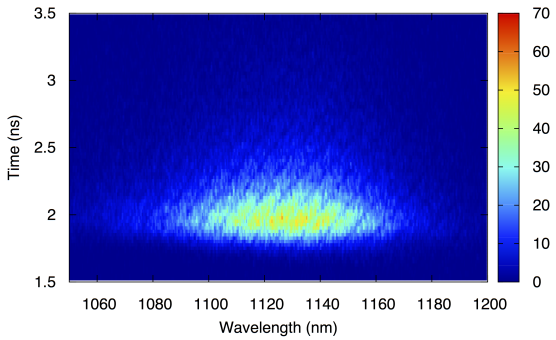


Figure B.13: Streak camera image of sample N2676 at room temperature (300 K), 900 nm incident excitation, 900μW incident power.

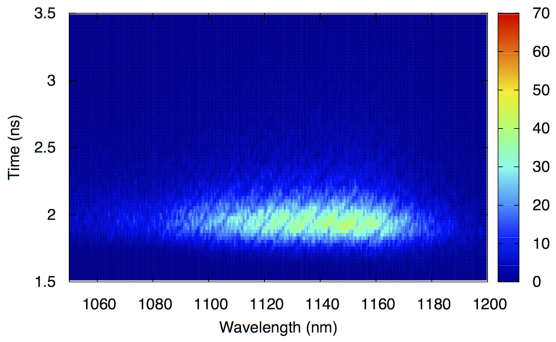


Figure B.14: Streak camera image of sample N2677 at room temperature (300 K), 900 nm incident excitation, 900μW incident power.

Appendix C

List of publications

Publications and conference proceedings authored or co-authored during this PhD project.

- Tomos Thomas, Ngai Lam Alvin Chan, Markus Führer, and NJ Ekins-Daukes. *Performance enhancement from radiative coupling considering realistic spectral conditions for optimal and sub-optimal bandgap multijunction solar cells.* In 2014 IEEE 40th Photovoltaic Specialist Conference (PVSC), pages 3409-3413. IEEE, 2014.

- Tomos Thomas, Markus Führer, Diego Alonso Alvarez, Ned Ekins-Daukes, Kian Hua Tan, Satrio Wicaksono, Wan Khai Loke, Soon Fatt Yoon, and Andrew Johnson. *GaNAsSb 1-ev solar cells for use in lattice-matched multi-junction architectures.* In 2014 IEEE 40th Photovoltaic Specialist Conference (PVSC), pages 0550-0553. IEEE, 2014.

- Tomos Thomas, Naofumi Kasamatsu, Kian Hua Tan, Satrio Wicaksono, Wan Khai Loke, Soon Fatt Yoon, Andrew Johnson, Takashi Kita, and Nicholas Ekins-Daukes. *Time-resolved photoluminescence of MBE-grown 1 ev GaAsSbN for multi-junction solar cells.* In Photovoltaic Specialist Conference (PVSC), 2015 IEEE 42nd, pages 1-5. IEEE, 2015.

- T Thomas, A Mellor, NP Hylton, D Alonso Alvarez, A Braun, NJ Ekins-Daukes, JPR David, SJ Sweeney, et al. *Requirements for a GaAsBi 1 ev sub-cell in a GaAs-based multi- junction solar cell.* Semiconductor Science and Technology, 30(9):094010, 2015.

- Ngai Lam Alvin Chan, Tomos Thomas, Markus Führer, and Nicholas J Ekins-Daukes. *Practical limits of multijunction solar cell performance enhancement from radiative coupling considering realistic spectral conditions.* IEEE Journal of Photovoltaics, 4(5):1306-1313, 2014.

- D Alonso-Álvarez, T Thomas, M Führer, NP Hylton, NJ Ekins-Daukes, D Lackner, SP Philipps, AW Bett, H Sodabanlu, H Fujii, et al. *InGaAs/GaAsP strain balanced multi-quantum wires grown on misoriented GaAs substrates for high efficiency solar cells.* Applied Physics Letters, 105(8):083124, 2014.

- Diego Alonso-Álvarez, Markus Führer, Tomos Thomas, and Ned Ekins-Daukes. *Elements of modelling and design of multi-quantum well solar cells.* In 2014 IEEE 40th Photovoltaic Specialist Conference (PVSC), pages 2865-2870. IEEE, 2014.

- Kasidit Toprasertpong, Hiromasa Fujii, Tomos Thomas, Markus Führer, Diego Alonso-Álvarez, Daniel J Farrell, Kentaroh Watanabe, Yoshitaka Okada, Nicholas J Ekins-Daukes, Masakazu Sugiyama, et al. *Absorption threshold extended to 1.15 ev using InGaAs/GaAsP quantum wells for over-50%-efficient lattice-matched quad-junction solar cells.* Progress in Photovoltaics: Research and Applications, 2015.

- Nicholas Hylton, Tomos Thomas, Kan Hua Lee, Yahya Al-Saleh, Ignacio Tobias, Nicholas Ekins-Daukes, et al. *Nanostructured solar cells: Surface textures and quantum dots.* In Optical Nanostructures and Advanced Materials for Photovoltaics, Optical Society of America, 2015.

- T Wilson, T Thomas, M Führer, and NJ Ekins-Daukes. *Addressing reflectivity losses in multi-junction solar cells to achieve 50% power conversion efficiency.* Materials Research Innovations, 19(7):503-507, 2015.

- A Mellor, NP Hylton, F Shirley, T Thomas, K-H Lee, Y Al-Saleh, A Braun, Josine Loo, Dries Vercruysse, Pol Van Dorpe, et al. *Nanoparticle scattering for radiation-hard multi-junction space solar cells.* In Photovoltaic Specialist Conference (PVSC), 2015 IEEE 42nd, pages 1-5. IEEE, 2015.

- Radek Roucka, Andrew Clark, Tom Wilson, Tomos Thomas, Markus Führer, Nicholas Ekins-Daukes, Andrew Johnson, Rick Hoffman, and David Begarney. *Demonstrating dilute-tin alloy SiGeSn for use in multijunction photovoltaics: Single- and multijunction solar cells with a 1.0-ev SiGeSn junction.* IEEE Journal of Photovoltaics, 6(4):1025-1030, 2016.

- A Mellor, NP Hylton, O Höhn, C Wellens, H Hauser, T Thomas, Y Al-Saleh, N Tucher, E Oliva, B Blasi, et al. Nanoparticle scattering for multijunction solar cells. In SPIE Photonics Europe, pages 989809-989809. International Society for Optics and Photonics, 2016.

- Tom Wilson, Tomos Thomas, Markus Fuúhrer, Nicholas J Ekins-Daukes, Radek Roucka, Andrew Clark, Andrew Johnson, Rick Hoffman Jnr, and David Begarney. *Single and multi-junction solar cells utilizing a 1.0 ev SiGeSn junction.* In 12th International Conference On Concentrator Photovoltaic Systems (CPV-12), volume 1766, page 060006. AIP Publishing, 2016.